

TECHNISCHE UNIVERSITÄT MÜNCHEN

Lehrstuhl E23 für Technische Physik

Walther-Meißner-Institut für Tieftemperaturforschung
der Bayerischen Akademie der Wissenschaften

Coupling phenomena in Nanomechanical Hybrid Systems

Daniel Schwienbacher

Vollständiger Abdruck der von der Fakultät für Physik der Technischen
Universität München zur Erlangung des akademischen Grades eines

Doktors der Naturwissenschaften

genehmigten Dissertation.

Vorsitzender: Prof. Dr. Michael Knap

Prüfer der Dissertation: 1. Priv.-Doz. Dr. Hans-Gregor Hübl

2. Prof. Dr. Christian Back

Die Dissertation wurde am 18.01.2021 bei der Technischen Universität München
eingereicht und durch die Fakultät für Physik am 15.03.2021 angenommen.

ABSTRACT

Nanomechanical systems and especially nanomechanical resonators are indispensable for mechanical sensor applications. They are used to measure e.g. forces, accelerations, masses or material parameters. For the latter applications, the high mechanical quality factors inherent in many nanomechanical resonators is a central feature. This enables high-precision measurements of the resonance frequency, and thus also the changes in resonance frequency due to external parameters. If we combine these features with further experimental degrees of freedom, we gain added functionality on one side and control over the mechanical properties via external parameters on the other. These control mechanisms can however also be used to learn more about the used external parameter and thus enable sensing applications. In this thesis, the coupling mechanisms of nanomechanical resonators to different experimental degrees of freedom are investigated. We use different coupling schemes to form hybrid systems. To this end, we couple nanomechanical resonators to mechanical, magnetic and electric degrees of freedom. To do this, we first introduce the workhorse of the thesis, a doubly clamped, tensile stressed nanomechanical string. We theoretically explore the models used to describe this system and then focus onto the different hybrid systems stemming from the different coupling mechanisms. First, we show a nanomechanical string network, comprised from three coupled nanomechanical resonators. Here, we investigate the coupling characteristics of the network and the dynamical excitation transfer within it. We experimentally reach a regime which cannot be described analytically anymore and generate a mechanical dark state in the system. We then focus onto a magnetomechanical hybrid system. Here the coupling is facilitated by a CoFe alloy thin film on top of a nanomechanical string. The CoFe material system has gained attention in the field of spintronics recently, as it was identified as a metallic magnetic system with ultra-low magnetic damping properties. One of the main questions is, if the magnetoelastic properties are connected to the magnetization damping properties of the material, as in the case of the well known material system Permalloy (NiFe). One of the main challenges, lies in the fact that the exceptional magnetic damping properties of CoFe only emerge in thin films and within specific layer stacks. This formidable challenge for conventional magnetostriction sensing methods can be overcome by using a nanomechanical string resonator, and we were able to extract the magnetostrictive constant for two CoFe alloys. We then gain further insight into the magnetomotive and magnetostrictive behavior of nanomechanical strings

by focusing on the effects of electrical currents passing through a string. This is again of interest for the field of spintronics because by mechanically releasing the conductors, one of the main sources for damping, the contact to the substrate, can be reduced. For this, we use a tensile stressed nanomechanical string covered with a cobalt thin film. This cobalt thin film is electrically connected at the two clamping points of the string. This enables voltage measurements across the string and sourcing electrical currents through it. Here, we find surprising new dynamics in the interplay of a nanomechanical string within an external magnetic field depending on the presence of an electrical current through the string. In the last part, we consider a system, where a nanomechanical string resonator is coupled to a superconducting circuit qubit. We discuss the system parameters necessary to enable ground state cooling and realizing three partite entanglement as well as how they can be reached in experiment. In this respect, we use finite element simulations to model the device and compare the results to early experiments.

Within this thesis, we present a network of mechanical strings and investigate the dynamical excitation transfer within. Further, we observe a mechanical dark state in one of the modes of the network, which is of interest in storage applications. We show how nanomechanical strings can be used to extract the magnetostrictive properties of a material where special magnetic properties are only apparent in thin films and within specific layer stacks, and which is therefore challenging for conventional measurement methods. We investigate how the presence of electrical current flow affects the mechanical properties of the nanomechanical string resonator. We also discuss the integration of a nanomechanical string into a circuit qubit, considering the field of circuit quantum dynamics as a foundation for nanomechanical sensing and storage applications.

ZUSAMMENFASSUNG

Nanomechanische Systeme und speziell nanomechanische Resonatoren sind unverzichtbare Komponenten für hochsensitive Sensorikanwendungen im Bereich mechanischer Freiheitsgrade. Sie werden dabei sowohl zur Messung von Kräften und Beschleunigungen eingesetzt als auch für Anwendungen, bei denen z.B. Massen oder Wechselwirkungen mit Materialparametern untersucht werden. In diesem Zusammenhang sind Systeme mit hohen mechanischen Güten von Interesse, da sich mit ihnen der Einfluss von externen Parametern auf die Resonanzfrequenz extrem empfindlich nachweisen lässt. Koppelt man diese mechanischen Resonatoren mit weiteren physikalischen Freiheitsgraden erhält man einerseits zusätzliche Funktionalität, andererseits erlaubt dies auch die Kontrolle mechanischer Eigenschaften durch externe Kontrollparameter. Im Umkehrschluss lassen sich dadurch auch diese zugrundeliegenden Freiheitsgrade erforschen. Diese Arbeit beschäftigt sich mit unterschiedlichen Kopplungsmechanismen, welche sich nutzen lassen um nanomechanische Resonatoren mit anderen Freiheitsgraden zu verknüpfen. Im Speziellen wird die Wechselwirkung von nanomechanischen Resonatoren mit mechanischen, magnetischen und elektrischen Freiheitsgraden untersucht. Dazu ist es zunächst notwendig, das zentrale Element dieser Arbeit, eine beidseitig aufgehängte, verspannte nanomechanische Saite theoretisch zu beschreiben und die dafür genutzten Modelle einzuführen. Anschließend wenden wir uns Hybridsystemen zu, die aus den verschiedenen Kopplungsmechanismen hervorgehen. Hier diskutieren wir als erstes ein Netzwerk aus drei gekoppelten nanomechanischen Saiten und untersuchen die aus der Kopplung resultierenden Konsequenzen sowie Fragen zur dynamischen Anregungsübertragung. Wir erreichen dabei ein experimentelles Regime, das sich nicht mehr durch eine analytische Lösung beschreiben lässt und erzeugen einen mechanischen Dunkelzustand in einer Mode des Netzwerkes. Als zweites gekoppeltes System, steht ein magnetomechanisches Hybridsystem im Fokus. Die Wechselwirkung ist hier durch die Magnetostriktion einer auf der Saite befindlichen CoFe Legierung gegeben. Letzteres Materialsystem wird im Feld der Spinelektronik derzeit sehr aktiv diskutiert, da es als metallisches, magnetisches System mit ultra-niedriger Magnetisierungsdämpfung identifiziert wurde. Eine zentrale Fragestellung in diesem Bereich ist, ob die Magnetisierungseigenschaften mit der Magnetoelastizität verknüpft sind, wie es z.B. im bekannten Materialsystem Permalloy (NiFe) der Fall ist. Die Tatsache, dass die niedrige Magnetisierungsdämpfung nur in dünnen Filmen beobachtet wird stellt hierbei eine extreme Herausforderung

an die Messmethodik. Durch Nutzung einer nanomechanischen Saite kann diese Herausforderung bewältigt werden und die Magnetostruktionskonstante von CoFe Legierungen innerhalb einer Dünnschicht bestimmt werden. Um weitere Einsichten in das magnetostruktive und magnetomotive Verhalten von nanomechanischen Saiten zu erhalten untersuchen wir die Effekte des Ladungsträgertransports durch die Nanosaiten auf deren mechanisches Verhalten. Dies ist von Interesse, da für spinelektronische Anwendungen auch die mechanische Freistellung von Leitern in Betracht gezogen wird, da dies die Dämpfungsraten zum Substrat reduziert. Dazu verwenden wir eine mit einem Cobalt Dünnschicht bedeckte Saite, welche an den beiden Ankerpunkten elektrisch kontaktiert ist. Im Zusammenspiel mit der Integration der Saite in einen elektrischen Schaltkreis beobachten wir eine Modifikation der mechanischen Eigenschaften, insbesondere eine unerwartete nicht-lineare Antwort des Systems. Im letzten Teil der Arbeit diskutieren wir ein Hybridsystem, in welchem eine nanomechanische Saite Teil eines supraleitenden Schaltkreisquantenbits ist. Hierfür diskutieren wir die notwendigen Systemparameter um Grundzustandskühlung und das Vermitteln einer Verschränkung zwischen den Teilsystemen zu ermöglichen und verknüpfen dies mit einer realen Probenauslegung. Hierfür nutzen wir finite Element Simulationen die wir mit frühen Experimenten vergleichen.

Zusammenfassend beschäftigt sich diese Arbeit mit der Kopplung unterschiedlicher Freiheitsgrade an die mechanischen Eigenschaften einer Nanosaiten. In dieser Arbeit untersuchen wir, durch den Aufbau eines Netzwerks aus Saiten die dynamische Anregungsübertragung zwischen gekoppelten Saiten. Im selben System erzeugen wir einen mechanischen Dunkelzustand, der z.B. für Speicheranwendungen relevant sein kann. Wir legen dar wie nanomechanische Saiten genutzt werden können um die Magnetostruktion von einem Material zu bestimmen, dessen besonderen magnetischen Dämpfungseigenschaften nur in dünnen Filmen und innerhalb spezifischer Schichtabfolgen zu Tage tritt. Wir untersuchen den Einfluss elektrischer Ströme auf nanomechanische Saiten die z.B. als freistehende Leiter in Spinelektronikanwendungen von Bedeutung sein können. Zuletzt diskutieren wir die Integration einer nanomechanischen Saite in ein Schaltkreisquantenbit, dies ermöglicht den Einsatz von nanomechanischen Saiten für Sensorik und Speicheranwendungen im Bereich der supraleitenden Schaltkreisquantendynamik.

CONTENTS

Abstract	I
Zusammenfassung	III
Introduction	1
1 Introduction to the basics of nano-mechanical string resonators	5
1.1 Introduction	5
1.2 Euler-Bernoulli beam theory	6
1.2.1 Inhomogeneous nano-strings	11
1.3 Nanomechanical string resonators as linear harmonic oscillators	14
1.3.1 Thermal excitations	14
1.3.2 Nonlinear effects in nano-strings	16
1.3.3 In-situ frequency tuning mechanism	19
1.4 Coupling concepts in nanomechanical string resonator networks	20
1.5 Summary	22
2 Nanomechanical resonator networks	23
2.1 Introduction	23
2.2 Theoretical background	24
2.2.1 Landau Zener physics/ transition dynamics	24
2.2.1.1 The three-level Landau-Zener model	26
2.2.2 Multiple coupled mechanical resonators	28
2.2.2.1 N coupled resonators	31
2.3 Device design and fabrication	34
2.3.1 Device fabrication	34
2.3.2 Device design	35
2.4 Measurement setups	36
2.4.1 Optical interferometry	37
2.4.2 Frequency domain setup	37
2.4.3 Time domain setup	39
2.5 Measurement results	39

2.5.1	Characterization measurements	39
2.5.1.1	Emergence of mechanical dark modes	43
2.5.2	Excitation transfer dynamics	47
2.6	Discussion and Outlook	52
3	Magnetostrictive interaction in nanomechanical resonators	55
3.1	Introduction	55
3.2	Theoretical background	56
3.2.1	Magnetostriction in a free FM thin film	57
3.2.2	Magnetostriction in a thin film on a substrate	59
3.2.3	Magnetostriction in a multi layer string	61
3.3	Device design and fabrication	62
3.4	Measurement setup	63
3.4.1	Optical interferometer	63
3.5	Magnetostriction of ultra-low damping CoFe films	64
3.6	Discussion and Outlook	71
4	Impact of electrical currents onto magnetostrictive interactions in nanomechanical resonators	73
4.1	Introduction	73
4.2	Electrical readout strategies	74
4.2.1	Lorentz force considerations	74
4.2.2	Control of the characteristic mechanical parameters by a quasi static bias current	76
4.2.3	Anisotropic magneto-resistance	77
4.3	Sample fabrication	78
4.4	Measurement setup	79
4.4.1	Electrical readout	79
4.5	Magneto-electromotive interactions in an electrically connected nano-string	81
4.5.1	Simultaneous probing of the mechanical motion using optical and electrical readout	81
4.5.2	Temperature shifts due to current	87
4.6	Discussion and Outlook	89
5	Superconducting nano-mechanical circuit devices	91
5.1	Introduction	91
5.2	Embedding nano-electromechanics in superconducting quantum circuits . .	92
5.3	Modeling and simulations	94
5.3.1	The transmon layout	94
5.3.2	The X-mon layout	99
5.4	Discussion and Outlook	103
	Discussion and Outlook	105
A	Nanomechanical string resonators	107
A.1	In situ frequency tuning mechanism - technical considerations	107

B Nanomechanical resonator networks	109
B.1 Optical interferometer	109
B.2 In line network dynamics	110
C Magnetomechanical and magnetomotive hybrid systems	113
C.1 nano-stringfrequency buckling considerations using FEM simulations	113
C.2 Magnetization damping of CoFe stacks on SiN substrates measured using broadband magnetic resonance	113
C.3 Optical and electrical measurement setups	114
Bibliography	119
List of Publications	133
Acknowledgments	135

INTRODUCTION

Macroscopic mechanical resonators are ubiquitous. They are harnessed for mechanical clocks [1], tuning forces [2] or simple swings [3], but they can also make our life more challenging, when thinking about undesired resonances of buildings [4] or bridges [5]. Amongst the most desired applications are high precision time keepers, which have long tradition in science, as time is essential for the understanding of nearly every dynamic physical phenomenon, as well as indispensable for navigation application [6]. But also for scientific endeavors they are of high interest e.g. for the discovery of flux quantization [7], or the Einstein-de Haas effect [8, 9].

In the last century, miniaturizing mechanical resonators played a huge role in industry and science and led eventually to the advent of micromechanical resonators [10, 11]. These resonators are typically of sub-millimeter dimensions [12–15], which makes them a compact component for a large variety of applications [13, 16, 17]. Amongst these are force, mass and acceleration sensing. Micro-electro-mechanical systems (MEMS) started out in automotive and aerospace applications where they were and are used as simple acceleration and pressure sensors [18, 19], but are nowadays part of many devices used in cars and airplanes. This begins at passenger security features like airbag release sensors or tire pressure sensors and ends with passenger amenities such as automated climate control or smart windows [20–23]. In industrial environments they are frequently used for monitoring vibrations and motion [24, 25]. In the last two decades, they were introduced into consumer electronics and are used, among others, as sensors for pressure, acceleration, magnetic field and yaw rate in most smart devices like smart-phones, tablet computers and smart-watches [26–29]. There, they mainly function as low-cost sensors with low energy consumption [29].

In scientific research, the integration of micro and nanomechanical resonators facilitated an increase in the sensitivity of many analytic tools in e.g. material science or physics. Scanning tunneling microscopy (STM) [30], atomic force microscopy (AFM) [31] and similar techniques [32–34] are only possible due to micromechanical cantilevers [35]. These techniques enable the investigation of e.g. persistent currents in metal rings [36] or to measure the Casimir force [37, 38]. Similar resonators are now also utilized to act as detectors for quantum properties such as spins in color-centers [39, 40] or to read out superconducting circuits [41]. The success of many of these applications hinges on the force, displacement,

mass or acceleration sensitivity. By miniaturizing the mechanical resonator to nanoscale dimensions [42–45], the sensitivity limit of the sensor can be generally improved allowing for additional applications. In the meanwhile, nanomechanical resonators demonstrated force sensitivities in the attonewton [46, 47] and sub-attonewton range [48, 49], they can detect deflections in the range of picometers [50], and detect single masses with a sensitivity in the yoctogram range [51] corresponding to the mass of a single proton. They also were shown to enable the manipulation of spins [52] as well as the detection of a single atomic spin [39]. Another area of applications lies in the use of nanomechanical sensors in biology and chemistry [53–55], where the abilities to measure forces and masses are used to e.g. determine the forces in biological or chemical reactions [56–60] or detect the presence of specific elements or molecules in a compound [61–65].

Apart from these applications, where ultimate sensitivity is the goal, nanomechanical resonators, especially nanomechanical string resonators, widen the area of applications or can be used to reduce the power consumption of sensors. They can be employed for sensing applications in otherwise challenging areas or reduce the sensor footprint. To this end coupling several nanomechanical string resonators is an option to connect several sensors into an array [66–68] or to enable remote sensing applications [69]. This can be achieved by coupling them mechanically with each other [70–72], by coupling several modes of one mechanical resonator [73, 74], or by coupling several of them via an external entity like an optical field [75]. Moreover, as the characteristic properties of such resonators are linked to the material parameters of the host material, these resonators are also ideal candidates for investigations in the field of material science. Examples in this respect are the Young’s modulus of a material including the mechanical damping properties, as well as interactions of the lattice with other degrees of freedom like electric polarization (piezoelectricity) and magnetic properties (magnetoelasticity and striction) [34, 76–80]. In addition, conductive mechanical systems also allow to investigate the coupling of charge transport properties of the material which gives rise to a manifold of magnetomotive interactions in diverse environments [81–89].

The field of extreme mechanical sensing is intimately connected to the question, whether it is possible to prepare a mechanical system in a quantum mechanical state to research true „quantum mechanics“. For this purpose, the field of optomechanics couples mechanical systems to optical or quasi-optical resonators, so that their resonance frequency becomes dependent on the displacement of the mechanical object. The sub-field of nanoelectromechanics developed this concept further by combining superconducting microwave resonators with nanomechanical systems [90–92]. This opened the pathway for many key experiments such as reaching the quantum limit of a nanomechanical resonator [93], ground state cooling [94–96] squeezing [97], electromechanical interference [98, 99], optomechanics with squid devices [100, 101], strong coupling [101–103], information transfer [104, 105], and the combination of these circuits with elements of quantum electrodynamics [106, 107].

In this thesis, we focus on the different mechanisms that can be utilized to couple a nanomechanical string resonator to a system of interest for the purpose of using the mechanical resonator as sensor for the respective coupling properties. In this context, we investigate various realizations of coupled systems based on mechanical, magnetostrictive, magnetomotive and electromechanical coupling. In detail, the thesis is structured as follows: In Part 1, we introduce the workhorse of this thesis, a doubly clamped nano-string resonator, with large mechanical quality factor. Here, we present models for the mechanical

properties of strings made from homogeneous as well as multi-layered materials, consider geometric non-linearities, and present an in-situ frequency tuning mechanism. We further introduce the different coupling mechanisms later investigated in this thesis. Part 2, is dedicated to the steady state and dynamic response of a network of three coupled high- Q nanomechanical string resonators. This system is a classical analog to a three-level Landau-Zener system. We discuss the model necessary to describe such a system in the classical framework. In detail, we investigate the inter-string coupling mechanics and the emergence of mechanical dark states if all resonators are frequency degenerate and examine the dynamics of the full network focusing on the controlled transfer of excitations within the network. We compare the experimental results with numerical simulations using only predetermined system parameters. Part 3 of the thesis examines the magnetostrictive properties of an ultra-low magnetic damping $\text{Co}_{25}\text{Fe}_{75}$ compound [108]. To this end we show how a nano-string resonator can be used to extract a solid state property, the magnetostrictive constant from a magnetic thin film material which is grown in an elaborate layer stack as a part of a string. In this context, the nano-string form factor is of particular advantage, as the particular magnetic damping properties only reveal themselves when the magnetic layer is fabricated in form of a thin film system. Part 4 of the thesis, considers the magnetomotive interactions of a nanomechanical resonator topped with a magnetic cobalt layer. Here, we expand the field of magnetomotive excitation and readout in nanomechanical resonators by using a magnetic material for an electric readout. We find surprising dynamics in the system when sourcing electrical currents through a nano-string, both in the presence and absence of external magnetic fields. We investigate the impact of electrical currents onto the mechanical properties of a nano-string, and discuss the back-action of the magnetomotive readout technique onto a metalized magnetic nano-string. In Part 5, we touch upon the integration of a nanomechanical resonator into superconducting circuits and in particular the combination of a coplanar waveguide resonator at microwave frequencies, a transmon qubit and a nanomechanical string resonator. We present a concise overview of the relevant system parameters, how they interact with each other and how they can be engineered by changing the device layout. Using finite element simulations of the device layout we engineer the desired device parameters and compare those results to early experiments. We further discuss the implications of switching the transmon layout to the so called X-mon geometry, and why this benefits the endeavor of combining a transmon qubit with a nanomechanical string resonator. Finally we give a summary over this thesis and provide an outlook on possible and ongoing experimental work regarding the different topics we discussed in this thesis.

PART 1

INTRODUCTION TO THE BASICS OF NANO-MECHANICAL STRING RESONATORS

1.1 Introduction

In this thesis, we explore hybrid systems held together by a common constituent - a nano-mechanically compliant string resonator, in short nano-string. Thus, the core and main theme of this thesis is to investigate and understand readout mechanisms to gain access to the motion of the nano-string and the interplay of mechanical motion for the purpose of information conversion, storage applications and in particular sensing applications. These nano-strings will consist of different materials and will be tailored for the specific experiment. However, the description of the displacement of a nano-string can be formulated in a general manner, with the details taken into account in the form of material parameters. As the nano-strings are key to the experiments performed in this thesis, we start with a review of their general and unifying properties. The introduction presented here is based on *Foundations of nanomechanics* [109] by Andrew N. Cleland and *Fundamentals of nanomechanical resonators* [110] by Silvan Schmid, Luis G. Villanueva and Michael L. Roukes. For a more engineering emphasized view onto the subject, we suggest *Vibration problems in engineering* [111] by Stephen Timoshenko.

We will start with the definition of a nano-string, followed by the model used to describe the system. We will present the equations governing the mechanical vibrations of a nano-string using Euler-Bernoulli beam theory. We will consider how external driving forces of different strength impact these vibrational modes and lead to geometric nonlinearities. We show, how we can use these effects to characterize the nano-strings and, how to in-situ tune their vibrational resonance frequencies. In the last section of this part we will shortly discuss the different coupling mechanisms used to create hybrid devices to be discussed later in this work, followed by a short summary of this part.

1.2 Euler-Bernoulli beam theory

In this section we discuss the mechanical vibration of a double clamped, suspended prismatic bar¹. This construct is commonly known as a beam, however since all devices considered within this thesis will be pre-stressed, we will use the name for a pre-stressed prismatic bar: a string. We consider the dynamics of such a string in the framework of the Euler-Bernoulli beam theory and show that the picture of a mechanically oscillating beam or string can be reduced to the case of an harmonic oscillator with a pointlike center of mass motion. This will simplify many discussions presented within this thesis considerably. However, we note that we physically always deal with extended three dimensional string resonators.

Under the label nano-string, we understand a double clamped, suspended mechanical string resonator, as it can be schematically seen in Fig. 1.1, next to a SEM image showing an actual device. To describe such a string, we denote its length along the x -axis as l , the thickness along the z -axis as t and the width along the y -axis as w . Since the two parameters w and t have dimensions of ≈ 100 nm, we call them nano-strings. The dynamics of the out of plane vibration of a homogeneous, undamped nano-string can be described by standard or Euler-Bernoulli beam theory [109, 111]. For this, we need to discuss the forces acting onto the string. As already stated, we only use tensile stressed nano-beams or string resonators in this work. Therefore the dominant force acting on a nano-string is a restoring force $F_{\text{restoring}}$, pulling the object into an equilibrium position². The main part of this restoring force originates from the pre-stress ($F_{\text{prestress}}$), however due to the three dimensional nature of the string, also the bending force of the string F_{bending} needs to be considered ($dF_{\text{restoring}} = dF_{\text{bending}} + dF_{\text{prestress}}$). To get a better insight into these two

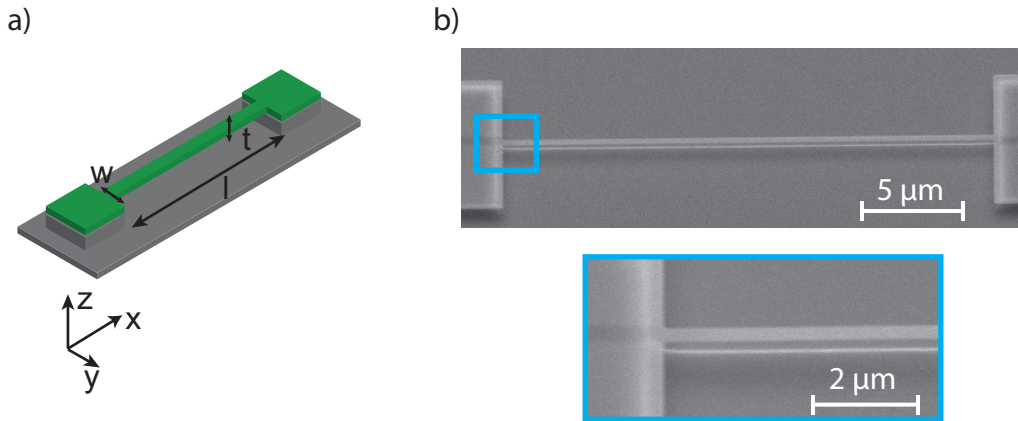


Figure 1.1: a) Schematic drawing of a nano-string defining the local coordinate system. b) Tilted SEM image of a 25 μm long, double clamped Si_3N_4 nano-string and zoom in on the left clamping area, clearly showing the release from the Si substrate.

forces we will discuss how they act on an infinitesimal volume element in a beam. This is shown in Fig. 1.2 a) & b). This volume element has a length dx and a crosssection $A = wt$ as well as a mass density ρ . The displacement from the equilibrium position $a(x)$ is defined

¹All devices considered in this work will have a rectangular crosssection.

²Gravitational forces are negligible and thus omitted.

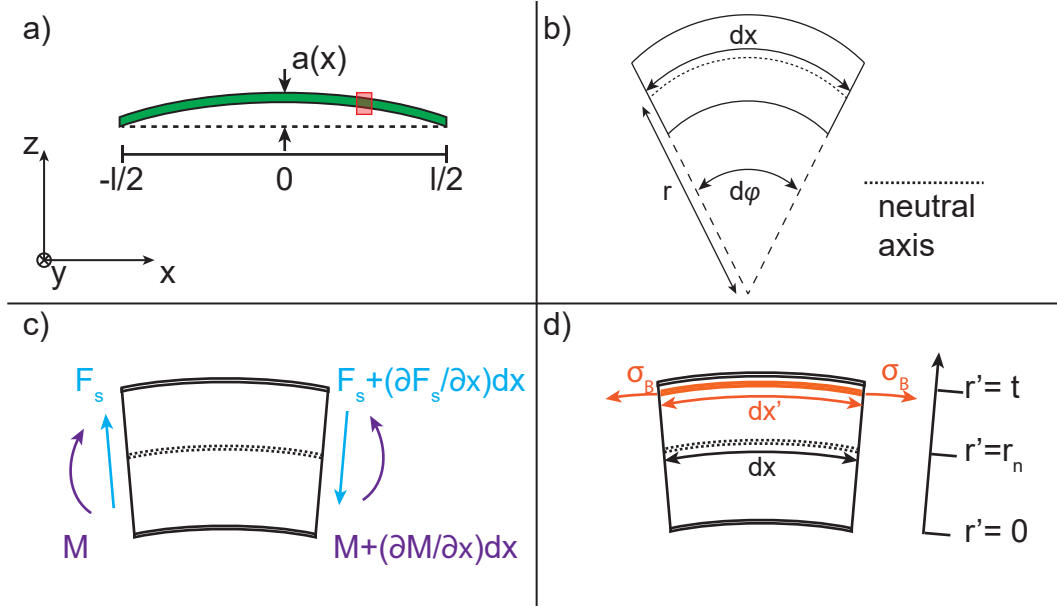


Figure 1.2: a) Schematic drawing of a slightly bent nano-beam. b) Zoom in on a infinitesimal volume element of the beam. c) Forces and torques acting on the volume element due to the bending. d) Added stress in the volume element due to the torque.

to happen only along the z -axis. If the beam is slightly displaced from the equilibrium position, a restoring force will occur. In the following we will use the standard beam theory to describe the bending of a beam [111]. This standard beam theory contains the concept of a neutral layer or axis in a beam or string. If the beam is bent or a part of it displaced, the neutral axis will retain the same length it had in the equilibrium position, whereas the areas to either side are either stretched or compressed accordingly. In a homogeneous beam³, which we consider at this point, this neutral layer is in the geometric center of the object [111]. If a part of the beam is now displaced e.g. bent, the aforementioned compressed and stretched layers of the beam want to return to the equilibrium position, thus a restoring force, countering the force that displaced, or bent the beam occurs. We now want to elaborate this in a more mathematic fashion. The restoring force acting on a volume element of the beam can be associated with a shear force $F_S(x)$ and a torque $M(x)$ (acting along the y -direction) as depicted in Fig. 1.2 c). Here the total force acting on the volume element due to bending in z -direction is given by $dF_{\text{bending}} = -\frac{\partial F_S}{\partial x} dx$. The total moment acting on the beam $\frac{\partial M}{\partial x} dx$ is related to the shear force F_S via [111, 112]:

$$\frac{\partial M}{\partial x} dx = F_S \frac{dx}{2} + \left(F_S + \frac{\partial F_S}{\partial x} dx \right) \frac{dx}{2} \approx F_S dx. \quad (1.1)$$

We now want to derive, how this bending moment M relates to the bending curvature of the beam $\frac{\partial^2 a}{\partial x^2}$ and how we can translate it into a stress in the beam. This will allow us to compare and integrate it with the pre-stress in a string later on. If the beam is bent, the

³This implies a homogeneous mass density distribution $\rho \neq f(x)$

neutral layer at $r' = r'_n$ by definition, does not change. However, the other layers of the string are either elongated or compressed respectively. This change in length is given by

$$dx' - dx = dx \frac{r' - r'_n}{r},$$

with r the bending radius of the string. This results in a bending stress σ_B in a given layer of the string (cf. Fig. 1.2 d) [113]:

$$\sigma_B = E \frac{dx' - dx}{dx} = E \frac{r' - r'_n}{r}, \quad (1.2)$$

with which we then can calculate the torque:

$$dM = \sigma_B w dr' (r' - r'_n) = E w dr' \frac{(r' - r'_n)^2}{r}.$$

We get the total bending moment by integrating over the beam thickness t under the assumptions of a homogeneous beam, in which case the neutral layer lies in the center $r'_n = t/2$:

$$M = \int_{r'=0}^t dM = E w t^3 / (12r). \quad (1.3)$$

With the moment of inertia for this bending in z -direction $I_z = wt^3/12$ and $1/r = \frac{\partial^2 a}{\partial x^2}$ [111] we arrive at:

$$M = EI \frac{\partial^2 a}{\partial x^2}, \quad (1.4)$$

and can write the bending force using $dF_{\text{bending}} = -\frac{\partial F_S}{\partial x} dx$ and Eq. (1.1) as

$$dF_{\text{bending}} = -EI \frac{\partial^4 a}{\partial x^4} dx. \quad (1.5)$$

We now want to consider a pre-stress in the material. This will lead us from considering a beam towards considering a string as this prestress changes the behavior of the object considerably. We first consider the prestress independently from any bending effects. Again, we consider an infinitesimal volume element of the string to define the forces. A prestress in the material leads to axial forces in the string. Since we only consider displacements of the string in z -direction, only the axial forces in x -direction are of interest here. Thus the prestress leads to two axial forces ($F_{\text{ax},1}$) and ($F_{\text{ax},2}$) in the volume element, pointing tangential to the neutral axis towards both sides as can be seen in Fig. 1.3. These forces are given by:

$$\begin{aligned} \vec{F}_{\text{ax},1} &= \sigma_0 A (-\cos(\varphi_1) \vec{x} + \sin(\varphi_1) \vec{z}), \\ \vec{F}_{\text{ax},2} &= \sigma_0 A (\cos(\varphi_2) \vec{x} - \sin(\varphi_2) \vec{z}). \end{aligned}$$

Here σ_0 denotes the prestress and $\varphi_{1/2}$ are the bending angles as indicated in Fig. 1.3. This results in a net force of:

$$d\vec{F}_{\text{prestress}} = \vec{F}_{\text{ax},2} + \vec{F}_{\text{ax},1} = \sigma_0 A [(\cos(\varphi_2) - \cos(\varphi_1)) \vec{x} + (\sin(\varphi_1) - \sin(\varphi_2)) \vec{z}]. \quad (1.6)$$

If we assume a small string displacement ($a \ll l$ and $\varphi_{1/2} \ll 1$), we can make the following approximations: $\cos(\varphi_2) - \cos(\varphi_1) \approx 0$ and $\sin(\varphi_1) - \sin(\varphi_2) \approx \varphi_1 - \varphi_2 \equiv d\varphi$. This change in angle can also be described with the curvature radius $d\varphi \approx dx/r$ with [114]

$$\frac{1}{r} = \frac{\frac{\partial^2 a}{\partial x^2}}{\left[1 + \left(\frac{\partial a}{\partial x}\right)^2\right]^{3/2}} \approx \frac{\partial^2 a}{\partial x^2}.$$

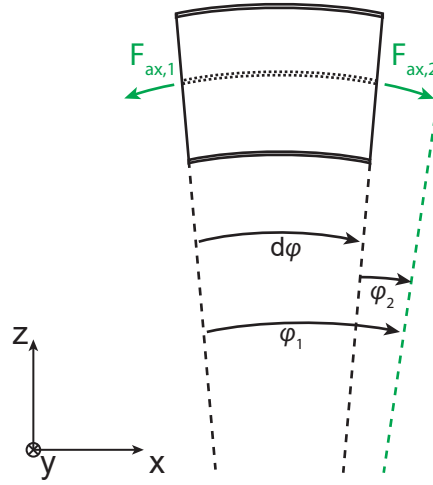


Figure 1.3: a) Schematic of a infinitesimal volume element of the string (cf. Fig. 1.2 b)). The prestress leads to axial forces along the interfaces that can be combined at the neutral axis of the string.

This results in the expression for the prestress induced force

$$d\vec{F}_{\text{prestress}} = \sigma_0 A dx \frac{\partial^2 a}{\partial x^2} \vec{z}. \quad (1.7)$$

We now combine these two forces into the restoring force of the nano-string $dF_{\text{restoring}} = dF_{\text{bending}} + dF_{\text{prestress}}$ and use the Euler-Bernoulli beam theory to obtain the equation of motion for the transverse vibrational mode of the nano-string [109, 111]:

$$-EI \frac{\partial^4 a}{\partial x^4} + \sigma_0 A \frac{\partial^2 a}{\partial x^2} = \rho A \frac{\partial^2 a}{\partial t^2}, \quad (1.8)$$

with EI being the flexural rigidity of the nano-string. If we assume a harmonic time dependence for the local displacement $a(x, t) = a(x) \exp(-i\Omega t)$ [111] the differential equation transforms to:

$$-EI a^{(4)}(x) + \sigma_0 A a^{(2)}(x) = -\rho A \Omega^2 a(x) \quad (1.9)$$

The general solution for Eq. (1.9) is given by [109, 111]

$$a(x) = c_1 \exp(\alpha x) + c_2 \exp(-\alpha x) + c_3 \sin(\beta x) + c_4 \cos(-\beta x) \quad (1.10)$$

with

$$\alpha = \sqrt{\mu_+} > 0, \text{ and} \quad (1.11)$$

$$\beta = -i\sqrt{\mu_-} > 0. \quad (1.12)$$

$$I = \frac{wt^3}{12}, \quad (1.13)$$

$$A = wt, \quad (1.14)$$

$$\mu_{\pm} = \frac{\sigma_0 A \pm \sqrt{\sigma_0^2 A^2 + EI \rho A \Omega^2}}{2EI}. \quad (1.15)$$

For a doubly clamped string the boundary conditions are given by [109, 111]

$$\begin{aligned} a(x = \pm l/2) &= 0 \\ \partial a(x = \pm l/2)/\partial x &= 0. \end{aligned} \quad (1.16)$$

The application of these boundary conditions to the general solution (1.10), results in a homogeneous system of four linear equations and four variables c_i ($i = 1, 2, 3, 4$). If the determinant of this system vanishes, this yields the non-trivial solutions for the displacement

$$e^{-\alpha l}[(\alpha^2 - \beta^2)(e^{2\alpha l} - 1) \sin(\beta l) + 4\alpha\beta e^{\alpha l} - 2\alpha\beta(e^{2\alpha l} + 1) \cos(\beta l)] = 0. \quad (1.17)$$

While the above result is general, its solutions require numerical methods. However, many suitable approximations for analytical forms can be found. The simplest resonance frequency for a nano-string used in the literature [109, 111, 115], is for the so-called *highly-tensile-stressed* (HTS) nano-string. Here, the assumption is, that a high enough pre-stress in the material ($\sigma_0 \gg EI\pi^2/Al^2$) dominates the motion of the string. In this case, the equation of motion (1.8) can be reduced to:

$$\ddot{a}(t) - \left(\frac{n\pi}{l}\right)^2 \frac{\sigma_0}{\rho} a(t) = 0 \quad (1.18)$$

and the corresponding resonance frequency of the nano-string is given by

$$\Omega_{n,\text{HTS}} = \frac{n\pi}{l} \sqrt{\frac{\sigma_0}{\rho}}, \quad (1.19)$$

with n being the mode number. However, as can clearly be seen, this approximation fully neglects the contribution of the restoring force due to the bending of the nano-string and assumes it to be fully floppy. While this approximation may be fine for a general description of the resonance of a nano-string, in this thesis, we want to use the precise measurement of the nano-string's resonance frequency to investigate material parameters. Therefore, we need an alternative approximation of the resonance frequency of a highly tensile stressed nano-string, which includes those bending effects, at least to first order. For this, we don't employ the approximation used for (1.19) [115, 116], but instead use the fact that for all tensile stressed strings in this thesis the effects due to bending can be seen as a small disturbance contributing to the prestress dominated motion. The mathematical relation expressing this, is given by $4EI\rho A\Omega^2 \ll \sigma_0^2 A^2$.⁴ This allows to approximate Eq. (1.15) as:

$$\mu_{\pm} \approx \frac{\sigma_0 A}{2EI} \left[1 \pm \left(1 + \frac{2EI\rho A\Omega^2}{\sigma_0^2 A^2} \right) \right], \quad (1.20)$$

by expanding the square root to the first order. If we then combine (1.20) with (1.11) and (1.15) we obtain

$$\alpha \approx \alpha_0 := \sqrt{\frac{\sigma_0 A}{EI}} \text{ and} \quad (1.21)$$

$$\beta \approx \sqrt{\frac{\rho}{\sigma_0}} \Omega. \quad (1.22)$$

⁴This holds true for all strings mentioned within this work unless specified differently.

While Eq. (1.22) can be associated with the resonance frequency of a simply supported perfect string, (1.21) can be identified with the flexural stiffness of the string [109, 110]. Next, we substitute the HTS approximation (Eq. (1.19)) into Eq. (1.22) and obtain

$$\beta l = \sqrt{\frac{\rho}{\sigma_0}} \Omega_{n,\text{HTS}} l \approx \pi n. \quad (1.23)$$

This allows us to approximate the last term of (1.17) as

$$\cos(\beta l) \approx (-1)^n$$

and thereby (1.17) simplifies to

$$\begin{aligned} & (\alpha_0^2 - \beta^2) (e^{2\alpha_0 l} - 1) \sin(\beta l) \\ & + 2\alpha_0 \beta \left[e^{\alpha l} (2 - (-1)^n e^{\alpha_0 l}) + (-1)^n \right] = 0. \end{aligned} \quad (1.24)$$

Due to the material parameters of the nano-strings used in this thesis, which will be discussed in detail in later parts (2 and 3), we find, that $\alpha_0 > 10\beta$ with $\beta l \approx n\pi > 1$ holds for all discussed samples. Thus we can assume $e^{\alpha_0 l} \gg 2$ to be well satisfied within the scope of this thesis. Under these conditions, Eq. (1.24) reduces to

$$(\alpha_0^2 - \beta^2) \sin(\beta l) - (-1)^n 2\alpha_0 \beta = 0.$$

Using $\alpha_0 \gg \beta$ we obtain

$$\alpha_0 \sin(\beta l) - (-1)^n 2\beta = 0. \quad (1.25)$$

Next, we solve for β by using (1.23) and expand $\sin(\beta l)$ around $n\pi$

$$\sin(\beta l) \approx (-1)^n (\beta l - n\pi). \quad (1.26)$$

By substituting this into Eq. (1.25), we obtain

$$\beta = \frac{n\alpha_0\pi}{\alpha_0 l - 2}. \quad (1.27)$$

As last step we identify α_0 and β using Eqs. (1.21) and (1.22) with the geometry parameters of the resonator and the resonance frequency $\Omega_n/2\pi$. We obtain

$$\Omega_{n,\text{TS}} = \frac{n\sigma_0\pi\sqrt{A/\rho}}{\sqrt{\sigma_0 A l} - 2\sqrt{EI}} = \Omega_{n,\text{HTS}} \frac{\sqrt{\sigma_0 A l}}{\sqrt{\sigma_0 A l} - 2\sqrt{EI}}. \quad (1.28)$$

This relation represents the resonance frequency of a tensile tressed nano-string with a first order correction accounting for the bending of the string. Hereby, we also show, that it is admissible to consider the center of mass motion within the framework of a harmonic oscillator, with a modal shape defined by $a(x)$ for the system of a nano-string resonator.

1.2.1 Inhomogeneous nano-strings

Up to now, we considered a homogeneous single layer string. However, within this thesis we will also discuss multi-layer strings, comprised from varying materials. These multiple layers are used to realize e.g. specific properties in magnetic materials (see Part 3). For the discussion of the mechanical properties, we consider the structure schematically shown

in Fig. 1.4 for two layers ($N_i = 2$). The lower layer $i = 1$ with a thickness t_1 is topped by the second upper layer $i = 2$ with a thickness t_2 . The scale to the right gives the thickness dependent bending radius r' . The neutral layer r_n may shift from the geometric center compared to a homogeneous string. Further, we consider only the out of plane (oop) motion, which also is the stacking direction for the multiple layers. We start with the force consideration. Expanding Eq. (1.8) to the settings of a multi-layer string, requires to consider the prestress in all layers $i \in N_i$ [114]:

$$d\vec{F}_{\text{prestress}} = d\vec{F}_{\text{prestress},1} + d\vec{F}_{\text{prestress},2} + \dots + d\vec{F}_{\text{prestress},i} = \sum_i d\vec{F}_{\text{prestress},i}$$

Condensing the individual prestresses of the layers into an effective prestress σ_{eff} , we can

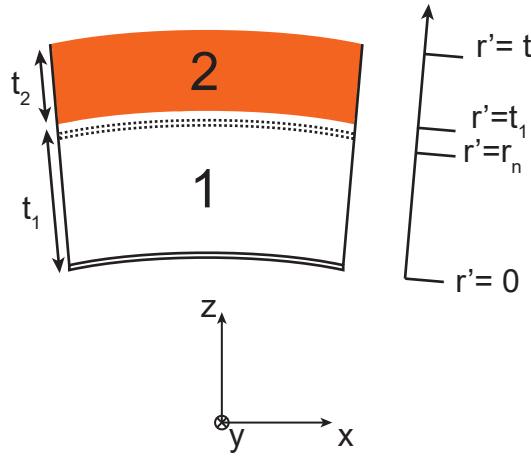


Figure 1.4: Schematic of a infinitesimal volume element of a two-layer string. The two layers 1 and 2 have corresponding thicknesses of t_1 and t_2 . Here, the layer interface is assumed to be clean and immediate. The neutral layer position may deviate from the geometric center of the string as was shown for a homogeneous string. The right hand side scale indicates the effective bending radius r' for different positions along the z -direction in the string.

formulate an equation analog to (1.7):

$$\vec{F}_{\text{prestress}} = \sigma_{\text{eff}} A dx \frac{\partial a}{\partial z} \vec{z} \quad (1.29)$$

with $A = w(t_1 + t_2 + \dots + t_i)$ and

$$\sigma_{\text{eff}} := \frac{\sigma_{0,1}t_1 + \sigma_{0,2}t_1 + \dots + \sigma_{0,i}t_i}{t_1 + t_2 + \dots + t_i}. \quad (1.30)$$

The overall effective prestress is comprised from a weighted mean of the individual prestresses in the layers according to the respective layer thicknesses [114]. In addition, we need to consider the bending moment of the multi-layer string. However, this requires that we account for the force caused by the Young's modulus E . This material parameter of the single layers E_i , translates into a parameter which depends on z (r') for the overall string $E(z)$. Also the neutral axis position r_n may have shifted from the geometric center of the string at $(t/2)$, as was the case for the homogeneous string. This shift depends on the material and mass density distribution throughout the string. We next generalize the

condition, that the total force acting on a infinitesimal volume element is the sum of the forces due to prestress and bending. Hereby, we can calculate r'_n of the multilayer string. The integral over the stress needs to vanish. Thus, together with Eq. (1.2) we obtain:

$$\int_{r'=0}^{t_1+t_2+\dots+t_i} dr' \sigma(r') = \int_{r'=0}^{t_1+t_2+\dots+t_i} dr' E(r') \frac{r' - r'_n}{r} = 0.$$

Solving for r'_n , we find:

$$r'_n = \frac{E_2 t_1^2 + 2E_1 t_1 t_2 + E_1 t_2^2}{2(E_1 t_2 + E_2 t_1)},$$

assuming a two layer system ($N_i = 2$). Here, we define the z -direction dependent Young's modulus in a piecewise fashion and treat each layer i as a material with Young's modulus E_i :

$$E(z) = \begin{pmatrix} E_1 & 0 < z < t_1 \\ E_2 & t_1 < z < t_1 + t_2 \\ \vdots & \\ E_i & \sum_{i-1} t_j < z < \sum_j t_i \end{pmatrix}.$$

The bending moment is then given by:

$$M = \int_{r'=0}^t dM = \int_{r'=0}^t E(r') w dr' \frac{(r' - r'_n)^2}{r},$$

with $t = t_1 + t_2 + \dots + t_i$. This gives us, for $N_i = 2$:

$$M = \frac{w [E_1^2 t_2^4 + 2E_1 E_2 t_1 t_2 (2t_1^2 + 3t_1 t_2 + 2t_2^2) + E_2^2 t_1^4]}{12r(E_1 t_2 + E_2 t_1)}.$$

Using the definition of the moment of inertia $I = w(t)^3/12$ [111], for an oop motion (cf. Eq. (1.13)), we can define the effective Young's modulus as⁵

$$E_{\text{eff}} = \frac{E_1^2 t_2^4 + 4E_1 E_2 t_1^3 t_2 + 6E_1 E_2 t_1^2 t_2^2 + 4E_1 E_2 t_1 t_2^3 + E_2^2 t_1^4}{(t_1 + t_2)^3 (E_1 t_2 + E_2 t_1)}. \quad (1.31)$$

Hereby, we can simplify the discussion within the Euler-equations to the effective parameters E_{eff} and σ_{eff} . The equation of motion (1.8) then reads:

$$-E_{\text{eff}} I \frac{\partial^4 a}{\partial x^4} + \sigma_{\text{eff}} A \frac{\partial a}{\partial x} = \rho_{\text{eff}} A \frac{\partial a}{\partial t}, \quad (1.32)$$

where the effective density is simply given by:

$$\rho_{\text{eff}} = \frac{\rho_1 t_1 + \rho_2 t_2 + \dots + \rho_i t_i}{t} \quad (1.33)$$

As Eq. (1.32) is designed to be fully equivalent to Eq. (1.8) by introducing effective material parameters, the resonance frequency of the out-of-plane mode of a multi-layer string can be deduced from the results describing a homogeneous string given by (1.19) or (1.28).

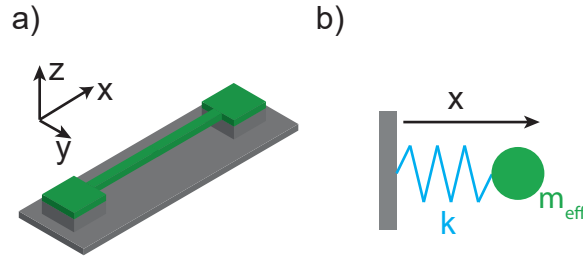


Figure 1.5: a) Schematic drawing of a double clamped suspended nano-string. b) The vibrational motion of the string shown in a) can be described in a harmonic oscillator model with spring constant k and effective mass m_{eff} .

1.3 Nanomechanical string resonators as linear harmonic oscillators

As discussed in Sec. 1.2, the motion of a three dimensional nano-string resonator can be modeled as the motion of a harmonic oscillator, characterized by a center of mass motion, an effective mass m_{eff} , and a spring constant k . Schematically this transition is shown in Fig. 1.5 from panel a) to panel b). The equation of motion, for a one-dimensional, dampened, coherently driven, harmonic oscillator is given by [113]

$$\ddot{x} + \frac{\Gamma_m}{m_{\text{eff}}}\dot{x} + \frac{k}{m_{\text{eff}}}x = \frac{F_0}{m_{\text{eff}}}\exp(-i\Omega t). \quad (1.34)$$

Here, the displacement from the equilibrium position is given by x ,⁶ Γ_m is the damping rate, k and m_{eff} are the effective spring constant and effective mass. In addition, we consider an oscillating force exciting the system with frequency Ω and amplitude F_0 . With the simple ansatz $x(t) = x_0(t)\exp(-i\Omega t)$, we obtain the well known steady-state equation of the motion:

$$x_0 = \frac{F_0/m_{\text{eff}}}{(\Omega_m^2 - \Omega^2) - i\Gamma_m\Omega}. \quad (1.35)$$

The undamped resonance frequency is typically associated with the spring constant and the effective mass via $\Omega_m = \sqrt{k/m_{\text{eff}}}$. In addition, we can relate Ω_m with the mechanical properties of the nano-string i.e. the internal prestress σ_0 and the mass density ρ_{eff} assuming the condition of a highly tensile stressed string (cf. Sec. 1.2 and 1.3). Even in the most general case, as also was shown in Sec. 1.2, the mechanical system can be represented as simple harmonic oscillator, when considering only the center of mass motion.

1.3.1 Thermal excitations

Up to now, we have discussed the simple classical excitation of an harmonic oscillator with a coherent driving force F_0 . However, the mechanisms also has the potential to excite a

⁵Please note that this expression is once again written down for $N_i = 2$.

⁶Note, that from now on we will use „ x “ as the displacement when treating a harmonic oscillator, instead of „ a “, which we used for the displacement of a string in the previous section.

mechanical motion. Some of these forces can be of a technical nature, e.g. mechanical vibrations, which we assume to be negligible in this chapter. More importantly, thermal excitations of motion will also result in a detectable mechanical displacement of the oscillators. This motion is commonly known as *Brownian motion* and intimately connected to the equipartition theorem [117]. This states that each degree of freedom contains the thermal energy of $1/2k_B T$ if its in a thermal equilibrium with its environment characterized by the bath temperature T ⁷. Here k_B is the Boltzmann constant. For any harmonic oscillator, with an effective mass m_{eff} and a resonance frequency $\Omega_m/2\pi$, this relates to [110]:

$$\frac{k_B T}{2} = \frac{1}{2} m_{\text{eff}} \Omega_m^2 \overline{x_{\text{th}}^2}.$$

The RHS of this equation corresponds to the energy in the displacement of the system. Here $\overline{x_{\text{th}}^2}$ describes the mean squared displacement of the oscillator, which is related to the mechanical spectrum via:

$$\overline{x_{\text{th}}^2} = \int_0^\infty S_{\text{xx}}(\Omega) / \pi d\Omega. \quad (1.36)$$

S_{xx} describes the displacement spectral density of the mechanical resonator. For the simple frequency response function of high-Q resonators, S_{xx} takes the form:

$$S_{\text{xx}}(\Omega) = \left(\frac{F_{\text{th}}(\Omega) / m_{\text{eff}}^2}{2\Omega_m} \right)^2 \frac{1}{(\Omega - \Omega_m)^2 + \Gamma_m^2 / 4}, \quad (1.37)$$

with $F_{\text{th}}^2(\Omega)$ the thermal driving force spectrum, given in units of force²/bandwidth i.e. $[F_{\text{th}}^2] = N^2/\text{Hz}$, and in this case associated with the temperature of the environment. For elevated temperatures with $k_B T \gg \hbar \Omega_m$, we can approximate the thermal force spectrum at the mechanical frequency as frequency independent ($F_{\text{th}}^2(\Omega) \approx F_{\text{th}}^2(\Omega_m)$). Together with (1.36) we get an expression for $\overline{x_{\text{th}}^2}$:

$$\overline{x_{\text{th}}^2} = \frac{F_{\text{th}}^2(\Omega_m)}{2m_{\text{eff}}^2 \Gamma_m \Omega_m^2}.$$

which together with the equipartition theorem allows us to give an explicit expression of the thermal driving force:

$$F_{\text{th}}^2(\Omega_m) = 2m_{\text{eff}} \Gamma_m k_B T.$$

Taken together, we can write the thermal noise spectral density as:

$$S_{\text{xx}}(\Omega) = \frac{k_B T}{2\Omega_m^2 m_{\text{eff}}} \frac{\Gamma_m}{(\Omega - \Omega_m)^2 + (\Gamma_m/2)^2}. \quad (1.38)$$

In consequence, the measurement of the thermal displacement noise can be utilized to calibrate a measurement setup and deduce the systems transduction. Thus connecting the measured observable to the displacement of the oscillator. Comparing this real, temperature dependent displacement of a nano-string in absence of all other driving forces with the actual measured power spectrum e.g. a voltage signal, allows us to calibrate the measurement setup for actual deflection of the nano-string. Exemplary this is shown in

⁷Please note, that this relation is only valid within limits. For temperatures considerably higher compared to room temperature ($T \gg 300\text{K}$) the relation needs to be adapted. The same is true if the bath temperature is too low and the oscillator is close to its quantum mechanical ground state. We will however stay within the viable range for the relation in this thesis.

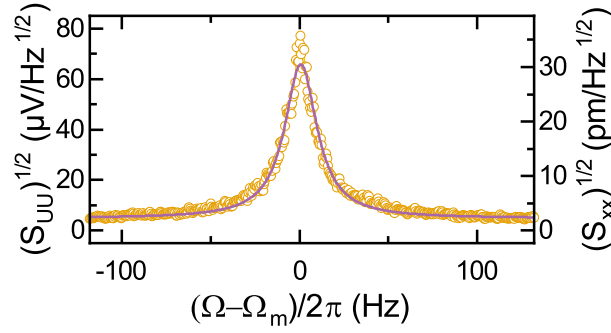


Figure 1.6: Thermal motion spectrum of the fundamental mode of a Si_3N_4 nano-string. By fitting the data with a Lorentzian line shape (cf. (1.41)), the calibration factor C , which relates the measured photovoltage to the actual mechanical displacement of the nano-string's center of mass motion, can be extracted.

Fig. 1.6, here the Brownian motion of a Si_3N_4 nano-string is shown. On the left y-axis the measured signal S_{UU} is plotted in $\mu\text{V}/\text{Hz}^{1/2}$. This measured spectrum is now related to the actual spectrum via a calibration constant

$$C = \sqrt{\frac{S_{xx}(\Omega_m)}{S_{UU}}}. \quad (1.39)$$

This allows us to calibrate the setup and sample and label the right y-axis of Fig. 1.6 with the actual nano-string deflection of several pico-meter. As a drawback, this method is highly sensitive on the setup and sample used. If a different sample is used, or if the readout setup changes, the calibration is not valid anymore. Due to the measurement setups, which will be discussed in Secs. 2.4, 3.4 and 4.4, the measured value will not depend linearly on the displacement of the center of mass motion of a nano-string. The setups are sensitive to an observable, which depends on the squared magnitude of the displacement x_0 , not the displacement itself. Therefore the measurable amplitude e.g. a photo-voltage spectrum can be described by:

$$|x_0|^2 = \frac{F_0^2/m_{\text{eff}}^2}{(\Omega_m^2 - \Omega^2)^2 + \Gamma_m^2 \Omega^2}. \quad (1.40)$$

Note, that (1.40) does not represent a simple Lorentzian response (cf. i.e. Fig. 2.13). However, for large quality factors $Q = \Omega_m/\Gamma_m$, Eq. (1.40) can be approximated by:

$$|x_0|^2 \approx \left(\frac{F_0/m_{\text{eff}}}{2\Omega_m}\right)^2 \frac{1}{(\Omega_m - \Omega)^2 + \Gamma_m^2/4}, \quad (1.41)$$

which is indeed a Lorentzian lineshape. Therefore, we expect the response spectra of the resonators to have a Lorentzian lineshape, as long as they stay in the harmonic regime (cf. 1.3.2).

1.3.2 Nonlinear effects in nano-strings

In the previous section, we treated the nano-string as a damped harmonic oscillator, in the linear response regime. This adequately describes nano-strings experiencing small displacements. For high amplitude states however, nonlinear effects can occur [111, 116].

Within this section, we present the impact of a restoring force which scales non-linearly with the displacement of the dynamical motion of the string. In particular, we discuss the situation of highly-tensile stressed nano-strings, where this restoring force originates from a geometric nonlinearity.

The geometric nonlinearity originates from higher order effects in the bending force discussed within Sec. 1.2. In particular, for the derivation of Eq. (1.5), we assumed that the prestress σ_0 is constant and therefore neglected it. For high amplitudes this approximation is no longer valid, and the prestress changes as a function of the string displacement $a(x)$ (cf. Fig. 1.2). The finite displacement lengthens the string and hereby induces the additional prestress

$$\delta\sigma = E\delta l,$$

where δl is the string stretching. Hereby, the bending force dF_{bending} becomes dependent on the string displacement. We will discuss how this can be taken into account in the equation of motion in the following. First, we need to calculate the stretching of the nano-string due to displacement. The length of the displaced string is given by [110]

$$l' = \int_{-l/2}^{l/2} \sqrt{1 + \left(\frac{\partial a(x)}{\partial x}\right)^2} dx \approx \int_{-l/2}^{l/2} \left(1 + \frac{1}{2} \left(\frac{\partial a(x)}{\partial x}\right)^2\right) dx.$$

The approximation on the right side is obtained by expanding the square root to first order, for $a'(x) \ll 1$. Further using the displacement approximation for a highly tensile stressed nano-string (cf. Eq. (1.18)) $a(x) = a_0 \cos(n\pi x/l)$ we get

$$l' = l \left(1 + \frac{n^2 a_0^2 \pi^2}{4l^2}\right). \quad (1.42)$$

This change in the total length of the string translates into an increase of the prestress σ :

$$\sigma = \sigma_0 + E \frac{l' - l}{l} = \sigma_0 + \frac{n^2 a_0^2 \pi^2 E}{4l^2}. \quad (1.43)$$

If we include this into the equation of motion of the tensile stressed nano-string (1.18), we obtain:

$$\ddot{a}(t) - \left(\frac{n\pi}{l}\right)^2 \frac{\sigma_0}{\rho} a(t) - \frac{n^2 E \pi^4}{4l^2 \rho} a^3(t) = 0. \quad (1.44)$$

This additional term, proportional to a^3 , is known as the *Duffing nonlinearity* with the *Duffing parameter*, defined as:

$$\alpha \equiv \frac{n^2 E \pi^4}{4l^4 \rho}. \quad (1.45)$$

Correspondingly, we can introduce the geometric nonlinearity in the one-dimensional equation of motion of the harmonic oscillator (1.34) and arrive at the *Duffing equation* [111,118]:

$$\ddot{x}(t) + \Gamma_m \dot{x}(t) + \Omega_m^2 x(t) + \alpha x^3(t) = \frac{F_0}{m_{\text{eff}}} \exp(-i\Omega t).$$

This equation of motion leads to an amplitude spectrum of a Duffing oscillator [118]:

$$\left[\Gamma_m^2 + 4 \left(\Omega - \Omega_m - \frac{3\alpha}{8\Omega_m} x_0^2 \right)^2 \right] x_0^2 = \frac{F_0^2}{m_{\text{eff}}^2 \Omega_m^2}. \quad (1.46)$$

In the limit of small displacements $x_0 \rightarrow 0$ Eq. (1.46) is identical to the linear response regime (see Eq.(1.35)). For large excitation forces, the displacement increases and the term $3\alpha/8\Omega_m x_0^2$ causes a modification of the mechanical response spectrum. In detail the maximum of the amplitude spectrum $x_{0,max}$ does not only get larger, but also shifts the effective mechanical resonance frequency from Ω_m to Ω_{eff} . This response spectrum is displayed in Fig. 1.7 a) for various excitation force amplitudes F_0 . Note, that for displacement amplitudes exceeding the critical amplitude x_{crit} , the spectrum becomes bistable i.e. the amplitude spectrum has more than one solution, of which maximally two are stable. Panel

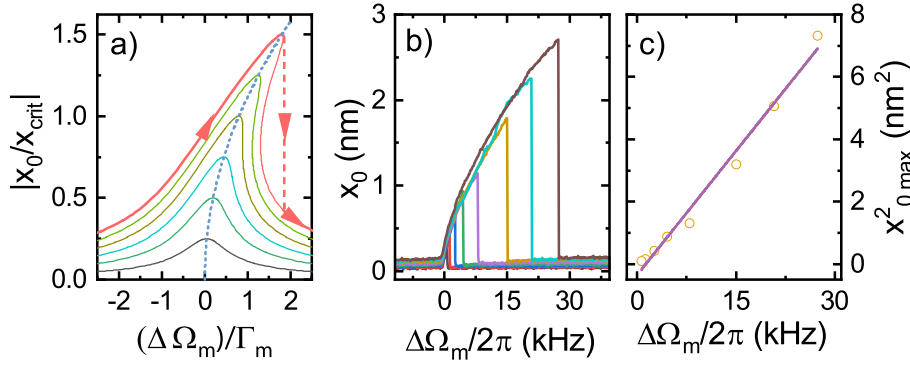


Figure 1.7: a) Amplitude of a Duffing oscillator. For amplitudes exceeding the critical amplitude x_{crit} , the response spectrum becomes bistable. When sweeping from left to right, the high amplitude branch can be accessed. In b) this is shown for the fundamental mode of a Si_3N_4 nano-string resonator for driving forces from $U_{piezo} = 7$ to 28 mV_{rms} extracted by laser interferometry (cf. Sec. 2.4.1). c) Shows the maximal mechanical amplitude for the different driving strengths extracted from the spectra in b) (backbone curve), the line is a linear fit, which allows to determine the Young's modulus (cf. (1.45) and (1.47)).

b) shows an actual measurement of a nano-string in this regime. Due to the sweeping direction of the exciting force (from lower to higher frequencies) during the measurement, it is not possible to reach the metastable amplitude states rising from the bistability, therefore the nano-string remains in the high amplitude state up to Ω_{crit} and jumps down to lower amplitudes once Ω_{crit} is surpassed. This of course is only the case if the drive frequency is swept from low to high. Thus the up sweep direction of the frequency allows to measure the high displacement amplitude response, while the reversing the frequency sweep direction gives access to the low displacement amplitude branch. The high displacement amplitude branch allows to determine the maximum displacement amplitude $x_{0,max}$ occurring at frequency Ω_{eff} . Plotting the maximum displacement amplitude as a function of $\Omega_{eff} - \Omega_m$ results in the so-called backbone curve, which allows to quantify the Duffing coefficient α (cf. Fig. 1.7c).

$$x_{0,max}^2 = \frac{8\Omega_m}{3\alpha}(\Omega_{eff} - \Omega_m). \quad (1.47)$$

Knowledge of α allows the determination of the Young's modulus. Note, that this requires quantitative knowledge about the displacement amplitude, which is obtained by prior calibration of the system, e.g. via thermal noise spectroscopy. Vice versa, if the Young's

modulus and mass density of a string are known, the Duffing backbone curve allows to calibrate the string displacement, complementary or substituting a thermal calibration (cf.1.3.1).

1.3.3 In-situ frequency tuning mechanism

We discussed the geometric nonlinearity as source of the Duffing term, which adds to the otherwise known mechanical response function. Within this section, we highlight how this feature can be used to tune the resonance frequencies of all modes of the oscillator. By recognizing, that the Duffing term corresponds to an additional stress in the system, we can immediately deduce, that the resonance frequency of a highly tensile stressed string resonator becomes tunable as (1.19):

$$\Omega_m = \frac{n\pi}{l} \sqrt{\frac{\sigma}{\rho}}.$$

Evidently, this mechanism allows to frequency tune all of the harmonics⁸ of the string. In this section we want to quantify how the resonance frequency of a mode $\Omega_m(n = 1)$ changes if one of the higher harmonics $\Omega_m(n > 1) = \Omega_{m,n}$ is driven into a high amplitude oscillation.

To discuss this mechanism in more detail, we take the expression for the additional prestress in a string due to high amplitude oscillation and the resulting string stretching (1.43) and substitute this into the expression for the resonance frequency of the fundamental mode Eq. (1.19):

$$\Omega'_m = \frac{\pi}{l} \frac{\sigma'}{\rho} \approx \Omega_m \left(1 + \frac{\Delta\sigma}{2\sigma_0} \right) \quad (1.48)$$

Using $\Delta\sigma = E\Delta l/l$ with $\Delta l = l' - l$ we can give an expression for the relative change in eigenfrequency of the fundamental mode, depending on the amplitude of a higher order mode $a_{0,n}^2$:

$$\frac{\Delta\Omega_m}{\Omega_m} = \frac{\Omega'_m - \Omega_m}{\Omega_m} = \frac{a_{0,n}^2 n^2 \pi^2 E}{8\sigma_0 l^2}. \quad (1.49)$$

The amplitude spectrum of $a_{0,n}$ is described by the Duffing spectrum (1.46). However, if we configure the system in a way, that the displacement remains in the upper branch of the bistable Duffing response, we can control its amplitude not only via the applied driving force, but also by setting the frequency of the drive Ω_{aux}

$$a_{0,n,\text{max}}^2 = \frac{8\Omega_{m,n}}{\alpha} (\Omega_{\text{aux}} - \Omega_{m,n}). \quad (1.50)$$

Note, that this amplitude control scheme is independent of the applied exciting force if $\Omega_{\text{aux}} > \Omega_{m,n}$ and within the limits of the bistability region ($a_{0,n}^3 \gg 4F_0/(3\alpha m_{\text{eff}})$ and $a_{0,n} \leq F_0/(\Gamma_{m,n} m_{\text{eff}} \Omega_{m,n})$ [71, 118]). Comparing Eqs. (1.50) and (1.47) shows a close resemblance, indicating that the backbone curve of the Duffing oscillator is actually a full description of the frequency to amplitude relation for the upper branch of the Duffing oscillator, within the bistability region. If we now combine the last two equations (1.49) and (1.50), we obtain an expression connecting the shift in the fundamental mode frequency to an auxiliary drive on a higher harmonic:

$$\frac{\Delta\Omega_m}{\Omega_m} = \frac{2}{3} \frac{\Omega_{\text{aux}} - \Omega_{m,n}}{\Omega_{m,n}}. \quad (1.51)$$

⁸We exclude the mode which is Duffing driven here, as this is more complicated.

It is notable, that the prefactor does neither depend on which higher mode is used, nor on the power of the auxiliary drive signal directly. Indirectly however, the drive power F_0 defines the bistability region and thereby limits the range of accessible frequencies for Ω_{aux} . This, together with the fact that the auxiliary drive needs to be initialized at $\Omega_{\text{aux}} \approx \Omega_{m,n}$ and then increased to the desired value of Ω_{aux} , limits which higher harmonic can be used for this frequency tuning method, depending on how far the fundamental mode frequency needs to be shifted. Also technical limitations need to be taken into account (cf. App. A.1). Experimentally we realize the tuning mechanism for up to the 11th harmonic of a nano-string [119]. Further it was shown, that the tuning mechanism does not influence the quality factor of the tuned mode [79, 80, 119]. Figure 1.8 shows three selected higher harmonics, and how far the fundamental mode can be tuned ($\Delta\Omega_m = \Omega_{\text{eff}} - \Omega_m$) using them. This gives us the possibility to in-situ tune the eigenfrequency of several nano-strings a technique which will be used to frequency tune multiple strings in a resonator network (cf. Part 2). For some technical aspects and challenges concerning this tuning mechanism please see App. A.1.

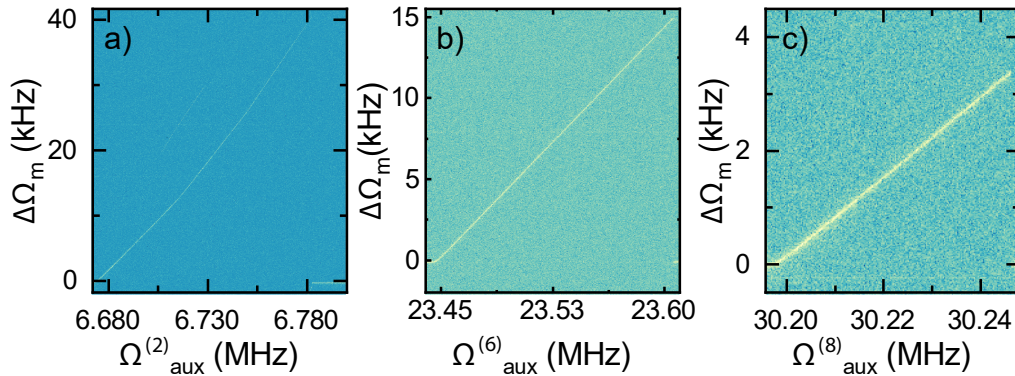


Figure 1.8: Fundamental frequency of a $80\ \mu\text{m}$ Si_3N_4 nano-string measured via laser interferometry (cf. Sec 2.4.1) while strongly driving higher harmonics. The initial frequency of the mode is at $\Omega_m = 3.33$ MHz. By sweeping the auxiliary drive at a higher harmonic $\Omega_{\text{aux}}^{(n)}$ the fundamental frequency is increased. In a) the second harmonic was used and shows a possible change in frequency of $\Delta\Omega_m \approx 40$ kHz in b) the 6th ($\Delta\Omega_m \approx 15$ kHz) and in c) the 8th harmonics were utilized ($\Delta\Omega_m \approx 3$ kHz). For higher harmonics the tuning range reduces due to the size of the Duffing bistability region. Note, that the undisturbed frequency of the mode is restored after leaving the bistability region at higher frequencies, this can be seen in the bottom right corner of each panel.

1.4 Coupling concepts in nanomechanical string resonator networks

In this thesis we mostly consider systems, where those nano-strings are coupled to other experimental degrees of freedom. For this, several coupling mechanisms can be conceived. One way, is to couple to a nano-string *externally*. This can be done e.g. by changing the way the nano-string is connected to the substrate, or by exerting a force e.g. loading the

string with molecules [51, 120, 121]. Technically, this can also be done by engineering the clamping structures as can be seen in Refs. [122, 123]. Here, the load exerted onto the string from the clamping points changes. However, in this case it was done statically and cannot be influenced in-situ during an experiment. Another approach is to do this dynamically, and use the clamping points to couple several nano-strings or their different modes to each other via a shared clamping structure [66, 70, 71, 74]. This case will be treated in part 2. There, three nano-strings are coupled by sharing one clamping point. Due to the mechanical properties of this clamping point, motion of one nano-string influences the mode shape of all other strings connected to the clamping structure. From a physical point of view, this can be described as a system of three coupled harmonic oscillators, where the motion of each string acts as an additional force onto all other strings coupled to the same shared support. This same coupling mechanism and structure also allow excitations to be transferred between strings. By in-situ tuning the frequencies of all strings, this transfer can be controlled.

The second kind of coupling can be achieved by influencing the string by changing a material parameter, or at least an effective material parameter. We refer to this as *internal* coupling, as a material parameter changes in-situ. This coupling mechanism is used in parts 3 and 4. There the coupling is facilitated by changing the material properties of the string or layers of a multi-layer string in-situ, e.g. by changing the overall tensile stress in the string via magneto-mechanical effects [79, 124]. In particular, in part 3 we influence the stress in layers of a multi-layer string by changing the magnetization. This influences the overall strain of the string. Thereby, we couple the oscillatory motion of a string to its magnetization, and facilitate a magneto-mechanical coupling. In part 4 we will use this kind of coupling to explore the impact of an electrical current passing through a nano-string onto the oscillatory motion of the nano-string and its effective material parameters.

The third way of coupling a nano-string to form a hybrid system, is by doing it via *passive* coupling. Here, the idea is that the motion of the nano-string itself influences a system or device it is a part of [91, 92, 101, 102, 104, 107, 125, 126]. This type of coupling will be discussed in part 5. There we discuss a nano-string as a part of a superconducting LC resonator. The string is integrated as a part of the resonators capacitance. Therefore, if the capacitor is charged and the string moves, its oscillatory motion leads to a mechanically compliant capacitance. The overall capacitance of the microwave circuit gains a dependence on the motion of the string. Vice versa, by charging the capacitor in a dynamic way, this can also influence the mechanical oscillation of the string. In such a system information transfer between the two resonators, the mechanical string and the microwave circuit is possible [104].

This short section, should by no means be a complete description of the used coupling concepts, but should only be seen as a short teaser of what is to be expected and seen in the following parts of this thesis, where the concepts and their realization will be discussed in depth.

1.5 Summary

In this part we introduced the concept of a nano-string as a mechanical harmonic resonator and discussed the models used to describe it. We considered the different forces acting on and within the a nanomechanical string resonator. First in a static case to take into account all forces as well as in the dynamic case, by including the influence of a driving force. Thereby discussing how an oscillating string can be described. We showed, that by using an appropriate modal shape, the center of mass motion can be considered as a harmonic oscillation. We also expanded the model for a case in which the string is no longer a homogeneous material but a multi-layer structure with different materials stacked in the oscillation direction. We further discussed how this given model needs to be expanded in the case of large mechanical amplitudes, which leads to geometric nonlinearities, and brings the string into the Duffing regime. Using this nonlinearity of the system, we showed how driving a higher harmonic of a nano-string can be used to in-situ tune the fundamental frequency of individual strings, while their quality factors remain at a high value. In the last section, we then gave a concise preview on how nano-strings will be used in the coming parts of the thesis to form hybrid systems. As parts of networks, to investigate dynamics, function as sensor platforms or integrated in superconducting circuit quantum electrodynamic (QED) devices.

PART 2

NANOMECHANICAL RESONATOR NETWORKS

2.1 Introduction

In this part of this thesis, we will consider strong coupling phenomena in nano-string resonator networks. These are comprised of high-Q Si_3N_4 nano-strings which are strongly mechanically coupled to each other in different configurations, thereby forming fully mechanical multi-level systems [70, 127–129]. These multi-level systems not only represent an important step towards larger mechanical resonator networks, e.g. for pure mechanical realizations of information processing [130–132], storage [94, 104, 133], and remote sensing applications [66, 69]. They also allow investigating several quantum-classical analogies in a range of phenomena like population oscillations [73, 127], population exchange e.g. in the form of Landau-Zener-Stückelberg like dynamics [71, 74, 134]. Almost all of these aforementioned applications require, by design, strong inter-resonator coupling. This is a necessary requirement to perform a deliberate transfer of phonons. Furthermore, the ability to control the resonance frequencies of the individual resonators in a given setup or system is often necessary. We will demonstrate all three of these key requirements in the nano-string resonator networks presented in this part.

We first consider the mathematical and theoretical foundations used for the description of the nanomechanical resonator networks in Chap. 2.2. For this we will pick up on the models used to describe single nano-string resonators in Part 1 and expand them to arbitrarily large, mechanically coupled resonator networks. We then will discuss the transition dynamics in such a system, first in the framework of a classical analogon to the Landau-Zener model and then by showing the bottom up classical approach. In Chap. 2.3 we will present the fabrication processes used to build the Si_3N_4 resonator networks. Further we will discuss the design considerations for the two presented network types. Chap. 2.4 will give a short introduction into the measurement setups and concepts used to extract the experimental data which will be shown and discussed in Chap. 2.5. Here, we will first show the characterization of the nano-string networks, including the emergence of dark-modes in the system. We will then discuss the transition dynamics in the system, in

Landau-Zener inspired experiments in detail. Here, we demonstrate the targeted excitation transfer between modes in a network. Lastly, we will summarize the findings of this part in Chap. 2.6. The groundwork for these experiments has been published in Ref. [71]. A large part of the findings to be shown here were acquired within the supervision of the Master's thesis of Thomas Luschmann [135] and partially published in Ref. [136].

2.2 Theoretical background

In part 1 of this thesis, we already discussed the physics of a single, double clamped, tensile stressed, suspended nano-string resonator. Here, we want to broaden the subject to first two and then n coupled resonators. Special care will be taken to discuss a system of three fully coupled resonators, since this will be the system considered experimentally later. In the course of this section we will first theoretically look at how multiple energy levels couple with and to each other in using the framework of the Landau-Zener model [137–141]. Then we will look into the classical pendant to this system and consider coupling and energy transfer between classical harmonic oscillators [128].

2.2.1 Landau Zener physics/ transition dynamics

We now want to take a look into the energy transmission dynamics in a system of two coupled harmonic oscillators. We start with the standard Landau-Zener formula, for energy transfer between two coupled levels. Then we will expand the description for the full three-level system, which also will be the main scope of the experimental data later on. We then will search for parameter ranges, in the three-level system in which we can simplify the system, and treat parts of it again as a standard two-level Landau-Zener system.

Lev Landau [137] and Clarence Zener [138], investigated the time evolution of a quantum mechanical system, consisting of two coupled levels. This can be generally described by a time dependent Schrödinger equation [137, 138]:

$$i\hbar \begin{pmatrix} \dot{\Psi}_1 \\ \dot{\Psi}_2 \end{pmatrix} = \mathbf{H}_2(t) \begin{pmatrix} \Psi_1 \\ \Psi_2 \end{pmatrix}, \quad (2.1)$$

with the time dependent hermitian Hamilton operator:

$$\mathbf{H}_2 = \begin{pmatrix} \epsilon_1 + b_1(t) & v \\ v^* & \epsilon_2 + b_2(t) \end{pmatrix}. \quad (2.2)$$

Here, the undisturbed energies of the levels $E_i = \epsilon_i + b_i(t)$, have a linear time dependence, and are coupled to each other with the off-diagonal elements v . For the general case of $b_1 \neq b_2$, the undisturbed levels will eventually cross at time t_c at $E_1(t_c) = E_2(t_c) \equiv E_c$. Then, the levels interact (if $v \neq 0$) and a transfer of excitation (transition) between the modes becomes possible. By calculating the eigenvalues of the Hamiltonian at $t = t_c$, we obtain the modified eigenenergies:

$$\lambda_{\pm} = E_c \pm v, \quad (2.3)$$

forming an anticrossing with a level splitting of $\lambda_+ - \lambda_- = 2v$. This process is visualized in Fig. 2.1b) where the anticrossing or avoided crossing is visible. The Landau-Zener model

quantifies the transition probability during one passage through such an avoided crossing as [138]

$$P_{\text{diab}} = 1 - P_{\text{adiab}} = \exp\left(\frac{-2\pi v^2}{\zeta}\right). \quad (2.4)$$

Here, we introduce the time dependent passage rate $\zeta = b_1 - b_2$, which defines within which time the avoided crossing is passed. P_{adiab} [137] gives the probability, with which a state transfer between the levels happens, e.g. if a state prepared at the undisturbed energy $|\Psi_1|^2 = 1 (t < t_c)$ ends up at energy of the other level afterwards $|\Psi_2|^2 = 1 (t > t_c)$ this would indicate a probability of $P_{\text{adiab}} = 1$. This is of course with the constraint, that the energy in the overall system remains constant ($|\Psi_1|^2 + |\Psi_2|^2 \equiv 1$). This transfer probability depends on the coupling strength v between the levels and the transition rate ζ . If the coupling strength is large and the transition slow, the probability for a state transfer is high (2.4), this case is called an adiabatic crossing. The other case, if the transition is fast and the coupling strength small, the probability for an energy transfer between the states is low, in this case a diabatic crossing happens. Qualitatively speaking, if the coupling between the states is non-zero, a slow/small ζ results in a small P_{dia} (or large P_{adiab}) and therefore in an adiabatic transition. Vice versa, a fast/large ζ will result in a large P_{dia} and thus a diabatic transition, the same is the case if the states are not coupled to each other. These transitions will be discussed in further detail in the next section 2.2.2, where we will consider a purely classical approach. By doing so, we will show that the effects present in the quantum mechanical description can, to a certain extend, be transferred into the classical regime and vice versa, insights gained in the classical regime can be applied for quantum systems.

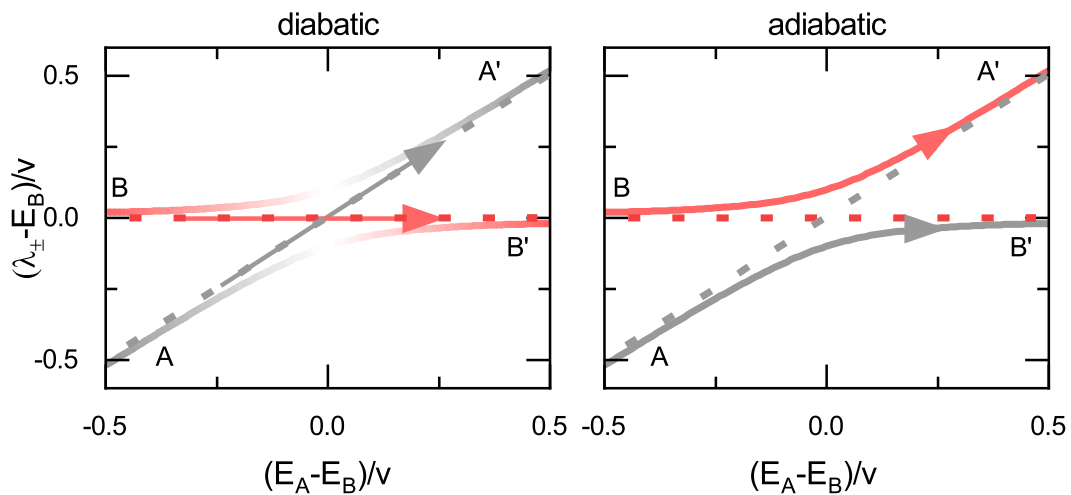


Figure 2.1: Schematic illustration of diabatic and adiabatic transitions: For fast transition rates (diabatic transition), the system passes the mode crossing diabatically without energy transfer between the modes. Thus an initial state A results in a final state A' (and respectively for B and B'). For slow rates (adiabatic) the system follows the lower branch of the mode splitting and an initial state A will result in a final state B' (respectively for B and A'). The dashed lines indicate the unmodified energies i.e. in the absence of an avoided crossing.

2.2.1.1 The three-level Landau-Zener model

After discussing the well known and experimentally also well mapped standard two-level Landau-Zener case, we next take a look into the three-level model. A system of three interacting levels can, in general, be described using the Hamiltonian [139, 141]:

$$\mathbf{H}_{(3)} = \begin{pmatrix} \epsilon_1 + b_1(t) & v_{12} & v_{13} \\ v_{21} & \epsilon_2 + b_2(t) & v_{23} \\ v_{31} & v_{32} & \epsilon_3 + b_3(t) \end{pmatrix}, \quad (2.5)$$

which is an obvious expansion of the two-level Landau-Zener case (2.2). Again the energies of the uncoupled levels are given by $E_i = \epsilon_i + b_i(t)$. However, this small extension results in a significant complication of the system. In fact Refs. [139–141] report, that an analytic description of the eigenvalues, and the transfer probabilities is no longer possible. However, for special cases, analytic solutions exist. Here we want to give two short examples of which boundaries need to be present for analytic solvability of an n -level Landau-Zener system, since we will later consider a physical system, in which we can find parameter ranges where they are applicable, as well as ranges where neither are applicable. The first case, named the *equal slope case* (cf. Fig. 2.2) by Brundobler and Elsner [140], assumes that all but one of the values of b_i are equal and positive ($b > 0$), as well as all corresponding energies are ordered $\epsilon_{i-1} < \epsilon_i < \epsilon_{i+1}$ and in particular not equal. In this case, all coupling constants $v_{i,j}$ may be non-zero, but all modes but one are initialized far detuned from each other and can therefore not couple to each other. Only one mode has the ability to change its energy and thus match with all the others, while they remain on parallel levels. This is illustrated in Fig. 2.2.

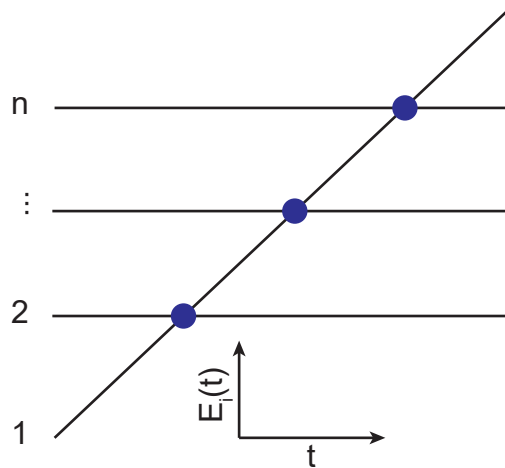


Figure 2.2: Sketch of the *equal-slope case*. All but one level have the same slope b_i and the energies are non-degenerate and ordered. Furthermore they are sufficiently separated such that the transition probability between parallel levels is negligible. Only mode 1 has a different slope and thus can match energies with all other levels respectively and therefore enables transitions (depending on ζ).

The second case, namely the *Boutie Case* (cf. Fig. 2.3) [140], describes the situation, where all levels become energetically degenerate at t_c . Here, all b_i can be different and all E_i have the same value at one specific time. However, to allow for analytical solvability,

the coupling rates $v_{i,j}$ need to be restricted in such a way, that only one degree of freedom e.g. Ψ_1 , can couple to all the others, but without them being coupled to each other ($v_{1j} = v_{j1} \neq 0$ and $v_{ij}(i, j \neq 1) \equiv 0$). E.g. a system where all modes are coupled to a central node, but not among each other. This can be seen in Fig. 2.3. These two examples

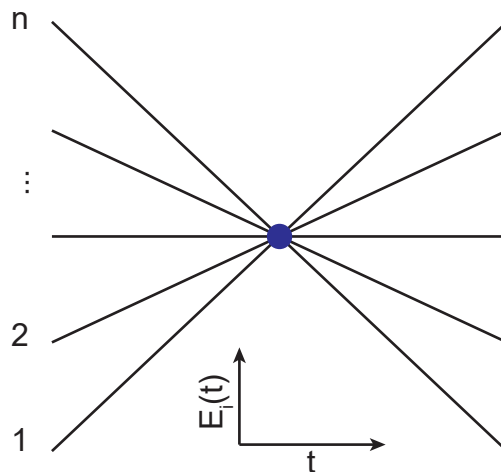


Figure 2.3: Sketch of the *Bowtie* case. All levels meet at one point with different slopes, but only one level is coupled to all the others, but they are not coupled to each other.

illustrate, that the general three-level Landau-Zener model cannot be solved analytically unless severe cuts into the generality of the model are made. In the following (cf. Sec. 2.2.2 and Sec. 2.2.2.1) we will show, that our system of three coupled nano-string-resonators can be described as a full three-level Landau-Zener system. We will further show, how it can be limited to the two analytically solvable cases presented here. Then, we will go beyond them and experimentally reach the range where no analytic solutions are viable.

2.2.1.1.1 Independent crossing approximation We remember, that for the two-level case, an analytic solution is possible, where it is not for systems with three or more levels. If we consider the solutions for the two-level case Eq. (2.3), we can see that significant amounts of energy exchange between the two states are only possible at the time where the levels cross ($E_1(t) \approx E_2(t)$) [140]. This implies, that if all crossings of exactly two levels are well separated from each other and from all other levels, we can consider them as independent. We can then treat each of them as a individual crossing, described by (2.2). This simplification is known in the literature [140] as the *independent crossing approximation (ICA)*. As a criterion to use this approximation in the thesis, we consider a crossing as independent, if the detuning between the crossing (x) and all other levels (i) $\Delta_{xi} = |E_x - E_i|$ is at least $\Delta_{xi} \geq 3 \cdot v_{xi}$ for all modes in the system not involved in the crossing¹.

¹We note, that for the later experimental application the energy detuning and coupling term here will be substituted by a frequency detuning and the corresponding coupling strength g .

2.2.2 Multiple coupled mechanical resonators

In Sec. 1.3 we discussed how a nano-string can be described using a harmonic oscillator model. Next, we discuss how inter-nano-string coupling can be described and how this coupling is realized in the discussed setting. As the first and simplest approach we assume two of those harmonic oscillators with effective spring constants $k_{A/B}$ and effective masses $m_{A/B}$. The trivial way to formulate a coupling between them, is by adding a third spring with constant K into the system. This can be imagined as shown as a sketch in Fig. 2.4, for two 1D oscillators. If we formulate the equations of motion for such a system, similar

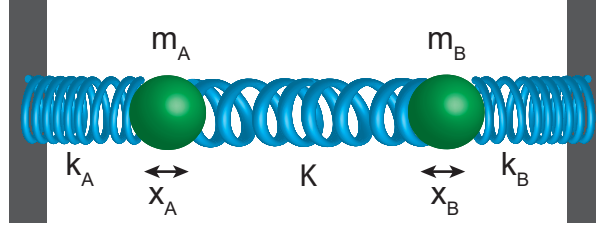


Figure 2.4: Sketch of a simple system of two coupled harmonic one dimensional oscillators. Each oscillator consists of a mass $m_{A/B}$ connected to a wall with a single linear spring with spring constant $k_{A,B}$. Additionally, the oscillators are coupled via a third spring K , connecting the two masses directly.

to Eq. (1.34), we arrive at [128]:

$$\begin{aligned} -k_A x_A + K(x_B - x_A) &= m_A \ddot{x}_A, \\ -k_B x_B + K(x_A - x_B) &= m_B \ddot{x}_B. \end{aligned} \quad (2.6)$$

Here, we did not take any external drives into account, neglected all damping mechanisms and assumed that the effective springs are not pre-tensioned, for we want to focus on the eigenfrequencies of the system. If we stay with the sketch model from Fig. 2.4, we can, without losing generality, assume that K is positive. This would amount to an attractive force between the two masses. To solve (2.6), we use an ansatz, analogous to the approach in Sec. 1.3. Here, the solutions are harmonic and of the form $x_m(t) = x_m^0 \exp(i\Omega_{\pm} t)$, with $m = A, B$, we get:

$$\begin{pmatrix} \tilde{\Omega}_A^2 & -\frac{K}{m_A} \\ -\frac{K}{m_B} & \tilde{\Omega}_B^2 \end{pmatrix} \begin{pmatrix} x_A^0 \\ x_B^0 \end{pmatrix} = \Omega_{\pm}^2 \begin{pmatrix} x_A^0 \\ x_B^0 \end{pmatrix}. \quad (2.7)$$

In this we defined $\tilde{\Omega}_i = \sqrt{(k_i + K)/m_i}$. We can now solve this equation for the eigenvalues of Ω_{\pm}^2 , obtaining the two normal modes of the system of two coupled oscillators (see also [128])

$$\Omega_{\pm}^2 = \frac{1}{2} \left[\tilde{\Omega}_A^2 + \tilde{\Omega}_B^2 \pm \sqrt{(\tilde{\Omega}_A^2 - \tilde{\Omega}_B^2)^2 + 8g^2 \tilde{\Omega}_A \tilde{\Omega}_B} \right], \quad (2.8)$$

with

$$g = \frac{\sqrt{K/m_A} \sqrt{K/m_B}}{2\sqrt{\tilde{\Omega}_A \tilde{\Omega}_B}}. \quad (2.9)$$

For the system we consider here, we further want to assume that the two oscillators are nearly identical ($m_A \approx m_B$ as well as $k_A \equiv k$ and $k_B \equiv k + \Delta k$ with $\Delta k \ll k$). For $\Delta k \rightarrow 0$, this allows approximating g to

$$g^2 \approx K^2/4(m(k + K)).$$

Thereby, relating the coupling strength mainly to the effective spring constants and masses. We now take a look into the behavior of Ω_{\pm} , depending on the detuning between the bare resonator frequencies $\Delta\Omega = \tilde{\Omega}_A - \tilde{\Omega}_B$. This mainly depends on Δk and is plotted for a small range around $\Delta k/k$ in Fig. 2.5. The frequency of oscillator A ($\tilde{\Omega}_A$) is kept constant, whereas the frequency of oscillator B ($\tilde{\Omega}_B(\Delta k)$) is increased from below $\tilde{\Omega}_A$ to above it by tuning Δk from $-k/2$ to $k/2$. The dashed lines illustrate the case of $K = 0$, here the two curves intersect at $\Delta k = 0$. The solid lines show the case of $K \neq 0$. Here, the two curves no longer intersect, instead a characteristic avoided crossing or anticrossing is visible. For

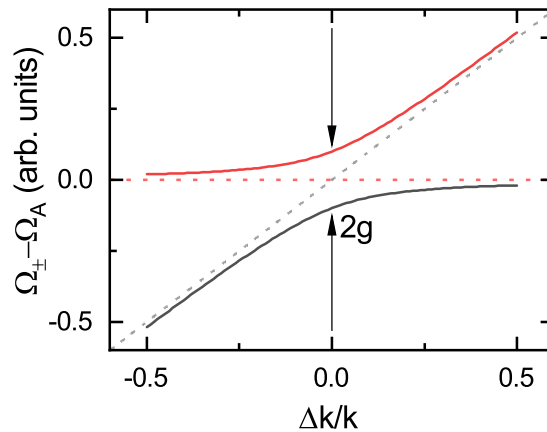


Figure 2.5: Eigenfrequencies of two coupled oscillators close to the resonance. The frequency splitting between the lower Ω_- and upper branch Ω_+ scales linearly with the coupling strength $g(K)$. The dashed lines show the behavior if $K = 0$, in this case the frequencies intersect at $\Delta k = 0$.

the case of $\Delta\Omega = 0$, the frequency splitting, visible as the difference between Ω_+ and Ω_- is simply given by $2g$. This relation is often used in experiments to determine the value of g , and we will do so in 2.5.1.

We now want, analogous to the Landau-Zener model, investigate what happens if one of the oscillator parameters changes in time, and the oscillators become degenerate. For this, we will follow the arguments put forward by L. Novotny [128]. Similar to the Landau-Zener case described in Sec. 2.2.1, to see the frequency splitting in Fig 2.5, the resonance frequencies need to change over time. In this approach, we facilitate this by tuning $\Delta k/k$ from $-1/2$ to $1/2$. Therefore, Δk becomes a function of time $\Delta k(t)$. If we initially start at $\Delta k/k = -1/2$ on the lower branch in Fig. 2.5 (Ω_-) and slowly increase Δk , the system will follow the same curve and we will end up still in the lower branch at $\Delta k/k = 1/2$. The same is true if we start on the upper branch Ω_+ .

This scenario is referred to as an *adiabatic transition*, which is defined along the lines of the Landau-Zener model 2.2.1. Thus, by dynamic tuning of the frequencies Ω_A or Ω_B , it

is possible to transfer energy from one oscillator to the other by slowly tuning the coupled system through resonance [128]. As e.g. the lower branch Ω_- can be associated with resonator B far to the left from the avoided crossing, but it is associated with resonator A on the other far right side of the avoided crossing. For a quantitative description we refer to the normal mode picture, which requires the introduction of normal coordinates (x_+, x_-) [128]:

$$\begin{aligned} x_A(t) &= x_+(t) \sin(\beta) + x_-(t) \cos(\beta), \\ x_B(t) &= x_+(t) \cos(\beta) - x_-(t) \sin(\beta), \end{aligned} \quad (2.10)$$

where β is given by $\tan(\beta) = (\Omega_B^2 - \Omega_+^2)/(\kappa/m_B) = -(\Omega_A^2 - \Omega_-^2)/(\kappa/m_A)$. If we substitute (2.10) into (2.6), we obtain:

$$\begin{aligned} \ddot{x}_+(t) + \Omega_+^2 x_+(t) &= 0 \\ \ddot{x}_-(t) + \Omega_-^2 x_-(t) &= 0. \end{aligned} \quad (2.11)$$

Which represent two independent harmonic oscillators. This gives us a set of coordinates x_+, x_- in which they oscillate independently with Ω_- and Ω_+ . Now we imagine a slow transition from $\Delta k/k = -1/2$ to $\Delta k/k = 1/2$. Initially $(\Omega_A - \Omega_-) \gg g$ and thus $\beta \approx -\pi/2$. If we put this into Eq. (2.10) and assume that initially only resonator A is excited, the energy of the system is fully associated with the normal mode x_+ ($x_- = 0$). If we now tune Δk past resonance, we have $(\Omega_A - \Omega_-) \ll g$ and $\beta \approx 0$ and thereby x_+ now fully coincides with resonator B, thus the energy is transferred from resonator A to resonator B if the system is slowly tuned through resonance. To look at this analytically, if Δk changes in time, then by definition k_B , Ω_B and Ω_{\pm} do as well. If we now assume a slowly varying $\Omega_{\pm}(t)$ in Eqs. 2.11 we find [128]:

$$x_{\pm}(t) = x_{\pm}(t_i) \text{Re} \left\{ \exp \left(i \int_{t_i}^t \Omega_{\pm}(t') dt' \right) \right\}, \quad (2.12)$$

with the ansatz $x_{\pm}(t) = x_{\pm}(t_i) \exp(i\nu t)$ and $d\nu^2/dt^2 \ll (d\nu/dt)^2$. Thereby Eq. 2.12 describes the *adiabatic* evolution of the normal modes.

Next we need to discuss what happens if Δk changes rapidly. For this we take the ansatz [128]:

$$\begin{aligned} x_A(t) &= x_0 c_A(t) \exp(i\Omega_A t) \\ x_B(t) &= x_0 c_B(t) \exp(i\Omega_B t), \end{aligned} \quad (2.13)$$

and once again, assume that initially only resonator A is active ($c_B(t = -\infty) = 0$). Also, the amplitude x_0 is given as a normalization constant ensuring $|c_A|^2 + |c_B|^2 = 1$, where $c_{A/B}$ are the time dependent amplitudes of the two oscillators. As in the adiabatic case, we substitute (2.13) into (2.6) and obtain the coupled differential equations:

$$\begin{aligned} \ddot{c}_A + 2i\Omega_A \dot{c}_A &= (K/m_A) c_B \\ \ddot{c}_B + 2i\Omega_B \dot{c}_B + (\Omega_B^2 - \Omega_A^2) c_B &= (K/m_B) c_A. \end{aligned} \quad (2.14)$$

Please note the time dependence of Ω_B . For weak coupling between the oscillators, the amplitudes $c_{A/B}(t)$ vary slow in time, compared to the oscillatory term $\exp(i\Omega_A t)$ in (2.14). Therefore, $\ddot{c}_A \ll i\Omega_A \dot{c}_A$ as well as $\ddot{c}_B \ll i\Omega_B \dot{c}_B$, which allows us to neglect the second order derivatives in (2.14) and thus obtain

$$2i\Omega_A \dot{c}_A = (K/m_A) c_B, \quad (2.15)$$

$$2i\Omega_A \dot{c}_B + [\Omega_B(t)^2 - \Omega_A^2] c_B = (K/m_B) c_A. \quad (2.16)$$

We can now combine (2.15) and (2.16) and find

$$\ddot{c}_A - i\dot{c}_A \left[\frac{\Omega_B^2(t) - \Omega_A^2}{2\Omega_A} \right] + c_A \frac{\kappa^2/(m_A m_B)}{4\Omega_A^2} = 0. \quad (2.17)$$

In this, we recognize $g^2 = \kappa^2/4(m_A m_B \Omega_A^2)$, for the interval of interest close to the anti-crossing region ($\Omega_A \approx \Omega_B$). Under the assumption, that the frequency difference between oscillators A and B changes linearly in time near the anticrossing

$$\xi t = (\Omega_B(t) - \Omega_A). \quad (2.18)$$

As can be seen from Eq. (2.18), the avoided crossing is passed at $t \approx 0$. Further, the frequency difference is negative before this time ($t < 0$) and positive afterwards. With this, we can approximate (2.17) into [128]:

$$\ddot{c}_A - i\dot{c}_A \xi t + c_A g^2 = 0.$$

This equation has no analytical solution [128], however we can find a solution for the interesting regime long after the passage of the avoided crossing $c_A(t \rightarrow \infty)$:

$$c_A(\infty) = \exp\left(-\frac{\pi}{\xi} g^2\right),$$

which gives us, due to the energy of the oscillator A being $E_A \propto |c_A|^2$ the probability for level a population transfer during a crossing analogous to the quantum Landau-Zener case(2.4):

$$P_{\text{diab}} = \exp\left(-\frac{2\pi}{\xi} g^2\right). \quad (2.19)$$

This shows, that the classical system of two coupled harmonic oscillators behaves the same way as the quantum mechanical pendant described by the Landau-Zener formalism, as we can identify the coupling strength g and transition rate ξ with the coupling strength v and transition rate ζ from Eq. (2.4). Therefore, we can now adapt the two-level Landau-Zener Hamiltonian (2.2) to the frequency picture we used in this section, obtaining:

$$\mathbf{H}_2 = \hbar \begin{pmatrix} \Omega_A(t) & g_{AB} \\ g_{BA} & \Omega_B(t) \end{pmatrix}. \quad (2.20)$$

2.2.2.1 N coupled resonators

In this last section, we discussed a model of two linearly coupled, harmonic, one-dimensional oscillators. We will now, very briefly, sketch how this can be extended to N coupled resonators². For this we generalize Eq. (2.6) for a harmonic oscillator with an index $i \in [1, N]$ and corresponding mass m_i [142]:

$$m_i \ddot{x}_i = F_i = -k_{ii} x_i + \sum_{i,j}^N \kappa_{ij} (x_i - x_j). \quad (2.21)$$

Again, we neglected all external drive and damping terms at this moment. k_{ij} is the coupling between resonator i and j if $i \neq j$. k_{ii} is the effective spring constant or stiffness of the resonator i . By introducing a generalized stiffness k_{ij} as:

$$k_{ij} = \frac{\partial F_i}{\partial x_j}, \quad (2.22)$$

²Please note, that we later perform experiments with $N = 3$.

we are able to write the N differential equations, using Eq. (2.21) on a network of N resonators in a more concise matrix form:

$$\mathbf{M}\ddot{\vec{x}} = \mathbf{K}\vec{x},$$

for which we defined \mathbf{M} as the diagonal matrix, with masses m_n on the diagonal, \mathbf{K} as the stiffness matrix with entries k_{ij} , and \vec{x} as the displacement vector containing the single displacements x_n .

$$\mathbf{M} = \begin{pmatrix} m_1 & 0 & \dots & 0 \\ 0 & m_2 & \dots & 0 \\ \vdots & 0 & \ddots & 0 \\ 0 & \dots & 0 & m_i \end{pmatrix}, \mathbf{K} = \begin{pmatrix} k_{11} & k_{12} & \dots & k_{1i} \\ k_{21} & k_{22} & \dots & k_{2i} \\ \vdots & \vdots & \ddots & \vdots \\ k_{i1} & \dots & \dots & k_{ii} \end{pmatrix}, \vec{x} = \begin{pmatrix} x_1 \\ x_2 \\ \vdots \\ x_i \end{pmatrix}.$$

Here, we assume the inter resonator coupling to be linear, and reciprocal $k_{ij} = k_{ji}$. Therefore \mathbf{K} is symmetric. Analogously to the approach in 2.2.2, we take the ansatz $x_i(t) = x_i^0 \exp(i\Omega_i t)$ and can therefore derive an eigenvalue equation for Ω^2 and the eigenvector $\vec{x}_0 = (x_1^0 \dots x_n^0)^T$:

$$-\Omega^2 \mathbf{M}\vec{x}_0 = \mathbf{K}\vec{x}_0. \quad (2.23)$$

This Eq. (2.23) presents a generalized eigenvalue problem, it can be solved for N , not necessarily degenerate, eigenvalues Ω_λ . In addition, we expect the existence of up to N , linearly independent eigenvectors $\vec{x}_{0,\lambda}$. Each of these pairs of eigenvalues and eigenvectors describes one normal mode of the coupled network. The problem can be simplified using theorems of linear algebra [143] and the knowledge, that \mathbf{K} is real and symmetric and \mathbf{M} is real and positive-definite. We then arrive at a eigenvalue problem with exactly N distinct normal mode solutions for the network. This system, similar to the two-level case can be described by a pendant to the three-level Landau-Zener Hamiltonian given by:

$$\mathbf{H}_{(3)} = \begin{pmatrix} \Omega_A(t) & g_{AB} & g_{AC} \\ g_{BA} & \Omega_B(t) & g_{BC} \\ g_{CA} & g_{CB} & \Omega_C(t) \end{pmatrix}, \quad (2.24)$$

showing that all statements taken in Sec. 2.2.1.1 concerning the three-level quantum system can be applied to a network of three coupled classical resonators. As already stated in Sec. 2.2.1.1, an analytical solution of the full Hamiltonian is not possible. However we will discuss an example of how the system can be treated numerically.

2.2.2.1.1 Numerical treatment for a three-level system We will now derive the differential equations for the case of $N = 3$. These will also be used to model population transition dynamics of three-resonator networks according to the measurement protocols used in Sec. 2.5.2. The following is an expansion of the model used in Ref. [71] to three-level systems.

We start with the equations of motion for $N = 3$ according to (2.21), with the addition of linear damping terms Γ_i as well as an external driving force F_{drive} .

$$m_A \ddot{x}_A + m_A \Gamma_A \dot{x}_A + k_{AA} x_A = k_{AB}(x_B - x_A) + k_{AC}(x_C - x_A) + F_{\text{drive}} \quad (2.25)$$

$$m_B \ddot{x}_B + m_B \Gamma_B \dot{x}_B + k_{BB} x_B = k_{AB}(x_A - x_B) + k_{BC}(x_C - x_B) + F_{\text{drive}} \quad (2.26)$$

$$m_C \ddot{x}_C + m_C \Gamma_C \dot{x}_C + k_{CC} x_C = k_{CB}(x_B - x_C) + k_{AC}(x_A - x_C) + F_{\text{drive}} \quad (2.27)$$

We now assume three almost identical nano-strings, which will be the case for the devices investigated later, and thus set $\Gamma_A = \Gamma_B = \Gamma_C$ as well as $m_A = m_B = m_C$. Without losing generality, we will now assume that string A is excited and controlled in the measurement. Therefore its eigenfrequency will be time dependent $\tilde{\Omega}_A(t)$. And we will further assume, that it will be tuned upwards by $\Delta\tilde{\Omega}_A$ in time τ . We can define $\tilde{\Omega}_A(t)$ as follows

$$\tilde{\Omega}_A(t) = \begin{cases} \tilde{\Omega}_A^0 & t < t_0 \\ \tilde{\Omega}_A^0 + \zeta(t - t_0) & t_0 \leq t \leq t_0 + \tau \\ \tilde{\Omega}_A^0 + \Delta\tilde{\Omega}_A & t \geq t_0 + \tau. \end{cases} \quad (2.28)$$

Using $\zeta = \Delta\tilde{\Omega}_A/\tau$. Similar to the experimental measurements in Sec. 2.5.2, string A is excited by a short pulse t_p with an oscillating force at the frequency $\tilde{\Omega}_A^0$. As $t_p < t_0$, we can write $F_{\text{drive}}(t) = F_0 \exp(i\tilde{\Omega}_A^0 t) \Theta(t_p - t)$, where $\Theta(t)$ is the Heaviside step function. We now use the ansatz $x_i(t) = x_0 c_i(t) \exp(i\tilde{\Omega}_A(t)t)$ with ($i = A, B, C$) and the time dependent amplitude coefficients c_i with $|c_A|^2 + |c_B|^2 + |c_C|^2 = 1$ (cf. Sec. 2.2.2). We also use the definition of the generalized stiffness (2.22) to introduce $\tilde{\Omega}_{B,C}^2 = k_{BB,CC}/m$ as the resonance frequencies of resonators B and C. Please note, that we use the time dependent resonance frequency $\tilde{\Omega}_A(t)$ associated with string A in the harmonic solution for all three equations of motion. This is possible as long as $|\tilde{\Omega}_A(t) - \tilde{\Omega}_{B,C}| \ll \tilde{\Omega}_{B,C}$, which holds in general for the modeled systems and in particular close to the corresponding avoided crossing where the population transfer takes place and $\tilde{\Omega}_A(t) = \tilde{\Omega}_{B,C}$. With this, we obtain

$$\ddot{c}_A + G(t)\dot{c}_A + (F(t) + \tilde{\Omega}_A^2(t))c_A = \frac{k_{AB}}{m}c_B + \frac{k_{AC}}{m}c_C + \frac{F_0}{mx_0}\Theta(t_p - t) \quad (2.29)$$

$$\ddot{c}_B + G(t)\dot{c}_B + (F(t) + \tilde{\Omega}_B^2)c_B = \frac{k_{AB}}{m}c_A + \frac{k_{BC}}{m}c_C + \frac{F_0}{mx_0}\Theta(t_p - t) \quad (2.30)$$

$$\ddot{c}_C + G(t)\dot{c}_C + (F(t) + \tilde{\Omega}_C^2)c_C = \frac{k_{AC}}{m}c_A + \frac{k_{BC}}{m}c_B + \frac{F_0}{mx_0}\Theta(t_p - t), \quad (2.31)$$

by defining the functions

$$F(t) = (i\dot{\tilde{\Omega}}_A t + i\tilde{\Omega}_A)^2 + 2i\dot{\tilde{\Omega}}_A + \Gamma(i\dot{\tilde{\Omega}}_A t + i\tilde{\Omega}_A) \\ G(t) = 2i(i\dot{\tilde{\Omega}}_A t + \tilde{\Omega}_A) + \Gamma.$$

We now approximate these equations, by neglecting the second derivatives \ddot{c}_i in Eqs. 2.29-2.31. This is possible, because the coupling rates are much smaller than the stiffness of the resonators ($k_{ij} \ll k_{ii} \forall ((i, j) \in (A, B, C)^2) \wedge i \neq j$). Therefore, we assume the coefficients $c_i(t)$ to vary much slower in time than the oscillatory motion ($\propto \exp(i\tilde{\Omega}_A(t)t)$ cf. Sec. 2.2.2 for the two-level case). We thus arrive at the final form of the equations, which are used for numerical calculations of the population transfer dynamics shown in Sec. 2.5.2:

$$G(t)\dot{c}_A + (F(t) + \tilde{\Omega}_A^2(t))c_A = \frac{k_{AB}}{m}c_B + \frac{k_{AC}}{m}c_C + \frac{F_0}{mx_0}\Theta(t_p - t) \quad (2.32)$$

$$G(t)\dot{c}_B + (F(t) + \tilde{\Omega}_B^2)c_B = \frac{k_{AB}}{m}c_A + \frac{k_{BC}}{m}c_C + \frac{F_0}{mx_0}\Theta(t_p - t) \quad (2.33)$$

$$G(t)\dot{c}_C + (F(t) + \tilde{\Omega}_C^2)c_C = \frac{k_{AC}}{m}c_A + \frac{k_{BC}}{m}c_B + \frac{F_0}{mx_0}\Theta(t_p - t). \quad (2.34)$$

2.3 Device design and fabrication

In this section, we discuss the fabrication of the Si_3N_4 nano-strings used in the experiments, and the considerations of how to implement a system of multiple coupled nano-strings. The fabrication of double clamped nano-string resonators used within this thesis is based on the processes developed by Matthias Pernpeintner during his PhD [144]. The processes were modified to the demands of networks containing multiple coupled strings and to improve the yield of fabricated nano-string networks.

2.3.1 Device fabrication

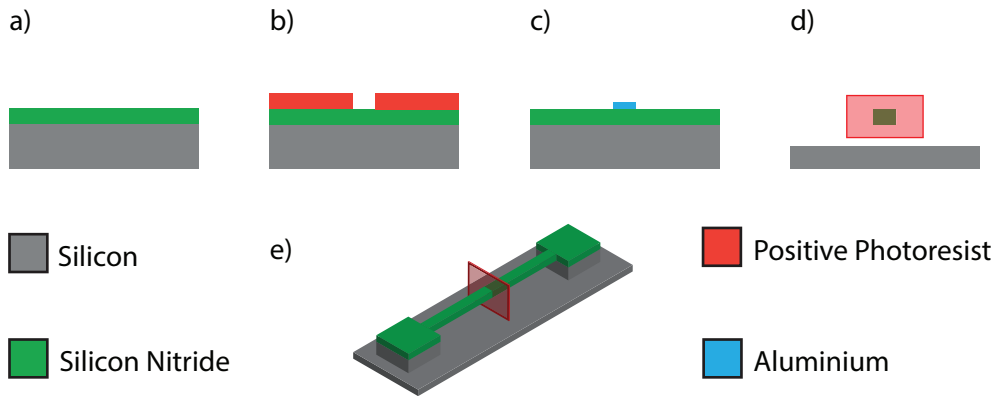


Figure 2.6: Schematic of the fabrication of a double clamped Si_3N_4 nano-string on a silicon substrate. The process starts with a mono crystalline silicon wafer a) topped with a 90 nm thick Si_3N_4 film, by commercial LPVA. In the next step b), the wafer is coated with a positive resist, and a negative of the pattern is defined by electron beam lithography. c) A thin aluminum layer is deposited and with a lift-off process the pattern is now defined in a metal hard mask. d) By first removing the surplus Si_3N_4 from the wafer using an anisotropic RIE process and then a following isotropic RIE process, the string is released from the Si substrate. e) The aluminum mask is removed by wet chemical etching resulting in the doubly clamped suspended Si_3N_4 string is finished.

The fabrication of tensile stressed Si_3N_4 nano-strings starts with a single crystalline Si wafer, on which 90 nm of Si_3N_4 have been deposited commercially via low pressure vapor deposition (LPVD) (see Fig. 2.6 a)). This deposition method results in a high intrinsic tensile stress in the Si_3N_4 film in the range of several GPa [11], which will be reduced by the patterning and etching steps to several hundred MPa. As shown in Fig. 2.6 b) and c), we use electron beam lithography and a positive resist to define a negative mask. We then evaporate a 30 nm thick layer of aluminum, by electron beam evaporation, to define the metal hard-mask, via a lift off process. This mask is then used to transfer the pattern into the Si_3N_4 via an anisotropic Ar/ SF_6 reactive ion etching (RIE) step, where the Si_3N_4 is removed around the area protected by the metal mask. A subsequent isotropic RIE step releases the Si_3N_4 nano-strings from the Si substrate (Fig. 2.6 d/e)). In the last step, the hard mask is removed with a wet chemical etching process and the sample is cleaned and dried. For samples, where a high yield of nano-strings is required, a critical point drying (CPD) process is used. This reduces the effect of strings being torn or bent to the

substrate by the capillary forces caused by evaporating solvents, an effect that is more prevalent for longer and thinner strings, and also depends on the overall tensile stress in the material³.

2.3.2 Device design

We next discuss device configurations of three coupled nano-strings. It has been shown, that coupling two strings using a shared support structure is possible and feasible [69, 79]. We will later use the geometric nonlinearity tuning mechanism discussed in Sec. 1.3.3, to frequency tune the strings within a network. While this concept was developed in [71], we now need to adapt the tuning to a three-level system. This leads to an increase in the number of auxiliary drive tones needed to control the whole system. Further frequency crowding becomes more of an issue. Here, we discuss several different sample designs and relate them to the resulting coupling matrix \mathbf{K} . Since the in-situ tunability of the

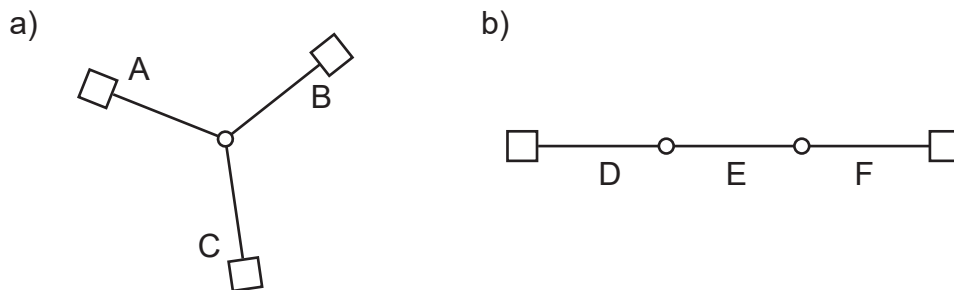


Figure 2.7: The two used sample designs. a) A fully coupled network of three strings coupled via a central shared support structure. In both cases the single strings are designed to be identical. The large rectangular clamping pads on the outside can be assumed as fix, whereas the small circular support structures mediate the coupling between the connected strings. b) A linear chain of three resonators, using the same clamping and coupling approach as in a).

resonance frequencies is possible, we found a highly symmetric approach to be the most promising. One in which all inter-resonator couplings are present and where the physical difference between the single strings is as small as technically achievable. Therefore, the system resembles a star shape of equally spaced Si_3N_4 , identical strings surrounding a central, shared support structure, mediating the coupling. The design idea is displayed in Fig. 2.7 a) and will be referred to later as the *star shaped* design. The shape and dimension of the coupling element allows to modify the inter-string coupling strength [135] and yielded, that a circular support with a diameter of $2\ \mu\text{m}$ has the optimal coupling properties. We attribute this to the under etching of the support, as this dictates how strong the support structure is connected to the substrate and thus how rigid it is. If the support structure is too rigid, it will not allow any coupling between the connected strings, whereas if its not rigid enough, there will be no separation between the strings. For the experiments we use the resonator network design depicted in Fig. 2.8. Here, three $30\ \mu\text{m}$ long and $300\ \text{nm}$ wide Si_3N_4 strings are coupled to a coupling element with an outer

³Please note, that this is mostly the case for pure metal nano-strings which will only be considered briefly in 5.

diameter of $2\ \mu\text{m}$ and a support column of $\approx 1\ \mu\text{m}$. The strings are angled by 120° with respect to each other. By using this design, we achieve an inter-string coupling between all strings of the network with $k_{12} \approx k_{23} \approx k_{31}$ for the *star shaped* case. In panel a) of Fig. 2.8 the whole network consisting of three coupled strings is visible in a tilted view. In the tilted zoom-in of the central coupling pad Fig. 2.8 b), the high acceleration voltage

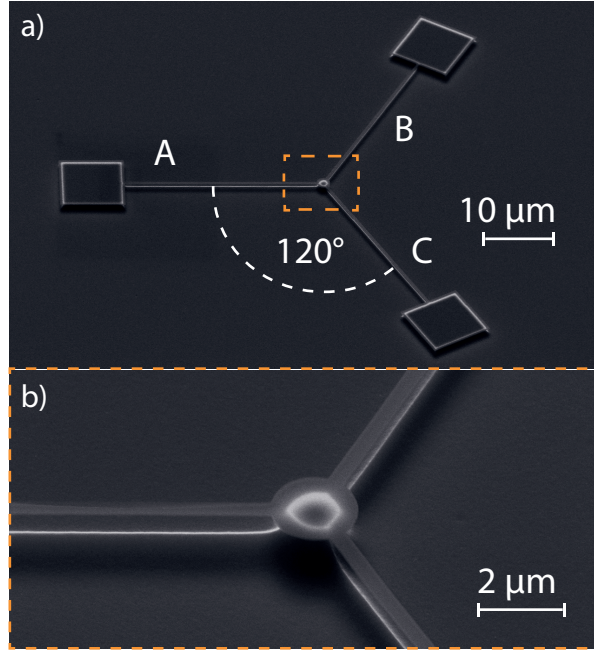


Figure 2.8: SEM image of a star shaped Si_3N_4 nano-string network, fabricated as described in Sec. 2.3.1. a) Three nano-strings are placed around a central clamping pad in an equiangular manner. b) Zoom-in featuring the central clamping pad, showcasing the partial under-etch of the pad.

used in the SEM, allows to see the partial under-etching of the circular pad. However, a quantification of the under-etched volume proves challenging. Furthermore a sharp ridge beneath the strings is clearly visible. This is a residue of the RIE process and a clear indication of the full suspension of a nano-string.

For comparison, we study a three resonator network in a linear arrangement (see Fig. 2.7b)). Here, we prepare a situation, where $k_{12} \approx k_{23}$ and $k_{13} = 0$, which is vastly different to the previous case. We will discuss the differences in detail in the following (see Sec. 2.5). In the course of this part we will refer to it as the *in-line* design.

2.4 Measurement setups

In this chapter, we present the experimental setups used for investigating the eigenfrequencies of the string networks and the dynamics of the population transfer. All experiments presented in this part are based on optical interferometry of the displacement of the individual nano-strings. In addition, we discuss the different data acquisition techniques employed to probe the sample properties and the means of how to interact with the sample and control the string frequencies.

2.4.1 Optical interferometry

To investigate the mechanical displacement of the Si_3N_4 nano-strings, we employed a free space optical interferometer. Here we only present a simplified depiction of the operating principle of the interferometer (cf. Fig. 2.9). The full details are presented in App. B.1. The interferometer uses a single-mode diode laser with a wavelength of 633 nm. After conditioning of the laser beam, it passes a beam splitter and is focused on the sample string using a commercial optical microscope objective. The interference of the light transmitted through the Si_3N_4 nano-string, which is partly reflected by the silicone substrate and the part which is directly reflected by the nano-string results in an intensity modulation on the photo detector. This intensity modulation encodes the displacement of the nano-string [145], which is later analyzed using spectral analysis, vector analysis or time domain recording schemes. The chip containing the nano-string is mounted on a xyz -piezo stage to allow precise positioning of the selected nano-string in the focal point of the laser. In addition, a piezo-shaker underneath the chip allows to apply coherent forces or superpositions of coherent oscillating forces to drive the dynamics of the nano-string. The whole sample stage is held in a vacuum chamber ($p < 0.01$ Pa), to prevent the negative influence of air-damping on the nano-strings [115]. Optical access is possible by using a 635 nm Koehler illumination, combined with a camera.

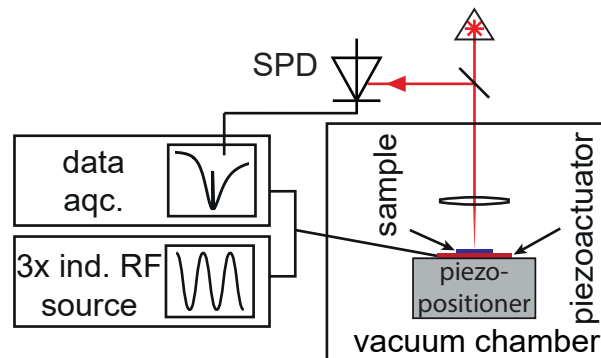


Figure 2.9: Schematic of the measurement setup. The optical interferometer is used to focus the laser spot onto the sample. The sample position is controlled with a piezo xyz -positioner inside a vacuum chamber. External drive tones from the RF sources used for in-situ frequency tuning as well as the signals necessary for the data acquisition setup are sent to a piezo actuator onto which the sample is glued. The reflected laser light, which is modulated by the nano-string displacement, leads to an intensity modulation at the photo detector. This encoded information on the displacement is later analyzed by various means.

2.4.2 Frequency domain setup

To characterize the system with all the resonance frequencies and Q -factors, the coupling strengths between the strings as well as to show the full in-situ control over the string network, we use a frequency domain (FD) setup. On one side, we use the thermal force of the environment to excite the strings motion, and a spectrum analyzer (SA) to measure the pure thermal motion spectra (cf. Fig. 2.10). On the other side, we use a vector

network analyzer (VNA) to send a weak oscillating force as a drive signal to the sample via the piezo actuator and compare this to the measured driven mechanical response of the string. In both cases the signal from the photo detector is amplified before processing to optimize the signal-to-noise performance for the chosen configuration (VNA or SA). For the full setup schematic please see B.1. The data obtained from both VNA and SA measurements looks very similar, as they both resemble the mechanical susceptibility for a string. However, the physical concepts, as well as the technical realization behind the two measurement techniques differs vastly. In the SA measurements the thermal noise spectrum is recorded and we obtain the spectral noise density of the observed string. For this the string is only excited by the thermal energy of the environment, commonly known as Brownian motion. On the other side the VNA measurements detect the displacement amplitude of a string. For this, the susceptibility of the string to a globally applied driving force is of importance. To characterize the nano-strings and the nano-string-network as a whole, we use both techniques jointly. We use a VNA measurement to roughly detect the string's eigenfrequency. By applying a large driving force, the displacement of the string increases and so does the modulation of the laser light and in turn the observable feature in the data. This allows us to detect the string frequency in a large frequency range. Note, that a large driving force leads to nonlinear behavior in the system (cf. Sec. 1.3.2), therefore it is not feasible to use this method to obtain the intrinsic frequency $\Omega^0/2\pi$ and linewidth $\Gamma/2\pi$ of a nano-string. To extract those values and to link the intensity at the photo detector with an actual displacement of the string, we use SA measurements to conduct a thermal calibration of the system (cf. Sec. 1.3.1). We use SA measurements to characterize the string and string network parameters (such as inter-string coupling), since the VNA measurements always directly drive at the mode frequency of the string under observation, whereas coupled strings are not influenced in this way. Therefore, even if we can detect all modes at the same time in a VNA measurement, the extracted values for the single modes are only partially comparable. In a more general view, there is one drawback to the SA measurements. This is the signal-to-noise ratio, which among other, depends on the number of excitations in a string. Considering a fixed measurement setup, this is limited by the environmental temperature. In a VNA measurement on the other side, it is possible to counteract a low signal-to-noise ratio by increasing the measurement power and thus the driving force on the string. However, nonlinear effects in the system need to be accounted for⁴. In both cases, and in the following time domain setup, the frequencies of the three strings in the network were partially or fully in-situ controlled by three additional RF sources using the tuning mechanism introduced in Sec. 1.3.3. This relies on strongly driving and tuning the a higher harmonic of the strings to increase the fundamental eigenfrequencies. Please note, that these auxiliary drives may not intersect in frequency and that the tuning range differs for different harmonics (see Sec. 1.3.3). Please note further, that this mechanism can only be used to tune the eigenfrequency above the intrinsic value. Technically the auxiliary drive forces are supplied by individual RF sources. The single signals are combined together with an optional measurement signal (for VNA measurements) using a power combiner. The sum signal is then sent to the piezo actuator onto which the sample chip is mounted. The two setups are shown as a sketch in Fig. 2.10

⁴Note, that the signal-to-noise ratio of the sample and setup can be too small for a SA measurement to be feasible, in this case the VNA measurements still allow collecting data.

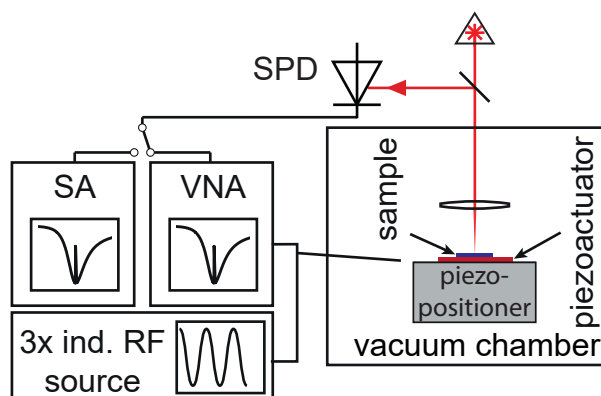


Figure 2.10: Sketch of the frequency measurement setup. The optically read out signal is converted and analyzed using either a vector network analyzer (VNA) or a spectrum analyzer (SA). Three individual frequency sources are used to in-situ tune the mode frequencies of the measured resonators.

2.4.3 Time domain setup

To investigate the dynamics of the nano-string network, we employ a time domain (TD) measurement setup. This setup is schematically shown in Fig. 2.11. Here, we still use the three RF sources for in-situ tuning however, we use an arbitrary wave generator (AWG), capable of emitting complex auxiliary drive sequences and a pulsed RF source to send excitation pulses to the system. A digitizer card with up to 200×10^6 samples/s is used to acquire the photo-detector's voltage signal. In these measurements, the AWG is used to instigate both, the excitation pulse sent to the sample, and the start of the data acquisition by the digitizer card. Thereby, we are able to measure the mechanical excitation of a selected single string in the network over time. By changing the read out string, we can probe the dynamics of the whole network part by part.

2.5 Measurement results

Here, we will present, discuss, and interpret measurement data collected from the resonator network. First, we will show and discuss characterization measurements of the system in the frequency domain, extracting the single string parameters as well as the inter-string coupling strengths in the network respectively. Here, the differences between the two sample layouts will be pointed out. In the following section, we will explore the case, in which all three resonators are tuned into resonance with each other and discuss the emergence of a mechanical dark state. In the last section, we will consider time domain measurements to explore the dynamics of the population transfer in the *star shaped* system. There, we treat two main cases, one covered by analytic solutions of the Landau-Zener three-level model 2.2.1, and one beyond its scope.

2.5.1 Characterization measurements

In this first section, we discuss the basic characterization measurements of the *star shaped* system. This is necessary to extract the system parameters. These parameters are used

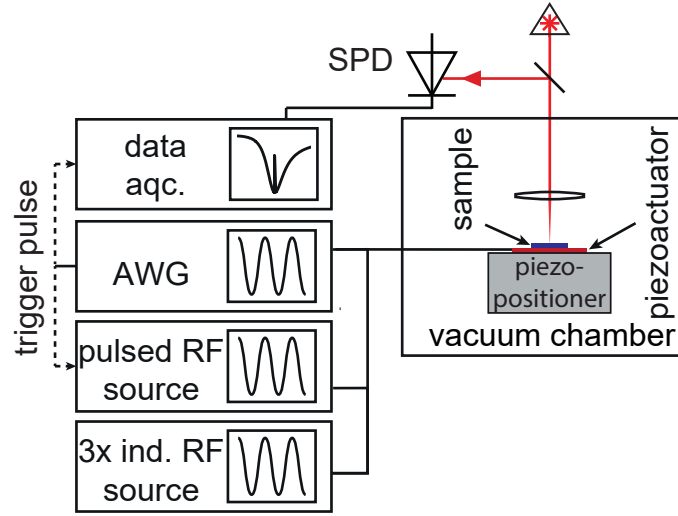


Figure 2.11: Full data acquisition setup used for the time domain measurements investigating the dynamics of resonator networks. Three individual frequency (RF) sources are used to in-situ tune the network at any time. A fourth source, paired with an arbitrary waveform generator (AWG) can be used to send shaped pulses to the piezo actuator and thus the sample. The photo detector voltage is processed using a digitizer card with up to $200 \cdot 10^6$ samples/s.

later as inputs for the numerical simulations, which we will use to corroborate the experiments addressing the dynamic response of the system. For the basic characterization of the system, we focus primarily on the spectroscopy of the modes, their controllability and their interactions. First pairwise, then all together. Figure 2.12 a) shows the displacement response of nano-string A in the star shaped layout, using a controlled stimulus and vector network analysis. We observe the dominant response of the mode α , which is originally spatially situated on the optically probed nano-string A. In addition to the mode of the probed string, we detect signatures of the β and γ mode, which are initially spatially associated with nano-strings B and C respectively. Their signatures are visible in the spectrum of string A due to the finite intermodal coupling. This happens even, if the mode frequencies are not on resonance with each other. Figure 2.12 a) shows the situation of the large natural detuning ($\Delta_{ij} \gg g_{ij}$), and thus allows to determine the resonance frequencies of the nano-strings A, B and C ($\Omega_{A,B,C}^0/2\pi$ cf. 2.1) with one measurement. Please note, that these frequencies, as well as their respective linewidths, may differ from their intrinsic values. This is due to the finite coupling between the strings and the disparity between the probed string A and the rest of the network (B & C). Although the strings were designed to be identical (cf. 2.3.2), the extracted resonance frequencies differ by several kHz. We note, that according to Eq. (1.19) and assuming a constant mass density ρ within the Si_3N_4 , the difference in frequency corresponds to a difference in length of about 60 nm. Effects of irregularities in the strings crosssection are neglected here, which is reasonable given the large aspect ratio of the strings and the fabrication process. Complementary thermal displacement noise measurements of all three resonators are used to extract the intrinsic resonance frequencies as well as linewidths of approx. 80(10) Hz. This corresponds to a Q-factor of about 150.000. Explicitly Fig. 2.13 shows the thermal displacement measurement for string B. Fitting this data with a Lorentzian lineshape (Eq. 1.19) allows us to

determine the intrinsic frequency $\Omega_B/2\pi = 9.2463$ MHz as well as its intrinsic linewidth to $\Gamma_B/2\pi = 86(1)$ Hz. Following this procedure for all strings in the network, we summarize

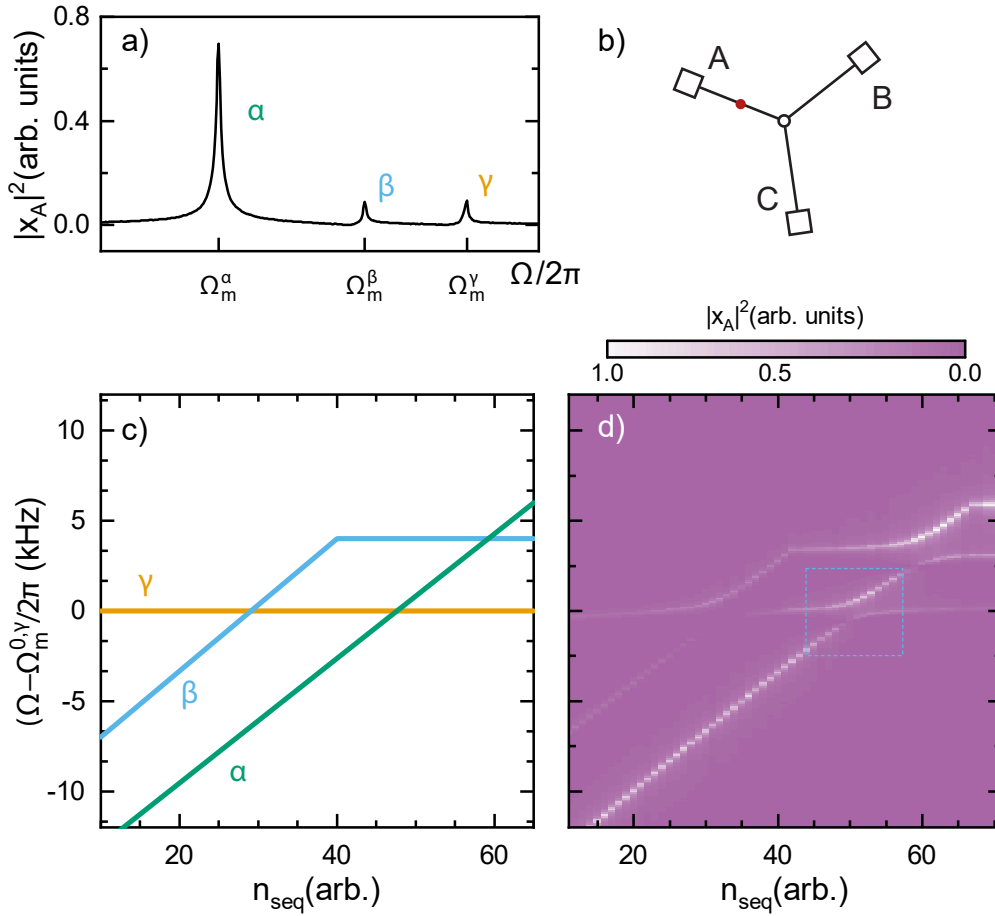


Figure 2.12: a) Mode distribution in the uncoupled case, read out via resonator A. The frequencies of modes α , β and γ are distinguishable. b) Schema of the used sample layout, the red dot indicates the laser spot position in the network. c) Tuning sequence showcasing the in-situ control over the system. d) Normalized mechanical response of the string network during the frequency tuning sequence shown in panel c). The presented data is read out via nano-string A. At points of frequency matching between two modes, avoided crossings are visible, e.g. crossing between β and γ indicated by blue rectangle.

the intrinsic resonance frequencies and linewidths in Table 2.1. Next, we turn to determine the intermodal coupling strengths. For this, we control the resonance frequencies using the frequency tuning scheme based on the geometric nonlinearity (see Sec. 1.3.3). For this experiment we use three RF sources, providing the drive signals to excite the higher order modes of the respective strings. In detail, we tune the frequencies of the three modes according to the configuration sequence shown in Fig. 2.12 b). The frequency tuning scheme is designed to realize a scenario where only individual modes dominantly intersect, and hence we can apply the ICA (cf. 2.2.1). In this situation, we can directly determine the individual inter-modal couplings g_{ij} (cf. Sec. 2.2.2). Note, that Fig. 2.12 c) and d) label the configured situation of the frequency by the index n_{seq} , as several frequencies are tuned at

	A	B	C
$\Omega^0/2\pi$	9.2382 MHz	9.2463 MHz	9.2538 MHz
$\Gamma/2\pi$	80(10) Hz	80(10) Hz	80(10) Hz

Table 2.1: Eigenfrequencies of the undisturbed modes of the string resonators (A/B/C) and their linewidth (FWHM), for the *star shaped* sample layout.

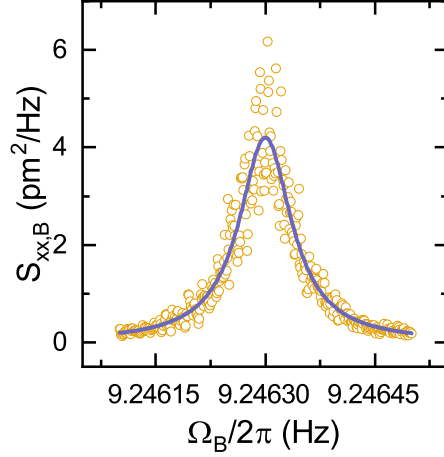


Figure 2.13: Thermal noise spectrum of a single nano-string (B) in the network. By fitting a Lorentzian line-shape (Eq. 1.19) to the data, we can extract the intrinsic resonance frequency Ω_B^0 and FWHM Γ_B . The values for all three strings are given in Tab. 2.1.

the same time. Hence, for the range shown, we use $n_{seq} \leq 10$ to configure the three modes α, β and γ with approximately equidistant resonance frequencies. Fig. 2.12 d) shows the driven mechanical response acquired by optically selecting nano-string A and conducting a VNA measurement. Hereby, we observe all modes in the network, even at large detuning between the modes. The intermodal coupling strengths can be directly extracted from the evolution of mode dispersion during the sequence: For example, at $n_{seq} = 47$, where mode α is nominally resonant with mode γ , we find the signature of an avoided crossing, while mode β is still far detuned. Equivalent scenarios are found at $n_{seq} = 28$ and at $n_{seq} = 59$, where avoided crossings are visible between α and γ , as well as α and β respectively. However, the coupling rates extracted using the driven approach have to be taken with care, as we use a relatively strong excitation force. As stated, this has the benefit, that we can follow all of the modes within one spectrum, even if they are far detuned. But, we cannot exclude that we drive the mechanical response into the non-linear regime. Hence, we employ thermal displacement noise spectroscopy to quantify the coupling rates. Fig. 2.14 shows the marked inset in Fig. 2.12 c), where we determine the coupling rate as $g_{\alpha\gamma}/2\pi = 1307$ Hz. In this particular case, we tuned the modes α and γ into resonance with each other, such that they hybridize. Here, we can identify the dressed state frequencies $\Omega_+^{\alpha,\gamma}$ and $\Omega_-^{\alpha,\gamma}$ as the respective upper and lower branches of the crossing (cf. 2.2.1). The mode β is detuned from these degenerate modes by 15 kHz and therefore does not impact the measurement, and the ICA can be applied. At the point of optimal mode mixing, we can extract the mode spacing as $2g_{\alpha\gamma}/2\pi = 1307$ Hz (cf. Eq. (2.8)). The panels b)

and c) of Fig. 2.14 show the extracted resonance frequencies and effective linewidths, extracted by fitting the single slices of a). We compare this to the mode frequency splitting between α and γ in Fig. 2.12 c). There $(\Omega_+^{\alpha\gamma}(n_{seq} = 47) - \Omega_-^{\alpha\gamma}(n_{seq} = 47))/2\pi = 1050$ Hz indicates a coupling strength of $2\tilde{g}_{\alpha\gamma}/2\pi = 1050$ Hz. This shows a significant difference between the two measurement techniques. Comparing the extracted coupling with the effective linewidth in the measurement shown in Fig. 2.14 $\Gamma_{\alpha,\gamma} \approx 80$ Hz we find, that the system is well in the strong coupling regime ($g_{\alpha\gamma} \gg \Gamma_{\alpha,\gamma}$). Similarly, all individual inter-modal couplings were determined and are summarized in Tab. 2.2. Using the approach

	$\alpha\beta$	$\beta\gamma$	$\alpha\gamma$
$g_{ij}/2\pi$	640.5 Hz	615 Hz	653.5 Hz

Table 2.2: Inter mode coupling strengths for the full symmetric, star shaped, three resonator network, extracted from individual avoided crossing measurements.

employing displacement noise spectroscopy, we determine all the parameters to quantify the Hamiltonian describing the system

$$H^{(3)} = \hbar \begin{pmatrix} \Omega_\alpha(t) & g_{\alpha\beta} & g_{\alpha\gamma} \\ g_{\alpha\beta} & \Omega_\beta(t) & g_{\beta\gamma} \\ g_{\alpha\gamma} & g_{\beta\gamma} & \Omega_\gamma(t) \end{pmatrix}.$$

For comparison, we show an equivalent measurement for the in-line layout in Fig. 2.15. Here, the modes are δ , ε and ϕ which in the far detuned case can be associated with the resonators D, E and F. The tuning sequence for the measurement is shown in panel a). The VNA measurement is done by reading out the central string E and subsequently tuning first modes δ and ϕ to the same frequency ($n_{seq} = 12$) then modes δ and ε at $n_{seq} = 35$ and finally the modes ε and ϕ ($n_{seq} = 57$). The first mode intersection, between the modes of the two end strings (D and F) shows no noticeable coupling effects whatsoever. This can be seen in Fig. 2.15 d), where the resonance frequencies for the region within the dashed orange rectangle in Fig. 2.15 b) are shown. Here, a clear crossing of the two modes is visible, indicating no noticeable coupling. When looking at the other two intersections, clear avoided crossings are visible. This is exemplary shown in Fig. 2.15 c). Here, the crossing of δ and ε in the region indicated by the red rectangle in Fig. 2.15 b) is evaluated. From the data we extract a mode frequency splitting of $2g_{\delta\varepsilon}/2\pi = 260$ Hz. For this case the three-level Hamiltonian (2.5) can be written as:

$$H^{(3)} = \hbar \begin{pmatrix} \Omega_\delta(t) & g_{\delta\varepsilon} & 0 \\ g_{\delta\varepsilon} & \Omega_\varepsilon(t) & g_{\varepsilon\phi} \\ 0 & g_{\varepsilon\phi} & \Omega_\phi(t) \end{pmatrix}.$$

The full parameter set for the in-line layout is summarized in App. B.2.

2.5.1.1 Emergence of mechanical dark modes

Now, that the characterization of the single resonators, as well as the characterization of individual mode pairs is concluded, one interesting situation accessible within the frequency regime is still missing. This is, where all three modes are tuned to the same frequency and thus are degenerate with each other. This case is of particular interest in the star shaped

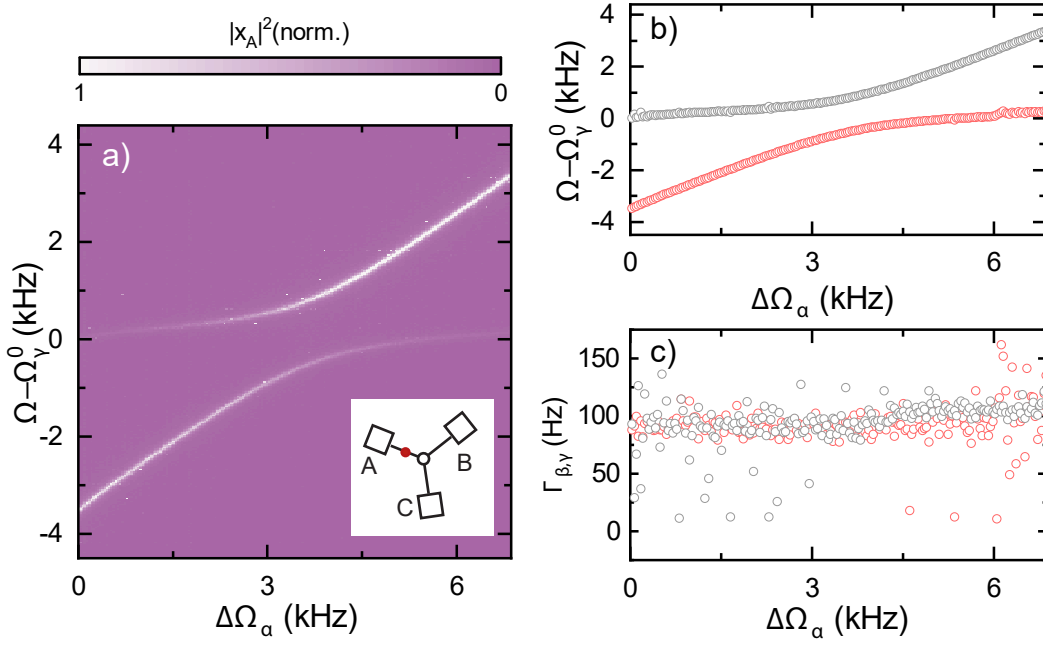


Figure 2.14: a) Measurement of the avoided crossing between the resonantly coupled modes β and γ , read out via resonator B. b) Extracted resonance frequencies from the measurement shown in a) at the point of optimal mode mixing, the coupling strength between the modes $g_{\beta,\gamma}/2\pi = 1230$ Hz can be extracted. c) Extracted linewidth (FWHM) of both modes during the avoided crossing, the linewidth is not influenced by the tuning mechanism, however the mode residing on the read out resonator shows a slightly higher quality factor.

layout, therefore we will focus on this case. At this point of mode degeneracy, the network can fully interact. This is of uttermost interest, since it represents an exemption of the analytically solvable range of the three-level Landau-Zener model (2.5). Figure 2.16 a) shows the corresponding thermal displacement spectrum for this case, where $\Omega_\alpha \approx \Omega_\beta \approx \Omega_\gamma$. We realize the fully degenerate state by only tuning one mode during the experimental data shown. For $\Delta\Omega_\alpha = 0$, the resonance frequencies are set to configure the modes β and γ in a hybridized state with the mixed frequencies $\Omega_+^{\beta\gamma}$ and $\Omega_-^{\beta\gamma}$ as defined in Eq. (2.8). We then increase the frequency of mode α through $\Omega_+^{\beta\gamma}$ and $\Omega_-^{\beta\gamma}$ and investigate the characteristic spectrum by optically probing the displacement of nano-string B. At $\Delta\Omega_\alpha = 0$, the assumptions of the ICA remain valid and an analytical description of the spectrum is still possible. We can describe the hybridized modes $\Omega_+^{\beta\gamma}$ and $\Omega_-^{\beta\gamma}$ using the coupled mode picture (2.2). However, this changes as soon as mode α starts to interact with the hybridized modes ($\Omega_\alpha + \Delta\Omega_\alpha \lesssim \Omega_-^{\beta\gamma}$). This becomes apparent from the formation of an avoided crossing between Ω_α and the lower branch of the hybridized modes $\Omega_-^{\beta\gamma}$ and the shift of the uppermost branch $\Omega_+^{\beta\gamma}$ to higher frequencies. Notably, the mode spacing between Ω_α and $\Omega_-^{\beta\gamma}$ shows a reduced effective mode splitting of $2g_{\text{eff}}/2\pi = 497(1)$ Hz at $\Delta\Omega_\alpha = 1.8$ kHz compared to the undisturbed mode splitting $2g_{\alpha\beta}/2\pi = 1281$ Hz (cf. 2.2). At a detuning of $\Delta\Omega_\alpha/2\pi = [2.5 \text{ kHz} - 3.5 \text{ kHz}]$, another interesting feature of the

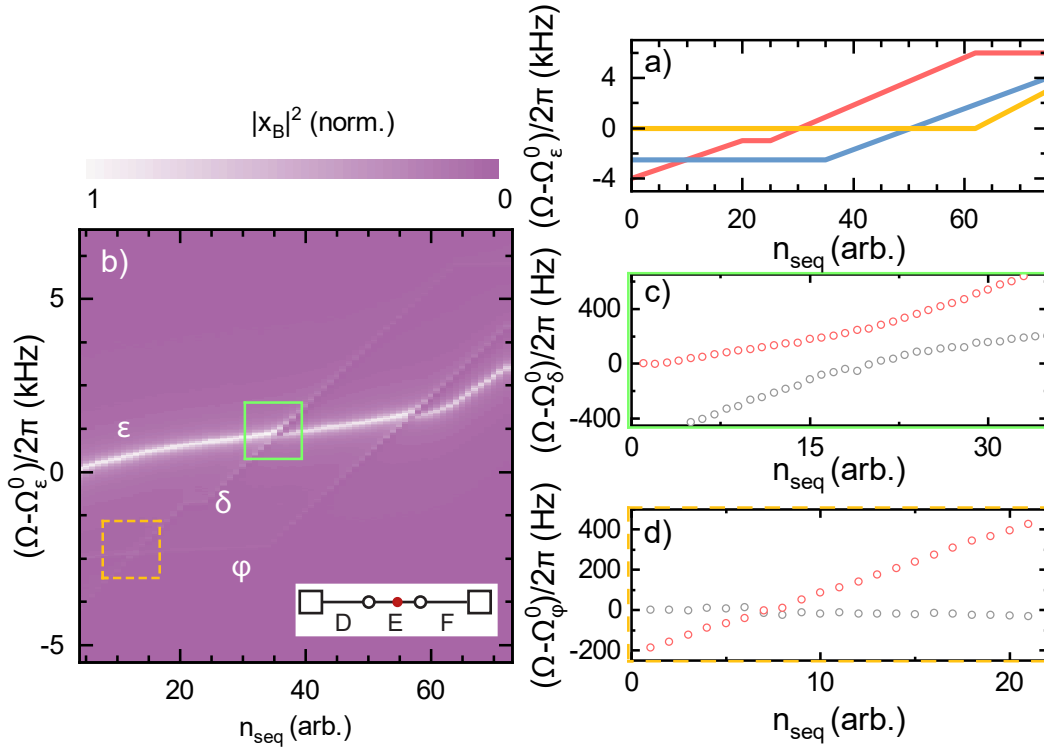


Figure 2.15: Normalized mechanical response of the in-line layout sample. In a) the tuning sequence for the measurement is depicted. b) shows a VNA measurement of string E during a tuning scheme (cf. inset) bringing all three resonators into resonance with each other sequentially. Avoided crossings are visible for the coupled strings (D/E and E/F) whereas a simple crossing can be seen for the uncoupled strings (D/F). The modes associated with the respective strings (D/E/F) are labeled as $\delta/\varepsilon/\phi$. c) Extracted frequencies for the avoided crossing indicated by the red rectangle in b) allowing the determination of the inter string coupling strength $g_{\delta\varepsilon}/2\pi = 260$ Hz. d) Extracted frequencies of the crossing of the outer strings D and F, indicated by the dashed orange rectangle in b) showing that there is no discernible coupling between them.

system emerges. We find a suppression of the thermal displacement of one of the modes, i.e. a dark state. Here, the uncoupled frequencies of mode α , β , and γ become degenerate and the central of the three hybridized modes quenches. Fig. 2.16 b) shows the extracted resonance frequencies, over the course of the experimental data. The extracted amplitude is encoded in the area of the data points. The values were extracted by fitting three individual Lorentzian lineshapes to the spectra in panel a). Note, that for the region, where the middle mode quenches, no resonance frequency could be extracted, since there are no discernible features or peaks visible in the background noise of the data. While, as stated before, analytic models cannot grasp the full richness of the spectrum, numerical simulations can be used to predict the frequency and amplitude evolution as shown in Fig. 2.16 c). Here, we show a full numeric simulation of the experimental data shown in a) by solving Eqs. (2.32) to (2.34) as shown in Sec. 2.2.2.1.1. We do this using the parameters determined beforehand for the coupling strengths and frequencies. Please note, that the model uses no free fit parameters, however it contains a linear correction term to

take heating effects on the sample into account (cf. 1.3.3). The calculated displacement amplitude is encoded in the area of the plot symbols of Fig. 2.16 c). In the region of the dark mode, no amplitude is present for the calculated frequencies, therefore we add a small bias to all amplitude values to visualize the frequency of the dark mode. This allows to better discern the frequency of the dark mode. As one can clearly see, the numerical simulations match the experimental data to a high degree regarding the mode frequencies. However, they cannot reproduce the amplitude, especially for the top branch of the measurement. This is mainly due to the fact, that the numerical solution does not take the transduction over the read out resonator into account, which influences the data extracted in the experiment.

The emergence of dark states has been extensively studied in optomechanics in recent years [146–148]. There the effect that those modes cannot absorb or emit excitations has been used to facilitate mediated quasi loss-less energy transfer between e.g. an optical as well as a microwave mode coupled to a mechanical dark mode [147]. Even more recently, mechanical dark-modes were observed in a strongly coupled three-mode Λ -type system [149]. Here, we observe a dark state in a, to our understanding, more general three-level system. All inter-modal coupling rates are present, comparable, and the system is well in the strong coupling regime. This is even true when taking the effective coupling strength into account ($g_{eff} > \Gamma$).

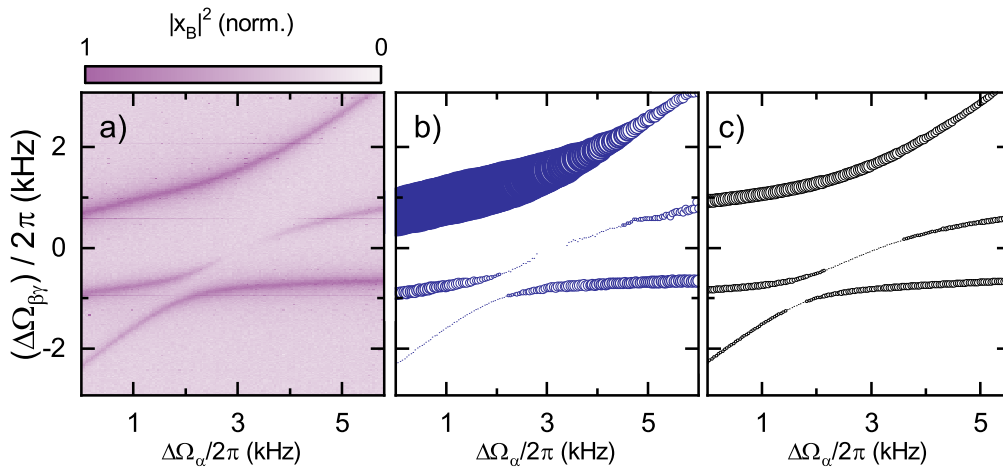


Figure 2.16: a) Tuning sequence which tunes all three modes in resonance with each other. The lower mode of the coupled system ($(\beta, \gamma)^-$) goes dark for a specific de-tuning combination. This would allow addressing only specific modes of a otherwise resonantly coupled system. b) Resonance frequencies for the single modes, extracted from a) using Lorentzian fits on each slice. The extracted amplitude is encoded in the point area. c) Numerical simulation of the resonance frequencies shown in the measurement a). The area of the data-points shows the amplitude of the mode at a given point in the spectrum. A bias is added to the amplitudes in c), hereby we aim to visualize the frequency, as the calculated amplitude in the range of the dark-mode is otherwise indiscernible.

2.5.1.1.1 Finite element simulation To corroborate the measurement results regarding the dark mode, and gain insight into the mode shapes present in the sample designs presented in 2.3, we employ finite element simulations⁵ for this specific case. For this purpose, we used the design values for the resonator networks, as well as known material parameters (e.g. mass density and pre-stress). This results, naturally, in the same setup as was in-situ fine tuned in the measurement shown in Fig. 2.16 ($\Omega_A = \Omega_B = \Omega_C$). By setting the finite element simulation up this way, the inter-string coupling strengths are assumed to be equal $g_{AB} = g_{AC} = g_{BC}$, which is in good agreement with the actual sample parameters (cf. tab. 2.2). A visual representation of the simulated displacement field a is shown for a possible eigenfrequency solution in Fig. 2.17. The perfect rotational symmetry assumed in the simulation, exhibits three solutions for this fundamental mode, differing only in a 120° rotation in the xy -plane of the sample. In Fig. 2.17 suppression of the displacement amplitude of one string (in our case string B) compared to the remaining strings is visible in this frequency match setup. This effectively forms a dark-mode as was found experimentally.

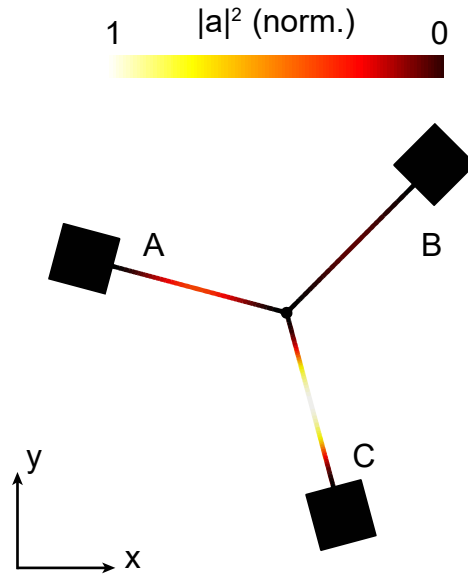


Figure 2.17: Results of a finite element simulation of the displacement field \vec{a} of the star shaped resonator network. Assuming identical nano-strings ($\Omega_\alpha = \Omega_\beta = \Omega_\gamma$), we observe a strongly suppressed displacement of nano-string B, corroborating the physical interpretation of a dark-state being possible in the network.

2.5.2 Excitation transfer dynamics

Next, we turn to investigate the dynamics of the star shaped multi-mode system using experiments inspired by Landau-Zener type state transfers [70, 71, 74, 134, 150]. For this, we first set the frequencies of the β and γ mode in a static fashion. The dynamics are then probed by tuning the α mode. Initially, we tune α to be off-resonant with the β

⁵Using *COMSOL Multiphysics*®.

and γ mode. At this point we prepare the amplitude state of the α mode with a sharp excitation pulse with a duration of $t_p = 400 \mu\text{s}$. After a short waiting period of $t_0 = 1 \text{ ms}$, the mode frequency of α is then chirped with the rate ζ through the frequency range. The frequency of mode α is at any point in time given by $\Omega_\alpha(t) = \Omega_\alpha^0 + \zeta t$. In the following, we will discuss how these dynamics are influenced by the initial setup for the modes β and γ where we will distinguish two principal cases, and how the chirp rate ζ allows switching between an adiabatic and a diabatic transition (cf. 2.2.1).

To quantify the dynamics of the excitation transfer, we record the response of the displacements of nano-string A, B, and C sequentially in the time-domain for various chirp-rates ($(\zeta/2\pi)^{-1} = 5 - 150 \mu\text{s/kHz}$). We distinguish between two principal system states for setting up modes β and γ . One (i) corresponds to the equal slope case discussed in 2.2.1.1, where all inter-mode coupling rates are present, but the frequencies of modes β and γ are never allowed to meet $\Delta_{\Omega_\gamma - \Omega_\beta} \gg g_{\beta\gamma}$, and are ordered $\Omega_\beta < \Omega_\gamma$, for the whole measurement. In this case, we can also treat all single avoided crossings with the ICA introduced in 2.2.1.1.1. In the second case (ii) we go beyond these analytically describable cases and initialize the modes β and γ in a hybridized state $\Omega_\beta, \Omega_\gamma \rightarrow \Omega_+, \Omega_-$ with a mode splitting of $(\Omega_+ - \Omega_-)/2\pi \approx 3 \text{ kHz}$. The dynamics for the in-line layout sample correspond to a high degree to the first case (i) with the difference of negligible inter-mode coupling between the modes of the outlying strings, δ and ϕ ($g_{\delta\phi} = 0$). The data for this setup can be found in App. B.2 for the interested reader.

Refocussing on the star-shaped layout, we will now first discuss the differences between the two cases and the impact of the chirp-rate ζ . Then we will take a closer look into the second case, since it holds richer features. In Fig. 2.18 the two cases are compared to each other, the columns show the different initial settings, the rows show experimental data, read out for each string respectively. The data is plotted over the inverse chirp rate. Thus, from fast chirp rates to slow chirp rates in each panel. The dashed lines are a guide to the eye, and give the times at which mode α is on resonance with the upper and lower modes respectively. The single columns are normalized to the initial excitation pulse respectively, allowing a quantitative comparison of the mechanical excitation on each string. In panels a) and d) we see the excitation on string A, here we can also see the damping of the system, as the decay of excitation is visible, especially for slow chirp rates. For small times t , the excitation remains on the string A, where it has been initially prepared, and experiences the expected exponential relaxation. Consequently, we observe no visible initial excitations on strings B and C. Note, that the dependence of the adiabaticity of the crossing is dependent on the chirp rate, as can be seen in all panels. The fastest chirp rates ($(\zeta/2\pi)^{-1} \leq 7 \mu\text{s/kHz}$), represent the diabatic limit of the system. The excitation fully remains on nano-string A (or mode α), where it decays, even after passing through the other modes, regardless of which case. In contrast, slow chirp rates ($(\zeta/2\pi)^{-1} \geq 7 \mu\text{s/kHz}$) result in a partially adiabatic transfer to the other modes, where a significant difference between the two cases emerges. Case (i) results in the two expected sequential Landau-Zener type state transfers, depending on the chirp rate and thus the adiabaticity of the process. Here, excitation is first transferred to one mode (panel b)), and then, independently to the second mode (panel c)). The main difference being the initial excitation present on string A before the avoided crossing with the respective modes. This leads to different excitation amplitudes on string B and C. However, as panels b,c) show, the crossing with the respectively other mode has no impact on the mechanical amplitude of the measured

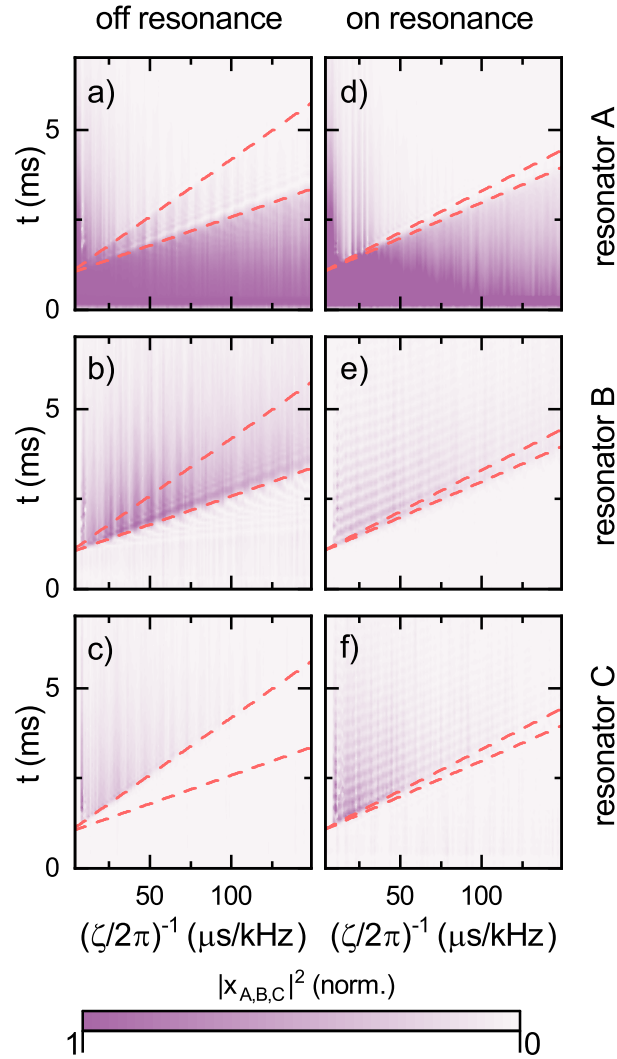


Figure 2.18: Excitation of the single strings over the time of a Landau-Zener experiment. The string network is in the off-resonant configuration ($\Omega_\beta \neq \Omega_\gamma$) for panels (a-c), and in the resonant configuration ($\Omega_\beta \approx \Omega_\gamma$) for panels (d-f). In both cases an initial pulse is used to excite mode α . The resonance frequency of mode α is then chirped, upwards through the resonance frequencies of the other modes with varying chirp rates (fast to slow). The dashed lines are a guide to the eye to mark the times at which the mode frequency of α matches the mode frequencies of β (lower) and γ (upper) respectively. The measurements are shown for all read-out resonators (A,B,C) respectively. A high mechanical response of the measured string is depicted by dark color. Each column of the graph is normalized to the initial excitation pulse.

string. In case (ii), where all resonators can become resonant simultaneously, the situation is more involved. The experimental data of these scenarios shows already more structure in Figure 2.18, where a fast beating in panels e) and f) is visible. To further analyze this, Fig. 2.19a-c) shows the same data, constricted to a smaller range of times and ζ showing

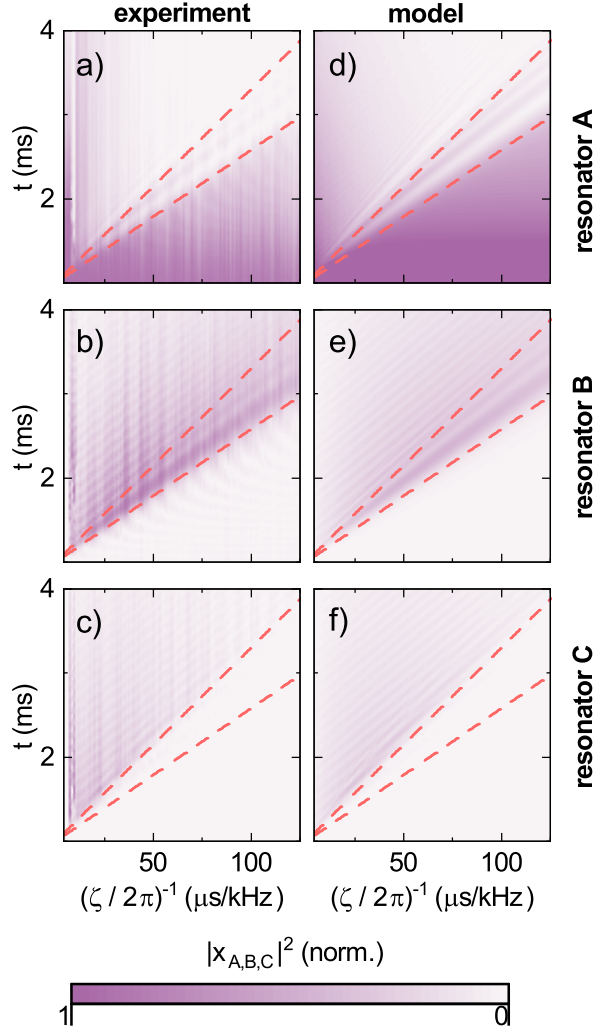


Figure 2.19: Excitation of the single strings over the time of a Landau-Zener experiment. Measurement data of the string network in the resonant configuration $\Omega_\beta \approx \Omega_\gamma$ (a-c), and corresponding numerical simulation results (d-f). In both cases an initial pulse is used to excite mode α . The resonance frequency of α is then chirped, upwards through the resonance frequencies of the other modes with varying chirp rates (fast to slow). The dashed red lines are a guide to the eye to mark the times at which the mode frequency of α matches the mode frequencies of $\beta\gamma_-$ (lower) and $\beta\gamma_+$ (upper) respectively. The measurement and model are shown for all read-out resonators (A,B,C) respectively. A high mechanical response of the measured string is depicted by dark color. Each column of the graph is normalized to the initial excitation pulse.

greater detail. Panels d-f) of Fig. 2.19 show the full numeric simulation for comparison to the data in a-c). Here, already for times between the passage of α through the small range between $\Omega_-^{\beta\gamma}$ and $\Omega_+^{\beta\gamma}$, we observe a slow beating in the excitation of nanostring A and B (see panels a/d and b/e). We associate this temporal evolution with the complex

interplay of the various coupling rates (cf. Fig. 2.16). There, we found a reduced effective mode splitting between mode α and $\Omega_{-}^{\beta\gamma}$ of $2g_{\text{eff}}/2\pi \approx 500$ Hz. If we compare this to the frequency of the slow beating $f \approx 350(150)$ Hz we find them to be in the same order of magnitude and thus a general agreement. However, the measured data does not allow a deeper analysis, since the beating frequency only shows one clear maximum and a second very unclear one. If we compare this to the off-resonant case 2.18 a/b) we do not find any structure in the excitation there. For times after the transit of both, the $\Omega_{-}^{\beta\gamma}$ and $\Omega_{+}^{\beta\gamma}$ mode, we find that, depending on ζ most of the excitation in resonator A is absent, similar to case (i). However, we record a fast beating of the excitation between resonators B and C. The latter can be understood as the pure modes of resonator B and C being hybridized and hence the excitation starts to oscillate between the physical nano-strings. This underlines the hybrid character of the modes, being distributed over parts of the network. We determine this oscillation frequency in Fig. 2.20. Here we show an exemplary cut from panels b-e) and c-f) in Fig. 2.19 at a chirp rate of $(\zeta/2\pi)^{-1} = 25$ $\mu\text{s}/\text{kHz}$. The extracted mechanical excitation for both resonators, experimental data as well as numerical simulation, is shown in the first column of Fig. 2.20. Here we see the sharp rise in excitation as the mode is coupled to mode α , modulated onto the exponential decay however, is the fast beating mentioned before. To analyze this beating, we Fourier transform the left column of Fig. 2.20 and show the results in the right column. The fast beating is now extracted by fitting a Lorentzian line shape to the first and only peak at non-zero frequency. This allows us to extract the beating frequency as $\Omega_{\text{R}}/2\pi \approx 3270(320)$ Hz which corresponds to the mode frequency splitting between the modes $\Omega_{-}^{\beta\gamma}$ and $\Omega_{+}^{\beta\gamma}$ set in the experiment. This supports that this feature is indeed a classical pendant to a Rabi oscillation [71]. This further indicates, that we are clearly beyond all analytic solutions for the three-level Landau-Zener model.

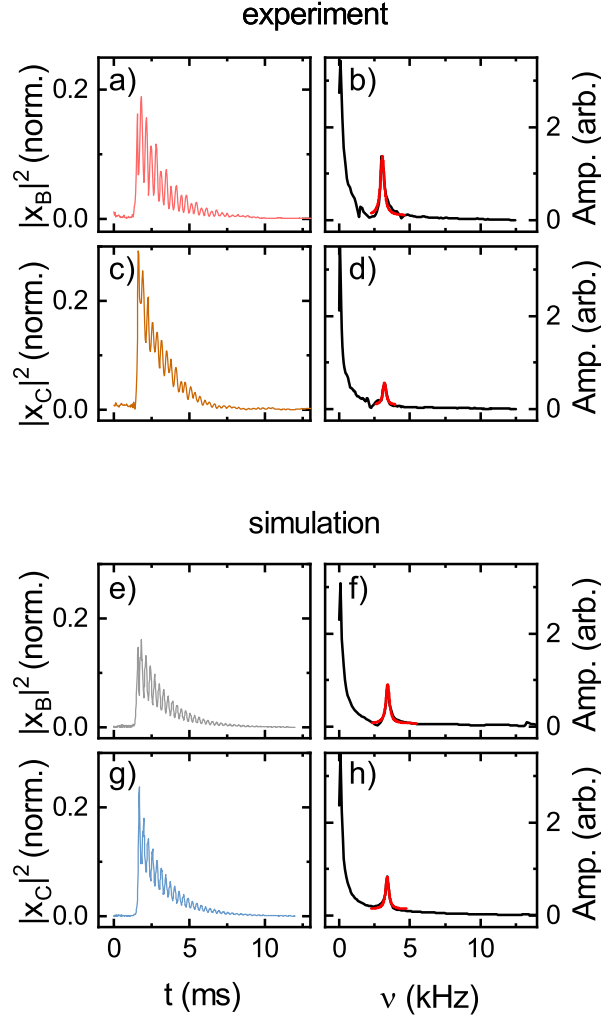


Figure 2.20: Method used to extract the beating frequency in Fig.2.19b-f). Single slices at $(\zeta/2\pi)^{-1} = 25 \mu\text{s}/\text{kHz}$ are shown for both resonators (B/C) from the experimental data as well as numerical simulation in the left column (a,c,e,g). The right column (b,d,f,h) shows the Fourier transformation of the neighboring data, the red line is a Lorentzian fit to the data, to extract the fast beating frequencies.

2.6 Discussion and Outlook

We experimentally investigated and characterized a nano-string network comprised of three nano-mechanical string resonators with independently tunable resonance frequencies, and comparable strong inter-resonator coupling. For this, we designed the device structure and adapted previously established fabrication processes to reliably fabricate the designed structures from thin Si_3N_4 films on Si substrate. Using an optical interferometry setup, combined with a frequency domain measurement setup, we characterized the individual nano-strings and the inter-string coupling strengths. For the specific setting, where all strings are resonant, we explored the emergence of a dark state in the system. We corroborate the emergence of this dark state using numerical calculations as this model goes beyond an analytic description. The relevance of dark states can be seen in the context

of information storage [151–153]. Other uses are for example in the field of topological energy transfer [154–156]. Using the same optical interferometer, but employing time domain measurement techniques, we investigated the dynamical evolution of the three nano-string network. Here, we explored the feature of having all mechanical elements interact with each other, as well as use the possibility of in-situ controlling all frequencies at the same time. In this context, we investigated the excitation transfer inspired by Landau-Zener physics. We did this in the range still describable by analytic solutions and beyond it. This demonstrates control over the transfer dynamics in a nano-string resonator network. We show, that these networks can still be expanded and are not yet at their limit. As the three nano-string network represents a building block for phononic networks, we expect our finding to be relevant for the controlled phonon or excitation propagation in mechanical networks. With the current setup of highly symmetric strings, frequency crowding in the auxiliary drive tones becomes an issue with the rising number of strings. Here two, independent paths promise solutions to this issue: By carefully designing the geometry of the single strings, they can be engineered to support different modes, which can then be addressed without interference. Alternatively, clever network design could be done, to limit the number of strings, which need to be controlled at the same time, even if the used network is much larger. In this regard, also multiplexing of auxiliary drives within a network may be a possibility. A more prominent issue is presented by the heating effects on the sample, due to the high power auxiliary drives. This was not optimized or even technically addressed here. For rising numbers of auxiliary drives, either the temperature impact of the piezo, or a temperature control of the sample must be engineered in the mid to long term. To look even further ahead, this work represents a classical simulation of equations of motions and we are confident that this system, or systems like this have the potential to be employed as classical simulators of quantum state transfer processes.

PART 3

MAGNETOSTRICTIVE INTERACTION IN NANOMECHANICAL RESONATORS

3.1 Introduction

Mechanical systems are used as sensing devices throughout daily life, most of them in the form of **Micro Electro Mechanical Systems** (MEMS) [10, 16, 17, 157, 158]. However, the next generation of sensing devices in the form of **Nano Electro Mechanical Systems** (NEMS) is in development [44, 45, 159–161]. Nanomechanical string resonators are an interesting platform for sensing applications, due to their typically very high quality factors. This combined with precise readout methods, allows determining minuscule changes in the nano-string’s environment or its own material properties and geometric parameters [162–164]. Thus, by coupling a nano-string to an external degree of freedom or making the string itself dependent on external parameters, it is possible to investigate them. Due to the physical size of a nano-string, it provides the possibility to measure small sample sizes and enables integrability with most semiconductor materials, devices and fabrication techniques.

Here, we want to learn about the magnetoelastic properties of the ultra-low magnetic damping material $\text{Co}_{25}\text{Fe}_{75}$, and how these can influence other sample parameters. Specifically, we want to investigate the interaction between the internal strain of a multilayer nano-string and the strain in the single constituent layers. The strain of the string material is, as mentioned already in part 1, one of the main contributors to the resonance frequency of a nano-string. Thus, a change in the strain can be detected easily and precisely, as we can detect the resonance frequency of strings with high Q -factors fast and precise using e.g. laser interferometry (cf. part 2). Magnetic alloys are an extremely well studied material group due to their importance for applications in magnetic information storage. While properties such as the saturation magnetization and magnetic anisotropy play key roles for the static configuration and stability of the magnetization state, material parameters related to magnetization control (beyond such enacted by static magnetic fields) are also

of huge interest.

Apart from current-induced magnetization switching [165–169], techniques based on magnetostriction constitute a complementary way to control the magnetization direction. Here, the elastic deformation of the material generates a strain-induced anisotropy term, which can be used to reorient the magnetization. Static control [77, 170–172] as well as the excitation of magnetization dynamics [173–176] already have been demonstrated. The reciprocal effect is used in sensing applications based on magnetoelastics [177]. The nano-string platform allows extracting the magnetostrictive properties of the material under the challenging circumstances. In this case due to the fact, that the material of interest is a thin-film layer in an elaborate layer stack. The advantage of the NEMS based approach is, that it enables to investigate complex materials on the nano-scale, e.g. in the field of thin films which is the realistic configuration for later device concepts, compared to previous studies [178–190], which focused on bulk samples. In particular, cobalt iron alloys recently regained interest as an electrically conducting ferromagnetic material, with ultra-low magnetic damping [108, 191, 192]. We note, that these damping properties are intimately linked with the layer stack in which the compound is embedded. Here, damping in thin film $\text{Co}_{25}\text{Fe}_{75}$ was found to be as low as in thin film yttrium iron garnet [193]. Since applications in spin electronics are usually based on thin films, quantification of the magnetoelastic properties of thin film $\text{Co}_{25}\text{Fe}_{75}$ is in this context of high interest. The investigated films were grown using the same recipe as the ultra-low damping material of Ref. 108, by the group of Justin Shaw at NIST¹. The findings shown here, were partially published in the article entitled *Magnetoelasticity of $\text{Co}_{25}\text{Fe}_{75}$ thin films* by D. Schwienbacher et al. and appeared in Journal of Applied Physics [80]

In the first Chapter 3.2, we discuss how the strain in the material is changed by magnetostrictive effects, and how this influences the resonance frequency of a nano-string depending on the material and magnetization. Next, we turn to the sample layout, composition and fabrication, followed by the introduction of the experimental setup. In Sec. 3.5, the acquired data is presented, analyzed and brought in context with the magnetostrictive response of the material. We then summarize this part and give a brief outlook. One of the main questions is, if the magnetoelastic properties are connected to the magnetization properties of the material, as in the case of the well known material system Permalloy (NiFe) [194].

3.2 Theoretical background

In this chapter, we introduce the model used to describe the magneto-mechanical interaction in a multi-layer nano-string, where at least one of the constituent layers is magnetic. For this we consider the magnetization of the magnetically active layer, which will later be controlled by an external magnetic field, and how this changes the strain/stress exerted by this layer onto the overall string. This will allow connecting the magnetostriction and magnetization of the material to the resonance frequency of the nano-string.

Magnetostriction and magnetoelasticity link the mechanical properties of a solid with the magnetic texture. These effects are part of the so-called multiferroic triangle [77] depicted in Fig. 3.1. Direct interactions are used to control e.g. the magnetization, the electric

¹NIST, Colorado Boulder, USA

polarization and the strain of a body using magnetic fields, electric fields, and stress. However, also indirect interactions occur, where one for them is magnetostriction. This effect was first identified by James Joule in 1842 [195,196], and connects the magnetization of a material to changes in the strain. The inverse effect, which describes the change in the magnetization of a material when exposed to stress or mechanical deformation is known as magnetoelasticity [197]. We will discuss the impact of these effects onto the system of

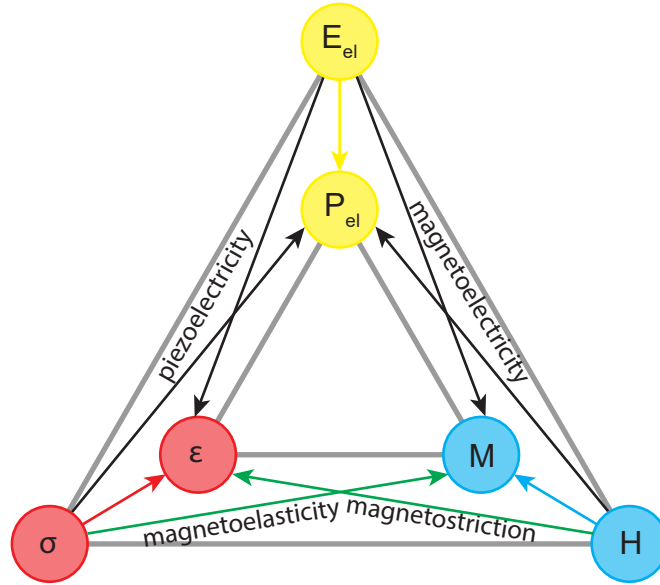


Figure 3.1: Phase control in (ferroic) magnetic materials. The magnetic field H , electric field E_{el} and stress σ can control the magnetization M , polarization P_{el} and strain ϵ in the sample respectively. The magnetoelastic interaction connects the magnetic field H with the strain in the sample ϵ and vice versa the stress σ with the magnetization M . Picture adapted from Ref. [77].

a (partially) magnetic nano-string in the following. For this, we will first consider magnetostriction in a magnetic thin film. Next we will discuss the changes in the behaviour if the thin film is constrained in its geometry and lastly the impact it has as a part of a multi-layer nano-string.

3.2.1 Magnetostriction in a free FM thin film

To discuss the impact of magnetostriction onto the resonance frequency of a nano-string, we need to consider how the magnetostriction comes to bear in a magnetic thin film. We start with a free standing thin film, only constricted in its thickness t which points along the z -direction and assume it to be infinite in the xy -plane for this step. For simplicity, we further assume that this thin film is in a monodomain state. Magnetostriction, which couples the magnetization to the lattice degree of freedom, will then lead to a mechanical deformation [197], depending on the magnetostriction vector \vec{M}/M_S and the saturation magnetization of the material M_S . The same effect will further lead to an inverse deformation along both orthogonal directions in the film, conserving its volume. In addition, the mechanical properties of the solid also play a role, and for simple scenarios this relative deformation, given by the elastic response, can be expressed in terms of the poisson ratio. A sketch

showing this effect can be seen in Fig. 3.2, where the initial film shape is contracted after fully magnetizing it. The contraction/elongation $\epsilon_{\parallel}(\epsilon_{\perp})$ for the directions along (perpendicular) to the magnetization orientation is given by the magnetostrictive constants λ_{\parallel} and λ_{\perp} respectively [197]:

$$\begin{aligned}\epsilon_{\parallel} &= \frac{\Delta L}{L} = \lambda_{\parallel} \\ \epsilon_{\perp} &= \frac{\Delta W}{W} = \lambda_{\perp}.\end{aligned}\tag{3.1}$$

Please note, that due to volume conservation the two magnetostriction constants need to be of opposite sign ($\lambda_{\parallel} < 0 < \lambda_{\perp} \vee \lambda_{\perp} < 0 < \lambda_{\parallel}$). We now want to consider the strain tensor, associated with the relative elongation and contraction. We define the $x'-y'-z'$ system as shown in Fig. 3.2 to be the natural system for the magnetostriction, where the magnetization direction defines the x' -axis. At this point, we also define the angle between the magnetization direction and the sample coordinate system as Θ , whereas Φ is the angle between the x -axis and the external magnetic field direction. The latter is used to control the direction of the magnetization. In the framework of the $x'-y'-z'$ coordinates, the magnetostrictive strain tensor is given by:

$$\epsilon'_{\text{mag}} = \begin{pmatrix} \lambda_{\parallel} & 0 & 0 \\ 0 & \lambda_{\perp} & 0 \\ 0 & 0 & \lambda_{\perp} \end{pmatrix}.\tag{3.2}$$

For our experiments however, we naturally use a coordinate system which reflects the reality of the lab. To combine both, we need to use the appropriate rotation tensor \mathbf{R} , which connects the $x-y-z$ coordinates and the $x'-y'-z'$ coordinates:

$$\mathbf{R} = \begin{pmatrix} \cos(\Theta) & -\sin(\Theta) & 0 \\ \sin(\Theta) & \cos(\Theta) & 0 \\ 0 & 0 & 1 \end{pmatrix}.$$

Thereby, we obtain the magnetostrictive strain tensor in the $x-y-z$ lab coordinate system as:

$$\epsilon_{\text{mag}} = \mathbf{R}^T \epsilon'_{\text{mag}} \mathbf{R} = \begin{pmatrix} \lambda_{\parallel} \cos^2(\Theta) + \lambda_{\perp} \sin^2(\Theta) & (\lambda_{\perp} - \lambda_{\parallel}) \cos(\Theta) \sin(\Theta) & 0 \\ (\lambda_{\perp} - \lambda_{\parallel}) \cos(\Theta) \sin(\Theta) & \lambda_{\perp} \cos^2(\Theta) + \lambda_{\parallel} \sin^2(\Theta) & 0 \\ 0 & 0 & \lambda_{\perp} \end{pmatrix}.\tag{3.3}$$

Note that this expression contains the magnetization direction Θ . However, we experimentally control the external magnetic field direction, characterized by the angle Φ in Fig. 3.2. If the external magnetic field \mathbf{H} is sufficiently large, that it suppresses all anisotropies in the system, the magnetization direction directly coincides with the magnetic field direction ($\Theta = \Phi$). If the external magnetic field is not large enough to overcome all anisotropies, the relation gets more involved. Therefore, we need to consider the impact of an anisotropy in the system onto the relation between Θ and Φ . We will now make this consideration for an uni-axial anisotropy along the x -axis. This corresponds e.g. to a shape anisotropy, if the magnetic material is constrained in a rectangular shape with a high aspect ratio, as it will be as a part of a nano-string. This anisotropy leads to a magnetic hard axis as well as a perpendicular magnetic soft axis in the material. Magnetizing the material along the soft axis is easier than magnetizing it along the hard axis, thus the magnetization

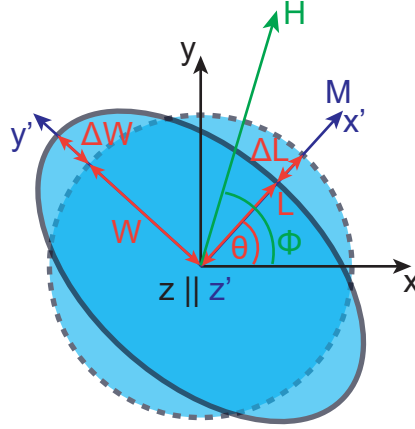


Figure 3.2: Coordinate system of the metallic magnetic film. The sample and lab coordinate system is spanned by x - y - z the natural system of the magnetostriction spanned by x' - y' - z' points its x' -direction along the magnetization direction \mathbf{M} . The rotation between the two coordinate systems is defined by Θ . The external magnetic field, points along the angle Φ in the x - y -plane. The dashed circle represents the film's equilibrium shape without any magnetization. The external magnetic field H magnetizes the film and it deforms (solid shape) along the magnetization direction.

direction will follow the external magnetic field direction directly along certain directions, whereas it will deviate along the perpendicular direction. We calculate the exact relation between the magnetization direction Θ and the magnetic field direction Φ for an uniaxial anisotropy along x with anisotropy constant K_{au} [113] by minimizing the free magnetic energy in the system [197]. This results in a $\Theta(\Phi)$ given by:

$$\Theta(\Phi) = \Phi - \frac{K_{\text{au}} \sin(2\Phi)}{-M_S \mu_0 H + 2K_{\text{au}} \cos(2\Phi)}. \quad (3.4)$$

3.2.2 Magnetostriction in a thin film on a substrate

In order to compare the experimental data with the magnetostrictive calculation of the stress in the string, we also need to consider the boundary conditions imposed by the geometry. In particular, the case where the film has been deposited on top of a substrate is of interest. The shared interface with a substrate layer imposes geometric boundary conditions on the magnetic material in the xy -plane. In an intuitive picture, the magnetostriction changes the equilibrium dimensions of the string, depending on the magnetization direction. For a material with e.g. $\lambda_{\parallel} < 0$ the equilibrium length of the string is reduced, whereas its width is increased. However, the boundary conditions ensure a constant length of the string, which results in a tensile stress in the magnetic layer along the strings x -direction, and respectively a compressive stress along the y -direction. Since the boundaries are only in the xy -plane, the film is free to expand or contract in the z -direction. We can mathematically describe these effects by introducing an additional strain ϵ_r countering the

magnetostrictive strain ϵ_{mag} in such a way, that the effective strain along the x and y -axis vanishes. We define

$$\epsilon_{\text{net}} = \epsilon_{\text{mag}} + \epsilon_{\text{r}},$$

with

$$\epsilon_{\text{net},x} = \epsilon_{\text{net},y} = 0.$$

This additional strain ϵ_{r} , can be seen as applied by the boundary conditions. It leads to an additional stress in the string, depending on the magnetostriction in the magnetic film:

$$\sigma_{\text{mag}} = \mathbf{C}\epsilon_{\text{r}}. \quad (3.5)$$

Here, \mathbf{C} denotes the elasticity tensor [113]. The strain thus can be written using the Voigt notation [113] as:

$$-\epsilon_{\text{r}} = \begin{pmatrix} \epsilon_{\text{r},xx} \\ \epsilon_{\text{r},yy} \\ \epsilon_{\text{r},zz} \\ 2\epsilon_{\text{r},yz} \\ 2\epsilon_{\text{r},xz} \\ 2\epsilon_{\text{r},xy} \end{pmatrix} = \begin{pmatrix} \lambda_{\parallel} \cos^2(\Theta) + \lambda_{\perp} \sin^2(\Theta) \\ \lambda_{\perp} \cos^2(\Theta) + \lambda_{\parallel} \sin^2(\Theta) \\ \epsilon_{\text{r},zz} \\ 0 \\ 0 \\ 2(\lambda_{\perp} - \lambda_{\parallel}) \cos(\Theta) \sin(\Theta) \end{pmatrix}. \quad (3.6)$$

Please note, that we are still assuming that the magnetic film is in a monodomain state. Furthermore we assume the magnetic film to be polycrystalline. The elasticity tensor \mathbf{C} for a polycrystalline material, is given by [113]:

$$\mathbf{C} = \begin{pmatrix} \lambda + 2\mu & \lambda & \lambda & 0 & 0 & 0 \\ \lambda & \lambda + 2\mu & \lambda & 0 & 0 & 0 \\ \lambda & \lambda & \lambda + 2\mu & 0 & 0 & 0 \\ 0 & 0 & 0 & \mu & 0 & 0 \\ 0 & 0 & 0 & 0 & \mu & 0 \\ 0 & 0 & 0 & 0 & 0 & \mu \end{pmatrix}, \quad (3.7)$$

with the material's shear modulus μ , Lamé constant $\lambda = (2\mu^2 - E\mu)/(E - 3\mu)$ and the Young's modulus E [113]. Now, we can define the free expansion of the material in z -direction, for which we use the fact that $\lambda_{\parallel} = -\nu\lambda_{\perp}$ with the Poisson ratio ν , as well as $\mu = E/2(1 + \nu)$ [113] to write:

$$\epsilon_{\text{r},zz} = \lambda_{\parallel} \left(1 - \frac{E}{2\mu}\right). \quad (3.8)$$

Here, we neglected the volume magnetostriction in the first order [197]. By combining Eqs. (3.5)-(3.8) we obtain for the magnetostrictive induced stress σ_{mag} ²:

$$\sigma_{\text{mag}} = \begin{pmatrix} \sigma_{\text{mag},xx} \\ \sigma_{\text{mag},yy} \\ \sigma_{\text{mag},zz} \end{pmatrix} = - \begin{pmatrix} E\lambda_{\parallel} \cos^2(\Theta) \\ E\lambda_{\parallel} \sin^2(\Theta) \\ 0 \end{pmatrix}. \quad (3.9)$$

²Please note, that we use „magnetetoelastically induced stress“ and „magnetically induced stress“ equivalently from here on.

3.2.3 Magnetostriction in a multi layer string

As stated in the introduction, we want to use a sensing concept employing the measurement of the mechanical resonance frequency, to investigate different materials with specific material properties. For this, we deposit the materials on top of a Si_3N_4 nano-string. Therefore, we now need to discuss the impact of a magnetostrictive layer in a multi-layer metal, Si_3N_4 nano-string. For this, we need to take into account both the intrinsic tensile stress in the Si_3N_4 (σ_{SiN}), as well as the stress in the magnetic thin film ($\sigma_{\text{film}}^{\text{tot}}$). For a double-layer system of a thin metal film on top of a Si_3N_4 string, the effective stress along the string direction is given by [198, 199]

$$\sigma_{\text{eff}} = \frac{\sigma_{\text{SiN}}t_{\text{SiN}} + \sigma_{\text{film,x}}^{\text{tot}}t_{\text{film}}}{t_{\text{SiN}} + t_{\text{film}}}, \quad (3.10)$$

as discussed in Sec. 1.2.1. Notably, the total stress in the magnetic layer contains contributions from both intrinsic pre-stress in the material as well as the magnetostrictive stress discussed in the last section $\sigma_{\text{film}}^{\text{tot}} = \sigma_{\text{film}}^0 + \sigma_{\text{mag}}$. If we now use this effective stress and introduce it into the expression for the resonance frequency of a tensile stressed string (1.28), we obtain:

$$\Omega_{\text{TS}} = \frac{\sigma_{\text{eff}}\pi\sqrt{A/\rho_{\text{eff}}}}{\sqrt{\sigma_{\text{eff}}Al - 2\sqrt{E_{\text{eff}}I}}}. \quad (3.11)$$

Here, l denotes the string's length, A its crosssection, I its moment of inertia along the oscillation direction and ρ_{eff} the effective mass density. E_{eff} denotes the effective Young's modulus of the whole string as defined in Eq. (1.31). Since the effective stress partially depends on external parameters, namely the magnetization direction, it is convenient to split the total stress into a static and an angle dependent part:

$$\begin{aligned} \sigma_{\text{eff}} &= \sigma_0 + \sigma_1 \cos^2(\Theta) \\ \sigma_0 &= \frac{\sigma_{\text{SiN}}t_{\text{SiN}} + \sigma_{\text{film}}^0t_{\text{film}}}{t_{\text{SiN}} + t_{\text{film}}} \\ \sigma_1 &= \frac{Et_{\text{film}}\lambda_{\parallel}}{t_{\text{SiN}} + t_{\text{film}}} \end{aligned} \quad (3.12)$$

This allows us to rewrite (3.11) into

$$\Omega_{\text{mag}} = \frac{n(\sigma_0 + \sigma_1 \cos(\Theta)^2)\pi\sqrt{\rho_{\text{eff}}^{-1}}}{\sqrt{(\sigma_0 + \sigma_1 \cos(\Theta)^2)L - 2\sqrt{E_{\text{eff}}t^2/12}}}. \quad (3.13)$$

This equation describes the resonance frequency of a double-layer nano-string consisting of a Si_3N_4 string with a thickness t_{SiN} and a magnetic layer with t_{film} on top, as a function of the magnetization orientation in the thin film material. Please note, that we assume that the magnetization is predominantly the xy -plane of the magnetic material and the magnetic material is in a monodomain state. Eq. (3.13) will be used later, to extract the values for the magnetostrictive constant λ_{\parallel} from measurements of the resonance frequency by varying the magnetization direction.³ In this context we will also encounter the magnetoelastic constant b [173, 197] which is correlated with the magnetostrictive constant via

$$b = \frac{B}{M_s} = -\frac{3\lambda_{\parallel}\mu}{M_s}. \quad (3.14)$$

³Please note, that we will use the descriptions „magnetization direction dependence“ and „angular dependence“ equivalently during this part 3 of the thesis.

3.3 Device design and fabrication

As the fabrication of double clamped Si_3N_4 nano-strings is already discussed in Sec. 2.3.1, here, we present only a brief description of the additional fabrication processes needed to add a CoFe stack to the top of the string. The project involving these CoFe samples was performed in collaboration with the National Institute for Standards and Technologies (NIST) in Boulder, Colorado, USA.

For the fabrication of $\text{Co}_x\text{Fe}_{1-x}$ layers on top of the freely suspended silicon nitride string resonators, we start with a single crystalline silicon wafer, which is commercially coated with a $t_{\text{SiN}} = 90$ nm thick, highly tensile-stressed (LPCVD) grown Si_3N_4 film. We define

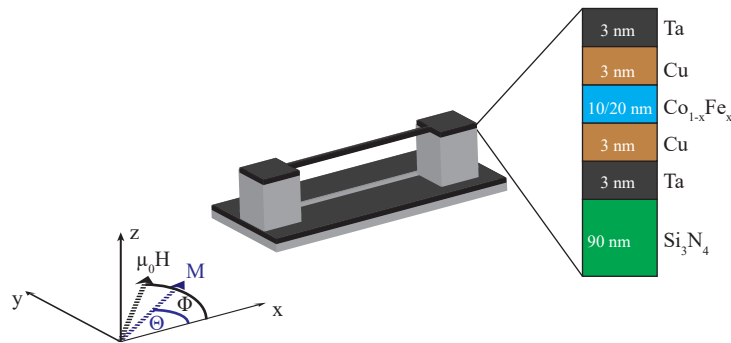


Figure 3.3: Schematic of the multi-layer nano-string. The Si_3N_4 string is topped with a complex layerstack necessary for the high quality CoFe sandwiched in the center.

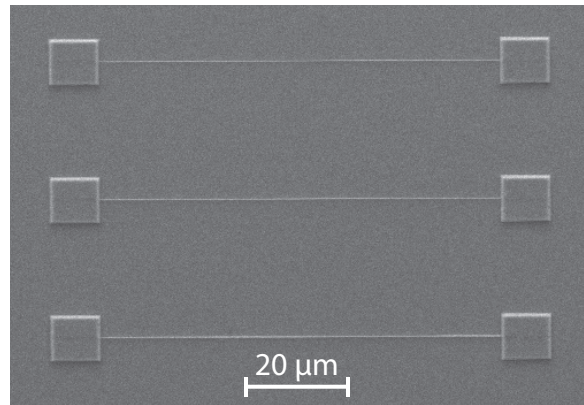


Figure 3.4: SEM picture showing an array of typically used Si_3N_4 strings before depositing metal layers on top. The strings are 80 μm long and from top to bottom 300 nm, 200 nm and 150 nm wide.

the geometry of the strings by defining a metal etch mask using electron beam lithography, electron beam evaporation of aluminium, and a lift-off process, same as already discussed in Sec. 2.3.1. A SEM picture of a part of a typical nano-string array can be seen in Fig. 3.4. The resulting unloaded SiN strings show typical Q -factors of about 150 000 for the ip and oop fundamental modes (cf.1.3). As the last fabrication step, the metal layer

on top was sputtered. For the CoFe samples a Ta/Cu/CoFe/Cu/Ta layer stack (as shown in Fig. 3.3) was deposited on top of the strings by magnetron sputtering⁴. This layer stack is composed from a seed layer of 3 nm of Tantalum, followed by a 3 nm thick layer of copper. Onto this the CoFe alloy was sputtered from a stoichiometric target. The CoFe alloy was then capped by two 3 nm thick layers of Copper and Tantalum. Thus, the CoFe stack covers the strings as well as the surrounding substrate. We ensured that there is no contact between the top- or string layer and the substrate level. With this process, two sets of samples with different CoFe alloys were fabricated: Co₂₅Fe₇₅, for which there was reported ultra-low magnetic damping properties [108] with a layer thickness of 10 nm, and Co₁₀Fe₉₀ as an alloy with larger damping for comparison with a layer thickness of 20 nm.

3.4 Measurement setup

To investigate Si₃N₄ nano-string covered with metal multilayers we employ an optical detection scheme, similar to the one used in part 2. More details about the initial configuration of the setup can be found in the Bachelor thesis of Peter Jörg [200]. During this thesis, this setup required multiple upgrades and adaptations.

3.4.1 Optical interferometer

The optical measurement technique uses a free space optical interferometer, in its basic concept very similar to the optical interferometer discussed in 2.4.1. However, this setup has no secondary interferometer arm and was build with a strong focus on the compatibility with electro-magnets. As can be seen in Fig. 3.5, the optical interferometer is split into two spatially separated parts, one operating in vacuum, to prevent the negative influence of air-damping on the nanostrings [115], and one situated in ambient environment. The vacuum vessel is shaped in a cylindric form to fit between the pole-shoes of several electromagnets at the WMI. Care was taken to use non-magnetic materials for this vacuum enclosure, as well as the components within. This suppresses motion or deflection of the interferometer parts due to magnetic fields. Here, we only present a simplified depiction of the interferometer. A full description can be found in App. C.3. The beam of a 633 nm laser is fed into the interferometer by a single mode fiber from a spatially separated source. Besides removing the necessity of mounting a relatively bulky and heavy laser directly on the head of the setup, it allows a flexible switching of laser sources. The beam then passes the optical head unit and is guided into the vacuum tube and focused onto the sample. The reflected laser light is modulated by the string on the sample in the same way as in Sec. 2.4.1. The reflected light re-enters the head unit and is guided to the photo detector. A LED source as well as a camera in the head unit allow optical access to the sample. The chip containing the nano-string is mounted on a *xyz*-piezo stage to allow precise positioning of the selected nano-string in the focal point of the laser. The laser beam is focused on center of the string ($x = l/2$) and interferometry is used to measure the displacement of the nano-string's oop motion. To excite this oop mode at its resonance frequency, the entire sample is glued on an extended piezo-actuator using a novolak polymer (Fig. 3.6, red layer). This actuator allows to exert a coherent oscillating force onto the entire chip,

⁴The samples were fabricated in cooperation with the group of Justin M. Shaw, special thanks go to Eric R.J. Edwards, who fabricated the CoFe stacks.

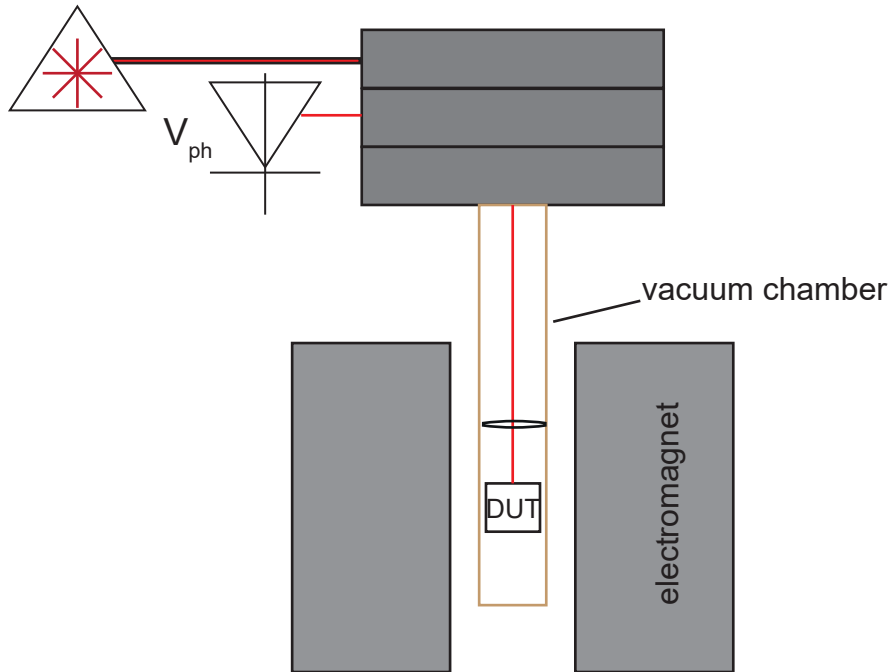


Figure 3.5: Sketch of the optical interferometer. The laser beam from a spatially separated laser is guided to the interferometer head by a single mode fiber. The head unit guides the laser into the vacuum tube. The reflected light is again passed through the head unit onto a photo-detector. A red LED source and a camera for optical access to the sample are integrated into the interferometer head. A full schematic can be found in App. C.3. The interference occurs similar to the interferometer in Sec. 2.4.1 between the light reflected by the nano-string and the light reflected by the substrate beneath the string.

which is glued on-top and hence allows to excite the motion of the nano-string. Technically, we detect the frequency dependent displacement response of the nano-string to such a stimulus using a vector network analyzer (VNA). To remain in the linear response regime of the nano-string, we choose an appropriately small excitation amplitude (cf. 1.3.2). To control the direction of magnetization, the sample is positioned between the pole pieces of an electromagnet. In detail, this allows to control the amplitude and direction of the applied magnetic field, rotatable in the xy -plane. The applied field direction is varied by rotating the electromagnet, whereas the sample position and orientation remain fixed.

3.5 Magnetostriction of ultra-low damping CoFe films

In this section, we discuss experiments investigating the magnetostriction of ultra-low damping CoFe thin films. This work was carried out in collaboration with the group of Justin M. Shaw at the NIST, Boulder. The main part of the data shown here were published in Ref. [80].

Figure 3.7 a) shows a color-encoded plot of the driven mechanical response function as a function of actuation frequency and applied magnetic field direction. Red highlights large out-of-plane(oop) mechanical displacement, while blue indicates no visible motion.

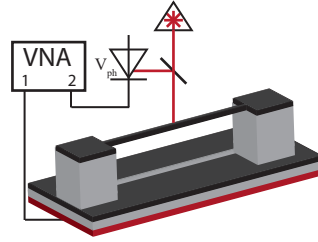


Figure 3.6: Schema of the measurement setup for the optical interferometry. A laser beam ($\lambda = 633 \text{ nm}$) is focused onto the center of a nano-string, the reflected light intensity is detected with a photo-diode. The sample is glued onto a piezo-actuator (red layer), which is used to globally drive the nano-strings on the sample. A vector network analyzer (VNA) is used to send the driving tone to the piezo and compare relate this to the signal detected by the photo-diode. The sample stage is positioned between the pole-shoes of an electromagnet, this allows the application of an external magnetic field.

This raw data is measured for a constant actuation amplitude and a fixed magnitude of the magnetic field $\mu_0 H = 950 \text{ mT}$. The resonance frequency of the string is 180° periodic with respect to the external magnetic field direction. An exemplary cut of this dataset at $\Phi = 153^\circ$ is displayed in the inset of Fig. 3.7 b), showing the mechanical response as function of the drive frequency. As the sample position is not actively stabilized, we attribute variations in the detected amplitude to drifts in the optical alignment originating from the rotation of the magnetic field direction. We estimate typical displacement amplitudes present in our experiment to be in the nanometer range⁵. To extract the resonance frequency, we fit a Lorentzian line shape (1.41) to the data for each measured angle Φ . From this fit we find a linewidth (full-width at half-maximum) of 900 Hz corresponding to a Q -factor of the string of about 8000. This Q -factor is significantly reduced compared to that of a pure SiN string and can mainly be attributed to the added metal layer stack. The stack increases the overall mass of the string, and thereby its effective density, which lowers the resonance frequency (see Eq. (3.13)). Moreover, adding a metal component is known to change the mechanical damping of nano-strings [198, 201]. Figure 3.7b) shows the evolution of the resonance frequency as a function of Φ .

To investigate the impact of the shape of the nano-string on the frequency response, we have measured a set of strings with different lengths and widths. To analyze our data, we use a global fit routine employing Eqs. (3.4) and (3.13). The fit uses the data of all strings for each CoFe ($\text{Co}_{25}\text{Fe}_{75}$ / $\text{Co}_{10}\text{Fe}_{90}$) composition as input parameter. In addition, we use the thickness $t = 112 \text{ nm}$ and 122 nm of the nano-strings and their effective densities $\rho_{\text{eff}} = 4350 \text{ kg/m}^3$ and 4336 kg/m^3 of each string as fixed parameters, as both are known

⁵An active calibration of the mechanical amplitude was not possible with this sample. The mechanical amplitude was estimated using geometrically similar samples made from pre-stressed SiN and pre-stressed Al.

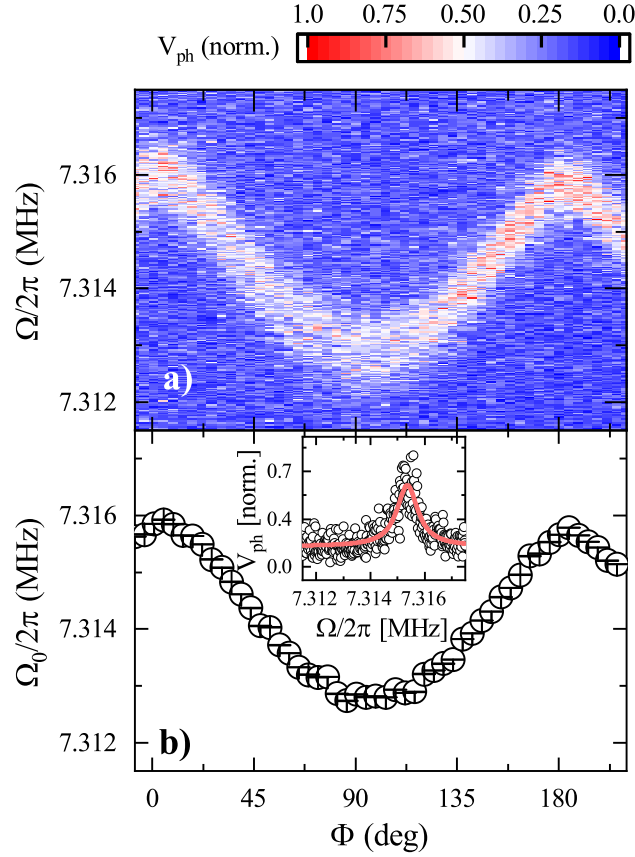


Figure 3.7: Mechanical response of the fundamental mode of a $25\ \mu\text{m}$ long nano-string as a function of external field direction Φ at $\mu_0 H = 950\ \text{mT}$. a) Shows the frequency dependent photo-voltage as a function of external magnetic field direction and drive frequency. This is a direct measure for the mechanical amplitude of the string. b) Shows the extracted resonance frequencies at specific field directions. The inset in b) shows a slice from a) at $\Phi = 153^\circ$ and the fit to a Lorentzian line shape (red line) used to extract the resonance frequency. Error bars are fit errors.

values. The thickness of the metal stack was determined by calibrating the deposition rates using x-ray reflectometry. The density was calculated by using the weighted average of the single material bulk densities [202]. Figure 3.8 a) shows the fit of Ω_0 for the $\text{Co}_{25}\text{Fe}_{75}$ compound for strings of different lengths. Here, the pre-stress σ_0 , the magnetically induced stress σ_1 , and the Young's modulus E of the sample were set as global fit parameters. For the fit, we used fixed values for the length l of the strings with $25\ \mu\text{m}$ and $35\ \mu\text{m}$. The string lengths of the two nominally $50\ \mu\text{m}$ long strings are free fit parameters. This allows to account for small variations in the frequencies of the two nominally identical strings, which otherwise should have the exactly the same frequency. The fitted lengths are $51.2\ \mu\text{m}$ and $50.8\ \mu\text{m}$ and are in good agreement with the design value of $50\ \mu\text{m}$. The uniaxial anisotropy constant K_{au} is a free fit parameter for each string as it might differ from string to string. Figure 3.9 a) shows the same for three nano-strings topped with the $\text{Co}_{10}\text{Fe}_{90}$ alloy, although in this case all three lengths ($25\ \mu\text{m}$, $35\ \mu\text{m}$ and $50\ \mu\text{m}$) were fixed parameters. As shown in Fig. 3.8 a) and Fig. 3.9 a), we find good agreement between the global fit and the data using $\sigma_1 = -386(5)\ \text{kPa}$, $\sigma_0 = 458.7(1)\ \text{MPa}$ and $E = 857.7(2)\ \text{GPa}$

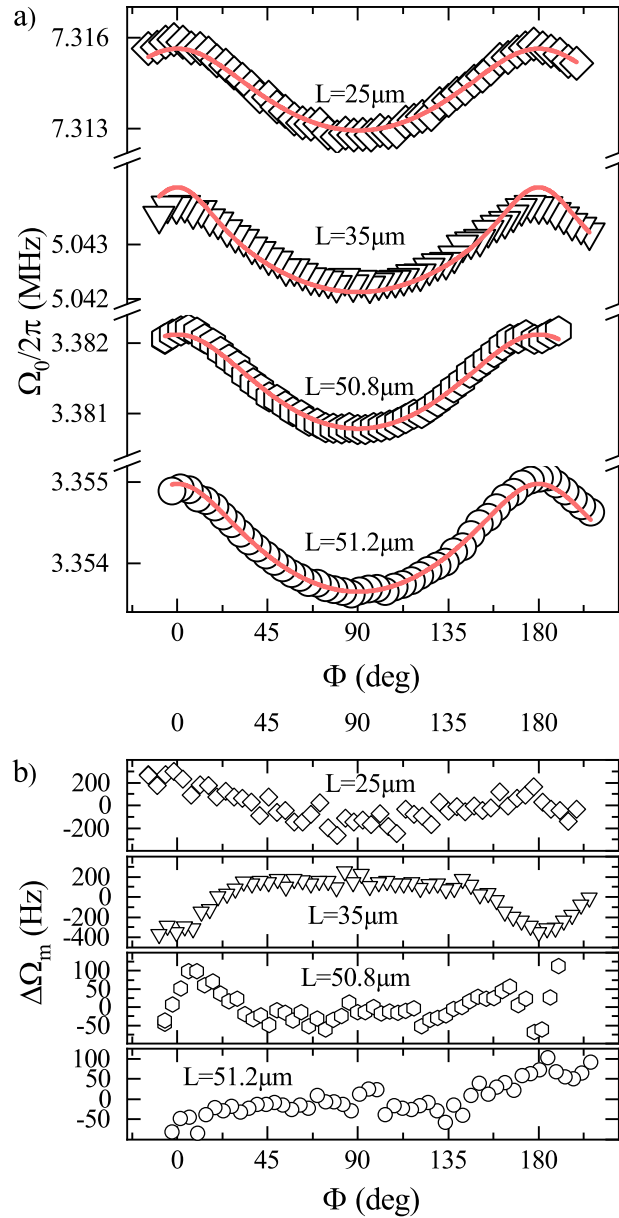


Figure 3.8: Global fit to the magnetization direction dependent resonance frequencies of strings with different lengths covered with the $\text{Co}_{25}\text{Fe}_{75}$ stack. The resonance frequencies of the strings with a length of $25\mu\text{m}$ (diamonds), $35\mu\text{m}$ (triangles), $50.8\mu\text{m}$ (hexagons) and $51.2\mu\text{m}$ (circles) length were globally fit using Eqs. (3.4) and (3.13) (red lines). Fit errors are within the size of the data symbols. In b) the deviation $\Delta\Omega_m = \Omega_0 - \Omega_{\text{fit}}$ is plotted versus Φ . The residuals are non zero for all the strings, however no clear systematics are apparent.

for the $\text{Co}_{25}\text{Fe}_{75}$ alloy and $\sigma_1 = -334(5)$ kPa, $\sigma_0 = 175.0(1)$ MPa and $E = 247.5(2)$ GPa for the $\text{Co}_{10}\text{Fe}_{90}$ alloy. The difference in pre-stress and Young's modulus between the measurements can be attributed to the different alloys and their difference in layer thickness. The extracted pre-stress is reduced compared to the pre-stress in a SiN string without any metal on top. This can be attributed to a compressive stress in the layer stack, exemplary for the $\text{Co}_{25}\text{Fe}_{75}$ alloy of $\Delta\sigma_0 \approx 270$ MPa. The sputtering process may change the

pre-stress of the composite string. Even though the sputtering process is carried out at room temperature, the temperature of the nano-string is expected to increase significantly due to the poor thermal coupling of the string to the substrate. Thus, the metal stack is deposited at a temperature well above room temperature. Cooling down the string coated by the metal stack after deposition then results in a partial compensation of the pre-stress due to different thermal expansion coefficients of SiN and the metal stack. A temperature increase of about 300 K could explain the observed change of pre-stress. For the thicker $\text{Co}_{10}\text{Fe}_{90}$ alloy sample a higher compressive stress and thus a larger deviation in pre-stress can be assumed. Also, the extracted Young's modulus is larger than expected from the Young's moduli of the individual materials [202]. Using (3.12) and (3.14) in combination with the known sample parameters and the Co-Fe Young's modulus we obtain a $\lambda_{\parallel}(\text{Co}_{25}\text{Fe}_{75}) = (-20.68 \pm 0.25) \times 10^{-6}$ and $b(\text{Co}_{25}\text{Fe}_{75}) = 2.62(5)$ T. We obtain these values when considering $t_{\text{CoFe}} = 10$ nm, $t = 112$ nm, $E_{\text{CoFe}} = 208.9$ GPa [202], $M_{\text{S}} = 1.904$ MA m $^{-1}$ ([191]) as well as the shear modulus $G = 81.7$ GPa [202]. Here the Young's modulus and shear modulus for $\text{Co}_{25}\text{Fe}_{75}$ were calculated from the literature values of the single materials. The same was done in the case of $\text{Co}_{10}\text{Fe}_{90}$, here with a $t_{\text{CoFe}} = 20$ nm, $t = 122$ nm, $E_{\text{CoFe}} = 208.4$ GPa [202], $G = 81.6$ GPa [202] and $M_{\text{S}} = 1.825$ MA m $^{-1}$ [191]. Thus resulting in: $\lambda_{\parallel}(\text{Co}_{10}\text{Fe}_{90}) = (-9.80 \pm 0.12) \times 10^{-6}$ and $b(\text{Co}_{10}\text{Fe}_{90}) = 1.30(2)$ T.

In addition, the measured data allow to access magnetic anisotropy parameters. For the $\text{Co}_{25}\text{Fe}_{75}$ sample we find an anisotropy $2K_{\text{au}}/M_{\text{S}} \approx 300$ mT with an easy axis pointing along the y -direction of the string. Note that because we have access only to in-plane measurements, we can calculate only projections of an anisotropy to the xy -plane of the sample. Combined with the calculated shape anisotropy $B_{\text{shape}} \approx 100$ mT [113], with an easy axis along the x -direction of the string, the total anisotropy field in the sample adds up to $B_{\text{aniso}} \approx 400$ mT. The compressive stress in the metal $\Delta\sigma_0$ leads to a magnetoelastic anisotropy of $B_{\text{magnet}} \approx 4$ mT [197]. For the $\text{Co}_{10}\text{Fe}_{90}$ sample the anisotropies are similar. Unfortunately, we cannot identify the origin of the anisotropy. However, we speculate that the overhanging material at the edges of the string might result in a preferential orientation of the magnetization direction perpendicular to the string. This may be a result of moving (rotation) the sample during the sputtering process, which is however necessary to avoid other, even stronger stress induced anisotropies e.g. [203–205]. The deviation $\Delta\Omega_{\text{m}} = \Omega_0 - \Omega_{\text{fit}}$ shown in Fig. 3.8 b) shows that there is some disagreement between the model and the data, however, without any systematics. For the $\text{Co}_{25}\text{Fe}_{75}$ deviations are lower for the two strings where the string length is a fit parameter, compared to the other strings where the string length was fixed for the fit. In addition, we note that the assumption of a single uniaxial anisotropy in the system may lead to increased systematic uncertainties. The same general observation holds true for the $\text{Co}_{10}\text{Fe}_{90}$ sample, as can be seen in Fig. 3.9 b). To set these results in context, we plot the extracted values of λ_{\parallel} and b for the two measured thin film CoFe alloys ($\text{Co}_{25}\text{Fe}_{75}$ and $\text{Co}_{10}\text{Fe}_{90}$) as well as the values for thin-film Co [79] and bulk Fe [202] in Fig. 3.10. The ultra-low damping material investigated here seems to follow the simple trend of an interpolating magnetostrictive constant connecting the bulk values. Since the values for the saturation magnetization and shear modulus are similar for Co and Fe, b is approximately linearly proportional to λ . Nevertheless, Fig. 3.10 also shows the data from Hunter et al. [179] (star with dot) obtained using a cantilever displacement method on various 500 nm thick $\text{Co}_x\text{Fe}_{1-x}$ films. Their data

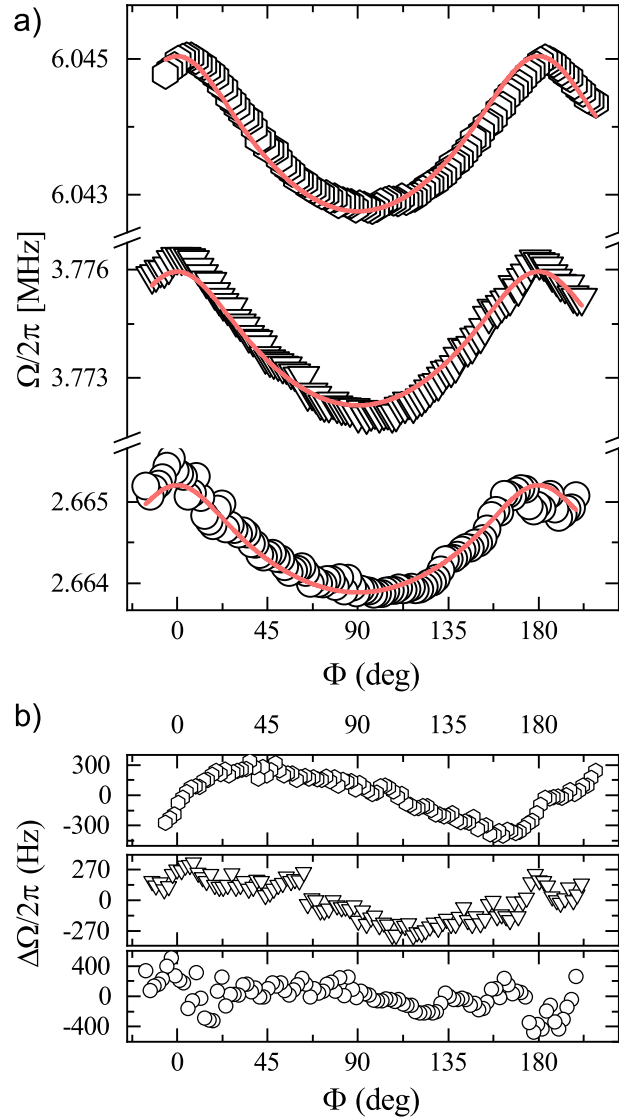


Figure 3.9: Global fit to the magnetization direction dependent resonance frequencies of strings with different lengths covered with the $\text{Co}_{10}\text{Fe}_{90}$ stack. The resonance frequencies of the strings with a length of $25\ \mu\text{m}$ (circles), $35\ \mu\text{m}$ (triangles) and $50\ \mu\text{m}$ (hexagons) length were globally fit using Eqs. (3.4) and (3.13) (red lines). Fit errors are within the size of the data symbols. In b) the deviation $\Delta\Omega_{\text{m}} = \Omega_0 - \Omega_{\text{fit}}$ is plotted versus Φ . The residuals are non zero for all the strings, however no clear systematics are apparent.

show an entirely different behavior, most importantly an opposing sign of $\lambda_{\text{S}} \approx 50 \times 10^{-6}$. Even earlier experiments by Hall [178] (stars) extrapolated an in-plane magnetostrictive constant of $\lambda_{100} \approx 75 \times 10^{-6}$ for $\text{Co}_{25}\text{Fe}_{75}$ and of $\lambda_{100} \approx 48 \times 10^{-6}$ for $\text{Co}_{10}\text{Fe}_{90}$ for bulk crystal discs. We note, however, that the seed layer material, interface effects between seed layer and CoFe layer, and the sputtering conditions are crucial for the realization of ultra-low damping material [206]. Thus, we rationalize that the magnetostrictive properties can be significantly altered due to interface effects. Low damping $\text{Co}_{25}\text{Fe}_{75}$ was realized on SiO_x [206] and Si [191] using the same seed layers used in this work. To ensure

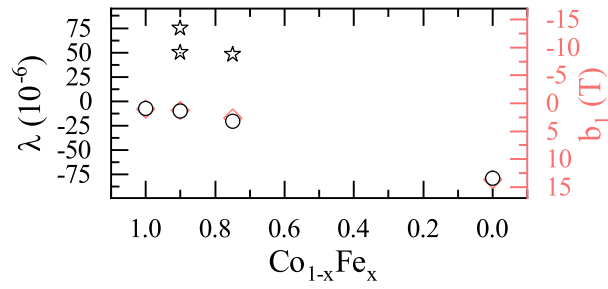


Figure 3.10: Magnetostrictive and magnetoelastic constants for the two $\text{Co}_{1-x}\text{Fe}_x$ alloys and pure metals (Co [79], Fe [202]) for reference. Circles show the magnetostrictive constant (λ_{\parallel}) on the left scale, while diamonds (red) depict the corresponding magnetoelastic constant (b) on the right scale. The star shaped data points correspond to literature values from Refs. 178, 179. Uncertainties in the alloy composition ($\pm 2\%$) are represented by the symbol size for the $\text{Co}_{25}\text{Fe}_{75}$ and $\text{Co}_{10}\text{Fe}_{90}$ compounds, uncertainties in the values of λ_{\parallel} and b are given in the text.

that the low-damping behavior of the Co-Fe is still present when changing the substrate from Si [108] to SiN used here, we performed ferromagnetic resonance (FMR) experiments on unpatterned CoFe-stacks on SiN samples (c.f. Appendix C.2) and find an oop Gilbert damping of $\alpha = (2.1 \pm 0.1) \times 10^{-3}$ for a 10 nm thick $\text{Co}_{10}\text{Fe}_{90}$ film which is in agreement with the values from Schoen et al. [108].

3.6 Discussion and Outlook

In this part, we considered a hybrid system, consisting of a nanomechanical string resonator coupled to a magnetic degree of freedom. This was established by using a multi-layer nano-string where one of the layers was a ferromagnetic metal. How this additional magnetic material changes the mechanical response of the nano-string and how it is influenced by the magnetization of the system, was first discussed theoretically.

We then investigated the magnetostrictive constants of two low magnetic damping Co-Fe alloys grown within a layer stack [108]. To get a quantitative value for the magnetostriction we used a magnetization direction dependent optical resonance frequency measurement of a nano-string, which is covered with the magnetostrictive layer stack. This readout method was first established in [79] and adapted for a many-layer film here. The layer stack for this sample was grown by the group of Justin Shaw at NIST. This method allows the investigation of the magnetostrictive and elastic properties of thin film magnetic layers, even with small sample volumes and high aspect ratios, which both are requisites for future technical applications of spintronic devices, including sensing applications. We extracted a magnetostrictive constant of $\lambda_{\parallel} = (-20.72 \pm 0.33) \times 10^{-6}$ which corresponds to a magnetoelastic constant of $b = 2.62(5)$ T for the ultra low damping $\text{Co}_{25}\text{Fe}_{75}$ alloy, as well as $\lambda_{\parallel} = (-9.8 \pm 0.12) \times 10^{-6}$ and $b = 1.30(2)$ T for $\text{Co}_{10}\text{Fe}_{90}$. With this, we show that the magnetostrictive properties of the two investigated alloys have the same order of magnitude as the constituent materials but differ significantly between the low-damping and normal damping case. CoFe and in particular the ultra-low damping compound $\text{Co}_{25}\text{Fe}_{75}$ shows a size-able magnetoelastic constant and hereby makes an ideal candidate for sensing and magnetization dynamic applications which rely on low damping materials. This is also where the material system differs significantly from the well known low damping material Permalloy. There the low magnetic damping was connected to near-zero magnetostriction [194], whereas for the CoFe alloys it is connected to the particular seed and capping layers [108] but as we found not a near-zero magnetostriction.

PART 4

IMPACT OF ELECTRICAL CURRENTS ONTO MAGNETOSTRICTIVE INTERACTIONS IN NANOMECHANICAL RESONATORS

4.1 Introduction

In this part, we investigate an alternative read out concept to optical interferometry as a tool to determine the mechanical response of a nano-string resonator. While a technical advantage for switching from optical to an electrical readout concept resides in the integrability of future devices, it is also of interest from a research perspective. For optical readout concepts it is well established that the light field can result in an optical tweezer like effect which can change the displacement of the nano-string and hereby the mechanical resonance properties. Moreover, even more profane effects such as heating can play a role. In this chapter, we want to explore an electrical readout of the mechanical response spectrum of the nano-string which is known as magnetomotive readout [81–89]. Its advantages are that the technique is environment independent [86–88], supports a wide frequency range [85, 86], and provides the possibility of reading out entire resonator arrays [89] with minimal experimental overhead. However, little is known how this technique combines with magnetic and magnetostrictive materials.

We will first discuss the theoretical idea of the measurement concept and consider the different effects that need to be taken into consideration. This is followed by a brief description of the used sample as well as the experimental setup. We experimentally observe an unexpected dynamic response in the form of an magnetic field orientation dependent Duffing nonlinearity and discuss possible mechanisms leading to this behavior. In the course of these experiments, we also investigate the heating impact of AC and DC currents onto a nano-string. We then summarize the findings of this part and give a short outlook.

4.2 Electrical readout strategies

The general idea of a magnetomotive readout method is quite simple. A conductive or partly conductive string is exposed to a static magnetic field. This generates an electromotive force, if the string is in motion. This force depends on the string's orientation with respect to the magnetic field as well as the string's maximum amplitude and leads to an induced voltage in the string. This voltage is proportional to the magnetic field penetrating the area which the string covers while oscillating. This area depends on the string's motional amplitude as sketched in Fig. 4.1 b). The induced voltage oscillates with the frequency of the mechanical excitation and its amplitude reflects the mechanical susceptibility [76,207] (cf. Sec. 4.2.3). Besides driving the mechanical motion with a piezoactuator as discussed in Sec. 3.4.1 an alternating current can also be used as excitation stimulus. In particular the oscillating current exerts a Lorentz force onto the string. However, this leads to the complication, that the readout and driving mechanisms are convoluted. As we have an optical readout scheme with piezo-actuation in place (see Sec.3.4.1), we are in the unique position that we can investigate the mechanical response with an without the electrical current at play and thus can identify additional contributions impacting the mechanical response due to its presence.

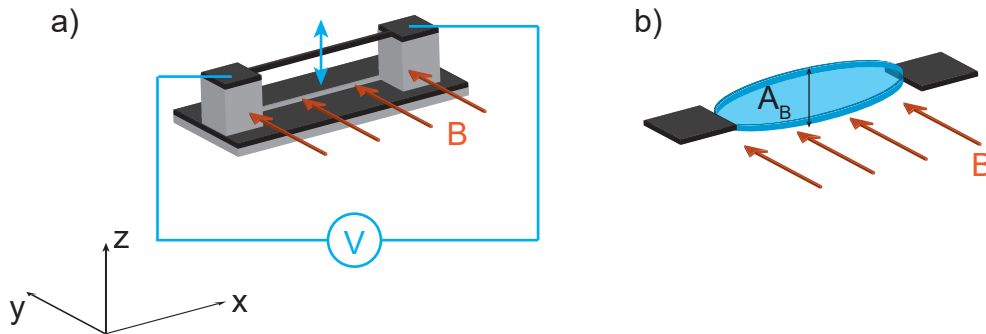


Figure 4.1: a) Sketch showing the sample setup, a metalized Si_3N_4 nano-string is contacted on both sides to enable a voltage measurement. The string is oscillating in z -direction and an external magnetic field \vec{B} is applied in the in-plane y -direction, perpendicular to the string. b) Schema showing the imaginary loop created by the moving nano-string penetrated by the external magnetic field. The light blue area indicates the area swept by the moving string during oscillation.

4.2.1 Lorentz force considerations

We will now first consider the effects of the Lorentz force on a nano-string system, followed by the theoretical description of the magnetomotive readout technique. We then consider the heating effects in a nano-string when adding additional currents through the string itself and briefly discuss the emergence of the anisotropic magneto resistance in a magnetic nano-string. The most obvious contribution provided by the electrical current is

the presence of an induced voltage which can back-act onto the mechanical motion. Due to Faraday's law of induction, the voltage along the string is

$$U_{\text{ind}} = -\dot{\Phi} = -B\lambda_m l \dot{z}(t), \quad (4.1)$$

if we consider the string, or at least the metallic layer, to be homogeneous. Here l is the length of the string, the factor λ_m accounts for the mode shape of the displacement, B is the magnetic field applied perpendicular to the long side of the string, and z is the string displacement (see Fig. 4.1). The mode shape depends on the details of the clamping [123, 164, 208]. As U_{ind} oscillates with the frequency of the displacement and reflects the mechanical susceptibility, it can also be used to determine the resonance frequency and the mechanical susceptibility of the system. However, due to the finite resistance of the string and the connected circuit $R = R_{\text{circuit}} + R_{\text{string}}$ the voltage also causes an induced current along the string. This induced current is given by

$$I_{\text{ind}} = \frac{U_{\text{ind}}}{R} = -\frac{B_y l \lambda_m}{R} \dot{z}(t). \quad (4.2)$$

As $z(t)$ oscillates, so does the current, which leads to the Lorentz force:

$$F_{\text{Lorentz}} = q(\vec{v} \times \vec{B}), \quad (4.3)$$

with the current direction \vec{v} . This force is then applied over the length of the string and thus we arrive at:

$$F_{\text{L}} = \int_l F_{\text{Lorentz}} ds = l I_{\text{ind}} B_y = -\frac{B^2 \lambda_m l^2}{R} \dot{z}(t). \quad (4.4)$$

In addition, we can also consider a bias current I_{bias} which is sourced by the external circuit through the string. Taking these additional contributions into account, the equation of motion of the nano-string reads (see also (1.34)):

$$\begin{aligned} \ddot{z} m_{\text{eff}} + \Gamma_{\text{m}} m_{\text{eff}} \dot{z} + kz - F_{\text{drive}} - F_{\text{L}} + I_{\text{bias}} l B &= 0, \\ \ddot{z} m_{\text{eff}} + \Gamma_{\text{m}} m_{\text{eff}} \dot{z} + kz - F_{\text{drive}} - l(-I_{\text{bias}} + \frac{B \lambda_m l}{R} \dot{z}(t)) B &= 0, \\ \ddot{z} m_{\text{eff}} + (\Gamma_{\text{m}} m_{\text{eff}} + \frac{B^2 \lambda_m l^2}{R}) \dot{z} + kz - F_{\text{drive}} - l I_{\text{bias}} B &= 0. \end{aligned} \quad (4.5)$$

Using (4.5), we can identify an effective damping Γ_{eff}

$$\Gamma_{\text{eff}} = \Gamma_{\text{m}} + \frac{B^2 \lambda_m l^2}{R m_{\text{eff}}}. \quad (4.6)$$

This shows, that indeed the mechanical response spectrum of a electrically connected nano-string can be influenced by a static magnetic field. The typically measured linewidth Γ_{m} for these strings is in the order of 100 Hz for room temperature experiments. If we assume the characteristic values for the parameters $l = 60 \mu\text{m}$ and $R \approx 2 \text{k}\Omega$ and use for the estimation $\lambda_m = 1$, $\Gamma_{\text{eff}}/2\pi \approx 600 \text{Hz}$ and should therefore lead to an increase in the observable linewidth.

4.2.2 Control of the characteristic mechanical parameters by a quasi static bias current

For the understanding of the experiment, we need to consider the impact of a DC or low-frequency AC current sourced through the string. Where we assume that its frequency is much lower than the mechanical resonance frequency Ω_m ¹. Figure 4.2 depicts the sketch of the current. A DC current through the string is always linked with a voltage difference

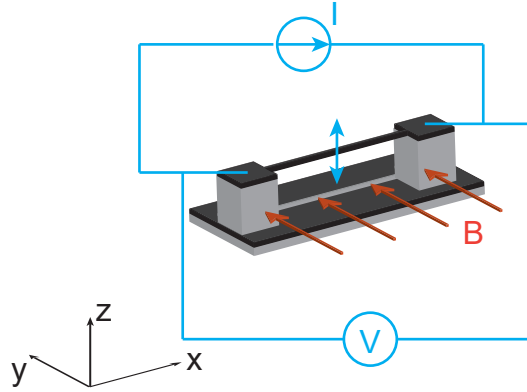


Figure 4.2: Sketch of the sample setup, additionally to the voltage readout a current source enables driving an additional AC or DC current through the string.

along the string. We note that various concepts exist utilizing a tuning scheme of the properties of the resonance based on electric fields [70, 73, 149, 198, 209, 210]. However, this tuning mechanism is ineffective in our experiments, as this concept relies on a dedicated bias electrode next to the string and we use sufficiently low voltages throughout the measurements. The impact of a bias current onto the mechanical resonance frequency via the Lorentz force needs to be considered, for the given parameter set this amounts to a force of ≈ 2.5 pN. This effect is thus negligible [209] compared to the shifts in resonance frequency due to magnetostrictive and heating effects and can further be seen as constant over the experiment.

In addition any AC or DC current can also result in a heating of the string. Since the metal layer in or on the nano-string has a resistance R , a current I flowing through the string will heat the string via Joule heating

$$P = RI^2. \quad (4.7)$$

The dissipated electrical power deposits heat and thereby causes a change of the temperature of the string. Due to the geometry of the structure the heat flow is restricted resulting in a spatially inhomogeneous thermal profile. The string has a higher temperature compared to the clamps and substrate. This thermal profile can in turn also source heat currents:

$$\dot{Q} = \lambda_T A \frac{\Delta T}{d_S}. \quad (4.8)$$

Here, A is the strings cross section, d_S is the distance the thermal flow has to cover ($d_{S,\max} = l$) and λ_T is the thermal conductivity of the material. For this we assume that

¹Please note, that we will use the label *external* current for this to distinguish it from the previously treated induced current.

the total dissipated power P is converted into heat \dot{Q} . Similar to what was discussed in Sec. 3.2.2, the change in temperature, leads to a change in the effective length [113] of each of the layers. In particular, due to thermal expansion and the differences in the thermal expansion rate the length of the covering layer changes to $l' = l\alpha_m\Delta T$, whereas the length of the Si_3N_4 string becomes $l'' = l\alpha_{\text{SiN}}\Delta T$. Here, α_m and α_{SiN} are the respective thermal expansion coefficients. The difference between these two lengths $\Delta l = l' - l'' = l(\alpha_m - \alpha_{\text{SiN}})\Delta T$ can be viewed as an additional stress in the system, because the shared interface suppresses an actual length difference between the layers [211]:

$$\Delta\sigma = E_{\text{string}}\frac{\Delta l}{l} = E_{\text{string}}(\alpha_m - \alpha_{\text{SiN}}). \quad (4.9)$$

Here E_{string} is the effective Young's modulus of the bi-layer string as defined in Eq. (1.31). Note, that we omit the temperature dependence of the Young's modulus in (4.9), as this effect is negligible compared to the relative expansion coefficient [202]. For the materials and geometries chosen in the experiments presented later, this effect leads to a decrease of the overall tensile stress for increasing temperatures. Thereby, it also leads to a decrease of the strings resonance frequency(1.19):

$$\Omega'_m = \frac{\pi}{l}\sqrt{\frac{\sigma_0 - \Delta\sigma}{\rho}}. \quad (4.10)$$

While naively, this effect could be interpreted as a static response, we point out, that there is a temporal component to this effect. For a DC current, the dissipated electrical power (Joule heating) results in an increase of the temperature of the string, which is determined by a steady state equilibrium between the heat dissipation in the string and the thermal coupling to the environment (mostly via the clamps). Therefore, driving an AC current through the string can result in a more complex behavior. In particular, the two cases to be distinguished are (i) a oscillating frequency slower than the thermal relaxation time of the system and (ii) is a fast AC stimulus, with a frequency exceeding the thermal relaxation time of the system. In the first case, the thermal currents remove the dissipated heat quickly and hence the mechanical frequency oscillates with double the frequency of the charge current. The latter results in an average temperature increase corresponding to a constant mechanical frequency shift.

4.2.3 Anisotropic magneto-resistance

As the metallic layer is magnetic, we also need to consider the impact of magnetoresistive effects, more precisely the anisotropic magneto-resistance (AMR), onto the mechanical properties of the string. This effect, first reported by William Thomson (Lord Kelvin) [212], is based on anisotropic scattering in ferromagnetic materials. A more fundamental explanation of the effect and its microscopic origin can be found in [213, 214]. The AMR is typically described in the form

$$\rho_{\text{AMR}} = \rho_{\perp} - (\rho_{\parallel} - \rho_{\perp}) \cos^2(\Theta_{\text{AMR}}). \quad (4.11)$$

Here, $\Delta\rho_{\text{max}}$ is defined as $\Delta\rho_{\text{max}} = \rho_{\parallel} - \rho_{\perp}$, with ρ_{\parallel} the resistivity measured along the current direction and ρ_{\perp} the resistivity perpendicular to it. The angle Θ_{AMR} is spanned by the current density vector and the magnetization direction \mathbf{M} . For our geometry, we

assume a homogeneous magnetic texture and hence use $R = \rho_{\text{AMR}}l/A$ as resistance of the string. In this sense, we assume that the current is exclusively directed along (x -direction) the string. The magnetization direction is assumed to be restricted in the xy -plane. These restrictions need to be taken into account when considering AMR effects in a (cobalt covered) nano-string environment [76, 78, 207].

4.3 Sample fabrication

The fabrication process for the sample discussed here, is in general the same as was already discussed for the CoFe samples in Sec. 3.3. Therefore, we only discuss the differences between the two samples. The main difference between the samples is the layer stack. For the Co sample, the nano-strings were covered in a 20 nm thick cobalt layer via magnetron sputtering (Fig. 4.3). Furthermore, the geometry of the string's clamping pads was

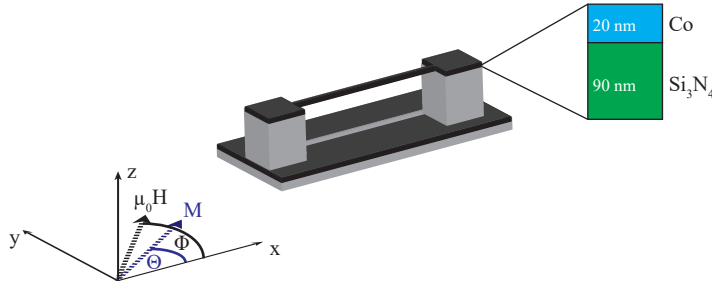


Figure 4.3: Schematic of the bi-layer nano-string. The Si_3N_4 string is covered with a 20 nm thick layer of Co by sputtering. The sample is equipped with bonding pads connected to the string (cf. Fig. 4.4).

changed, and the clamping pads enlarged. This allows us to easier connect the strings electrically via aluminum wire bonds. The layout of the string's on the Co sample can be seen in Fig. 4.4 b) compared to the simple layout used for the CoFe samples (panel a)).

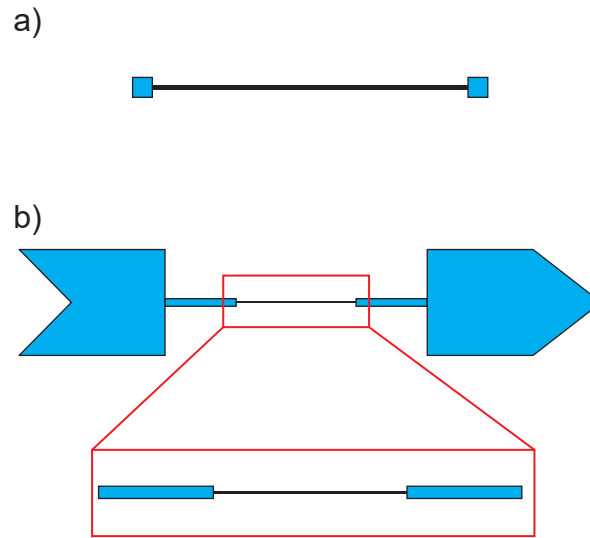


Figure 4.4: Schematic of the nano-string design used: a) Simple double clamped string b) Double clamped string with enlarged, asymmetric pads for wire-bonding to the cobalt layer.

4.4 Measurement setup

In this section, we discuss the measurement setups used to investigate the magneto-motion of a magnetic metalized nano-string, and the impact of external electrical currents onto the behavior of a nano-string. For the optical measurements, we use the optical interferometer used in Part 3 and described in Sec. 3.4.1. Additionally to this, we use the electrical readout setup discussed in the following. For a more detailed description of the measurement setups and their integration, please see App. C.3.

4.4.1 Electrical readout

To integrate the electrical readout technique discussed in Sec. 4.2, the nano-string is electrically connected to room temperature electronics. As depicted in the electrical circuit diagram shown in Fig. 4.5, we can perform voltage measurements and have the ability to source AC and DC currents through the string. Note, that this allows to simultaneously measure the electrical and the optical response, which we will later use in our experiments (see Sec. 4.5). We use a Zurich instruments lockin with two simultaneous recorded inputs. This allows us to measure the resistance of the sample (using an $I_{ac} = 50 - 400$ nA stimulus at 23 Hz) and also the large frequency response at MHz frequencies originating from the motion of the string due to Faraday's law of induction. A more detailed description of the electrical connection scheme, including wire bond connections can be found in App. C.3. The second input (and output) is used to excite the mechanical motion and measure the corresponding displacement via optical interferometry, this part of the measurement is comparable to the VNA measurements used in Sec. 3.4.1. For the electrical measurements discussed later, we distinguish two cases for the electrical readout setup. In case i) the electrical circuit including the nano-string is closed. We use this configuration to feed

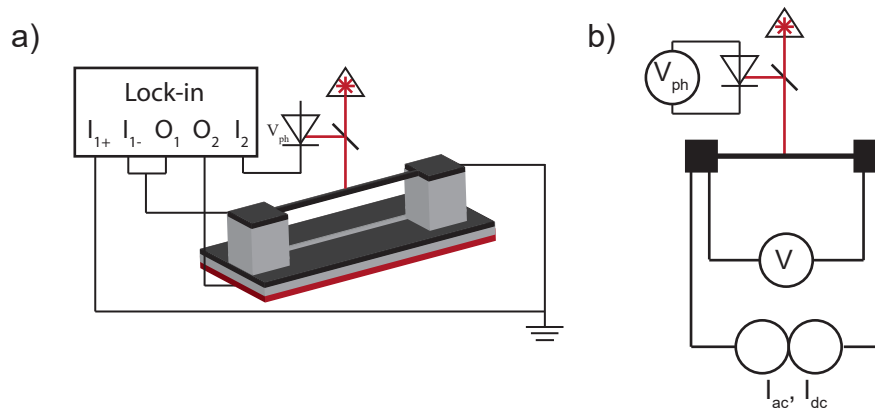


Figure 4.5: Schema of measurement setup for the simultaneous optical interferometry and electrical readout. The optical part is the same as described and showed in Fig. 3.6. a) Connection schema of the lockin amplifier. One channel of the Lock-in is used to detect the voltage across the string (I_1) and to send an external current through the string via O_1 . The signal of the photo-detector is recorded by input (I_2 of the LI. b) Circuit diagram equivalent of the readout setup of the nano-string. The voltage across the string, as well as the photo-voltage are measured. At the same time it is possible to send a DC current an AC current or both through the string. The sample stage is positioned between the pole-shoes of an electromagnet and a piezo actuator can be used to shake the entire sample by using a voltage supplied by O_2 .

a current through the string. This is the situation shown in Fig. 4.5 b). In the second case ii) this electrical circuit is open. In both cases the measurement lines for the voltage measurement are connected. To point out which circuit setup was used for the respective measurement, we introduce two icons representing the respective configurations in Fig. 4.6. Here panel a) corresponds to the closed circuit of case i) and panel b) to the open circuit of case ii).

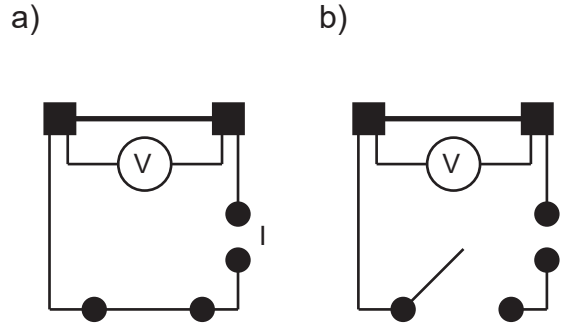


Figure 4.6: Icons representing the different configurations of the electrical readout setup shown in Fig. 4.5. In a) the electrical circuit is closed and a current can flow through the string or be sourced through it. In b) the circuit is open. In both cases the voltage across the string can be measured.

4.5 Magneto-electromotive interactions in an electrically connected nano-string

In this section, we discuss experiments focusing on the comparison of electrical and optical readout concepts for the magnetization orientation and the mechanical displacement. For these measurements we use a Si_3N_4 string covered with $t_{\text{film}} = 20 \text{ nm}$ of cobalt (see Sec. 4.3). In detail, we use the sample layout shown in Fig. 4.4 b) and employ a combined electrical and optical readout setup (see Sec. 4.4.1 and App. C.3).

4.5.1 Simultaneous probing of the mechanical motion using optical and electrical readout

We start the investigation of the sample response by performing a simultaneous measurement of the optical and electrical signatures as a function of the external magnetic field direction Φ . Here, an external magnetic field of $B = 473 \text{ mT}$ was applied. Then Φ was changed stepwise by rotating the electromagnet around the sample in the xy -plane. This follows the same measurement procedure as was already used in 3.5. At each angle step, three measurements are recorded simultaneously. This is shown in Fig. 4.7. In panel a) we show data gathered by optical interferometry, comparable to the measurements carried out in Sec. 3.5. Simultaneously, we measure the induced voltage detected at the stimulus frequency of the piezo actuator (panel b) recorded for a drive amplitude of $V_{\text{piezo}} = 20 \text{ mV}$. Using this technique, we are sensitive to the string's mechanical amplitude. However, as discussed in Sec. 3.5, we expect a distinct amplitude response as the induced voltage originates from Faraday's law of induction. In particular, we expect a suppression of the signal for $\Phi = 0^\circ$ and 180° and a maximum in the detected voltage at $\Phi = 90^\circ$. We indeed observe this in Fig. 4.7. In addition, we observe a pronounced Φ dependent shift in the mechanical resonance frequency, this is due to the magnetostriction in the cobalt. Note, that the background in panel b) shows an increase if the external magnetic field is perpendicular to the string. This effect is not apparent in the optical measurement shown in panel a). We attribute this to the change in the strings resistance R and a following change in the detected voltage. Panel c) shows a *static* measurement of the string's resistance by ap-

plying a slow AC current with $I_{AC} = 100 \text{ nA}$ and $\nu_{AC} = 23 \text{ Hz}$ and measuring the voltage across the string's length (cf. Sec. 4.2.3). As stated by (4.11) the resistance has the largest values for $R(\mathbf{M} \parallel x) \approx 1370 \Omega$ and declines sinusoidally towards $R(\mathbf{M} \perp x) \approx 1350 \Omega$, this corresponds to a $\rho_{\parallel} \approx 9.13 \times 10^{-8} \Omega \text{ m}$ with a ratio of $(\rho_{\parallel} - \rho_{\perp})/\rho_{\parallel} = 1.4\%$ which is comparable to previous measurements by Nynke Vlietstra ($\rho_{\parallel} \approx 1.4 \times 10^{-7} \Omega \text{ m}$) and values from the literature $\rho_{\parallel} \approx 1.7 \times 10^{-7} \Omega \text{ m}$ [207]. This shows, that the AMR changes with Φ but is independent of the piezo drive. The oscillations visible along the frequency axis of panel c) can be attributed to a slight crosstalk in the read out electronics. Figure 4.7 demonstrates, that the electrical and optical readout concepts give comparable results, where there is the difference that the amplitude of the electrical readout signature also reflects the symmetry of the Faraday effect. Moreover, as expected these electrical readout schemes can also be used with magnetic materials. Please note, that due to the change in the resistivity for each Φ , the electric readout of the mechanical resonance frequency is biased slightly differently for each Φ as well, thus a direct amplitude comparison between two slices of panel b) needs to be taken with care.

Next, we want to take a further look into the mechanical response spectrum and specifically the dependence on the external field direction and thus, also the magnetization direction. As shown in Fig. 4.7a) and b), the lineshape of the mechanical response spectrum changes during the measurement. For the parallel case $\vec{M} \parallel x$ ($\Phi = n\pi; n \in \mathbb{N}_0$), the linewidth is smaller ($\Gamma/2\pi \approx 230 \text{ Hz}$) and the lineshape is pure Lorentzian, as predicted by the model introduced in Sec. 1.3 and as can be seen in panel d). When the orientation of the external magnetic field changes towards the perpendicular case $\vec{M} \perp x$ ($\Phi = (n + 1/2)\pi; n \in \mathbb{N}_0$), this changes. First, at small deviations from the parallel orientation, the linewidth begins to broaden. This can be seen in panel e). Here the fit to a Lorentzian lineshape is still possible, however the linewidth is larger compared to the initial value $\Gamma/2\pi \approx 310 \text{ Hz}$. This effect can be explained by an increased effective damping rate $\Gamma_{\text{eff}}/2\pi$ due to the Lorentz force as discussed in Sec. 4.2.1. However, when the orientation approaches the perpendicular case $\vec{M} \perp x$, the lineshape of the mechanical response changes more drastically and starts to resemble a shark-fin. This can be seen in Fig. 4.7 f) This non-linear behavior is usually seen as an effect of Duffing-like behavior of a nano-string. It indicates, that non-linear restoring forces become relevant for the equation of motion (see Eq. 4.5). This effect is unexpected and rather surprising, and cannot be explained by simple Lorentz force considerations as we made in Sec. 4.2.1. The data shown this far, was extracted with the electrical circuit around the sample closed (cf. Fig. 4.6) and thus allowing induced and external currents to pass through the string.

To complement the findings in Fig. 4.7 (and later 4.9), we measure the mechanical response for the field orientations $\Phi = 0^\circ$ and $\Phi = 90^\circ$ (see Fig. 4.8). With this we want to ensure, that the mechanical response does not change depending on external magnetic field strength. Panels a) and c) show, optical and electrical readout measurements, and showcase that the characteristic shark-fin lineshape observed for $\Phi = 90^\circ$, becomes visible from $B \geq 250 \text{ mT}$ and increases towards higher magnetic fields. In the parallel case $\Phi = 0^\circ$, the spectrum remains unchanged. For the parallel case we chose to observe the mechanical response spectrum for even higher magnetic fields up to 630 mT , and observe no changes in the linewidth up to this field. We note, that the field of 630 mT is larger

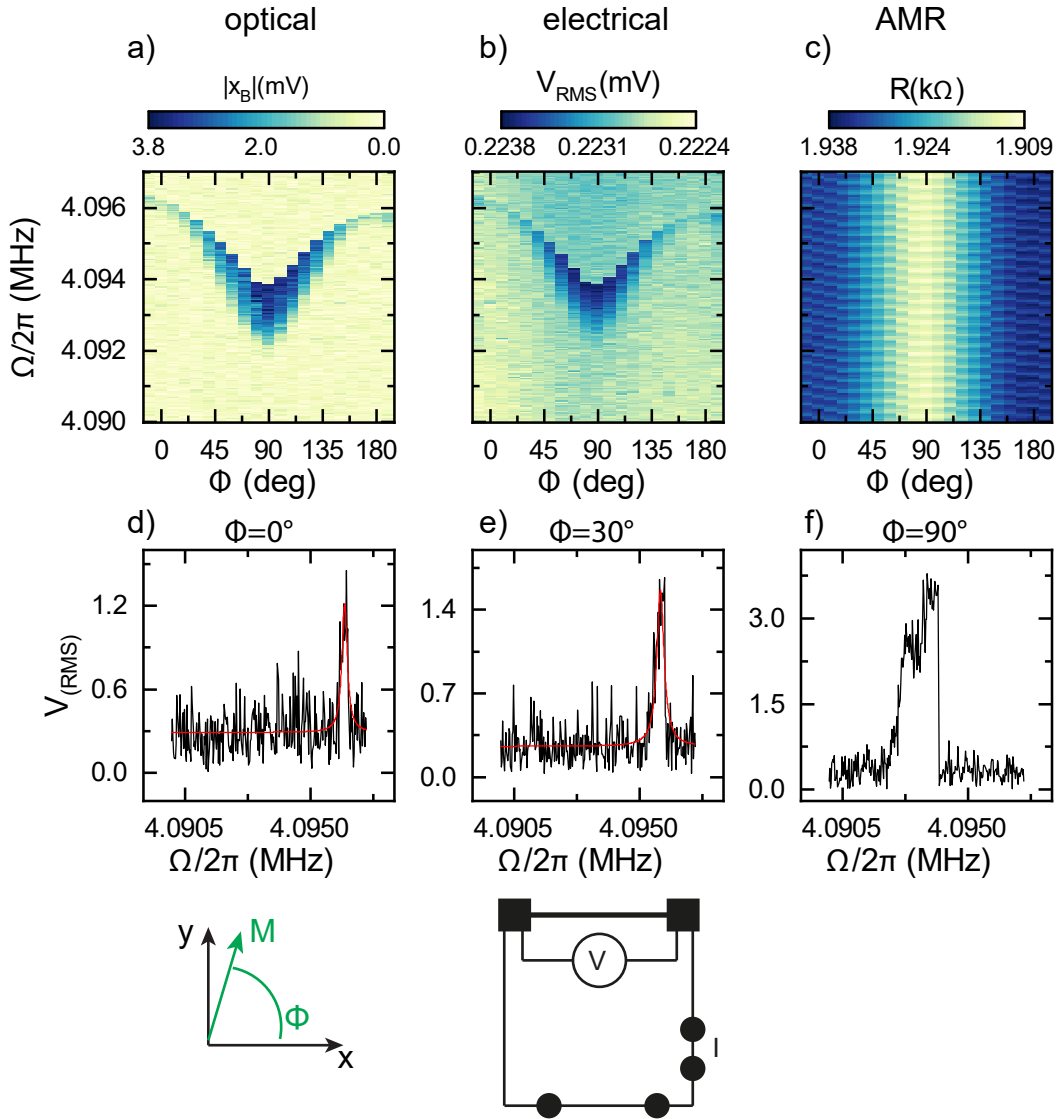


Figure 4.7: Raw data set of the combined electrical and optical readout methods. Φ denotes the angle between the strings long axis and the external magnetic field. The y -axis shows the piezo drive frequency. a) optical readout at drive frequency. b) AC electrical readout at drive frequency. Both a) and b) show the mechanical response spectrum, with dark color denoting high mechanical amplitudes. Note the typical $\cos^2(\Phi)$ dependence of the resonance frequency due to magnetostriction in the material. Also note the highly increased linewidth for $\Phi \approx 90^\circ$. c) Static AMR measured with a $\nu = 23$ Hz AC current ($I_{AC} = 100$ nA), the data shows a reduction in resistance for $H \perp x$. The external magnetic field strength was set to 473 mT. The piezo actuator was driven with $V_{piezo} = 20$ mV. The panels d-f) show cuts along different set angles (0° , 30° and 90°) from panel a) and showcase the change in lineshape. The lineshape starts as a Lorentzian (0°), widens up (30°) and shows nonlinear behavior at 90° .

than any anisotropy fields known for the sample material Co and the geometry ². The

²The saturation magnetization for cobalt is given as 1167 kA m^{-1} , and thus the shape anisotropy can be approximated as $\mu_0 H_{\text{aniso}} \approx 22 \text{ mT}$ [79, 144].

inversion of the magnetic field leads to the same observation. The same is true for all the measurements shown in this section and hence we note that the effects are symmetric in B .

We next discuss the presence of the electric circuit on the observed non-linear signature.

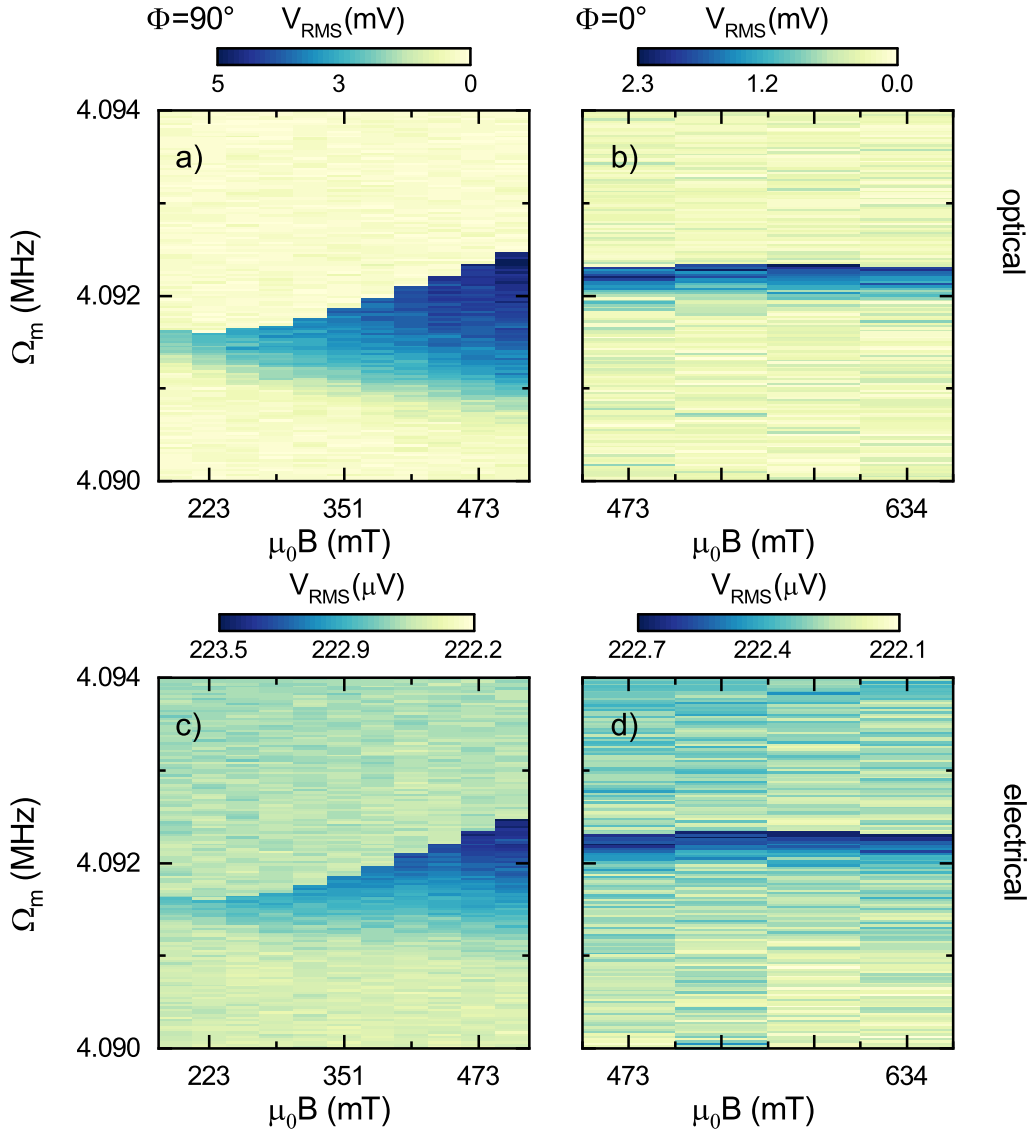


Figure 4.8: Magnetic field sweeps for the two extreme angles $\Phi = 0^\circ \parallel x$ and $\Phi = 90^\circ \perp x$ separated in columns, the rows show the respective optical and electrical readout. For $\Phi = 0^\circ$ the linewidth and frequency of the string does not change with increasing external field (b,c)). In the perpendicular case $\Phi = 90^\circ$ the frequency and linewidth change visibly. This can be attributed to magnetostrictive effects. To check for effects in the parallel case, the magnetic field strength is set to the technical limit of 630 mT.

While the non-linear response is evident for the configuration of a closed circuit (Fig. 4.7), the mechanical response remains in the linear regime if the circuit is set to „open “and no additional bias current is applied (see Fig. 4.9). In this case no AMR measurement

can be performed. The magnetomotive readout is much closer to the noise limit, but can clearly be observed. The linewidth and lineshape stay relatively constant for all external field directions, as the effective linewidth remains at $\Gamma_{\text{eff}}/2\pi \approx 300$ Hz independent of the magnetic field orientation. We note that Fig. 4.7 and 4.9 use the same external magnetic field ($B = 473$ mT) and the same piezo drive voltage ($V_{\text{piezo}} = 20$ mV). The slight shift in the initial resonance frequency can be attributed to a shift in the string temperature due to current heating (cf. Sec. 4.5.2). Further analysis shows, that the linewidth in both measurements at $\Phi = 0^\circ$ is comparable, $\Gamma_{0^\circ, AC} \approx \Gamma_{0^\circ, noAC} \approx 300$ Hz. For the second measurement, this broadens slightly for $\Phi = 90^\circ$, and the amplitude also is reduced here. From this we can learn, that the impact of only having an external magnetic field perpendicular to the string, shifts the resonance frequency according to the magnetostrictive effect ($\Delta\Omega_m(I = 0) \approx 1500$ Hz) and, a slight linewidth broadening paired with a slight decrease in mechanical amplitude can be observed. However, the Lorentz force consideration made in Sec. 4.2.1 is not applicable in this case. For the case with an added AC current through the string, this magnetostrictive shift can not be easily determined since the bare resonance frequency is not straightforwardly identifiable. Estimations of the shift via the low frequency offset of the mechanical feature yields $\Delta\Omega_m(I \neq 0) \lesssim 1800$ Hz. This puts it in the same range as the value in the experiment without electrical currents. Thus the magnetostrictive effect seems not to be affected the observed change in the mechanical response. This motivates us to expand the equation of motion presented in Sec. 4.2 by

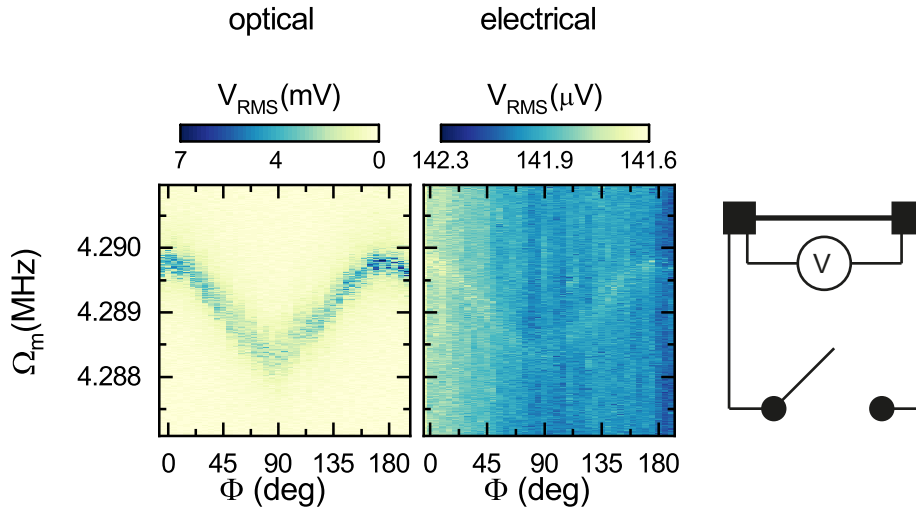


Figure 4.9: Raw data set of the combined electrical and optical readout methods. Φ denotes the angle between the strings long axis and the external magnetic field. The y-axis shows the piezo drive frequency. a) Electrical readout at drive frequency and b) optical readout at drive frequency. Both a) and b) show the mechanical response spectrum, with dark color denoting high mechanical amplitudes. Due to no external current in the string, the signal to noise ratio for the electrical readout in a) is significantly smaller compared to the measurements shown in Fig. 4.7. Note the typical $\cos^2(\Phi)$ dependence of the resonance frequency due to magnetostriction in the material. The piezo-actuator was driven with $V_{\text{piezo}} = 20$ mV and the external magnetic field strength was set to 473 mT.

including a Duffing term (cf. Sec. 1.3.2) in Eq. 4.5:

$$\ddot{z}m_{\text{eff}} + (\Gamma_m m_{\text{eff}} + \frac{B^2 \lambda_m l^2}{R})\dot{z} + kz + \alpha m_{\text{eff}} z^3 - F_{\text{drive}} - lI_{\text{bias}}B = 0. \quad (4.12)$$

We now want to consider, how the effect visible in Fig. 4.7 can be explained. During the sweep of the external magnetic field direction, the response spectrum of the string changes from a linear to a non-linear behavior. This behavior could be explained by several means. One possibility is an increase in the string's amplitude. This was shown in 1.3.2 as a possibility to drive a resonator into the nonlinear regime. However, the driving force exerted by the piezo does not change during the measurement, excluding this reason. A second possibility is a decrease of the damping Γ_{eff} of the system. This would allow for larger mechanical amplitudes and could be a reason for the Duffing like non-linear response in the region of interest ($\Phi = 90^\circ$). However, the Lorentz-force induced additional damping contradicts this model. Alternatively, a change in the Duffing parameter α would also explain the effect. This would make $\alpha(\Phi)$. and magnetic field dependent. the Duffing parameter was defined in 1.3.2 as

$$\alpha \equiv \frac{n^2 E \pi^4}{4l^4 \rho}, \quad (4.13)$$

containing material and geometric parameters. None of which are expected to show a dependence on the magnetic field or magnetization direction. In addition we need to account for the observation that α is only altered when a current flows through the string. As discussed in Sec. 4.2.2 and mentioned above, the additional AC current leads to a temperature increase in the string itself. The Young's modulus of Co and Si_3N_4 is known to be temperature dependent as is true for many materials [215–219], however typically an increase in temperature leads to a decreasing Young's modulus, which does not explain the observed data. Furthermore, we will show in Sec. 4.5.2, how the mechanical response changes due to heating, introduced by an additional current, in more detail. There we will also see, that the temperature change does not explain the change in the mechanical response spectrum. We will now, rather safely, assume that the following parameters remain unchanged during the measurement: i) the gas pressure ($p < 0.01$ Pa), as the sample is operated in a controlled environment. ii) the current flowing through the string is well controlled. However, we note that the effect depends on the chosen configuration and the current level.

In this respect, we can discuss the AMR as the potential origin of the observation. The overall resistance of the string changes depending on the magnetization direction, and hence the resistance R of the string in Eq. 4.12 has an angle dependent part:

$$R = R_0 + R_{\text{AMR}} \cos^2(\Phi). \quad (4.14)$$

This in itself would not lead to a large change in Γ_{eff} , as the AMR resistance is typically in the order of $\approx 1\%$ of R_0 . However, the dynamic of the system and its oscillation in z could lead to a more intrinsic dependence of R to a z^2 term. This is sketched in Fig. 4.10. The oscillation of the string leads to a $\dot{z}(t)$ dependence. The magnetization depends on the external field direction and also gets an oscillatory term, which in turn makes the resistance of the string z^2 dependent. This could in consequence lead to a $z^2(t)\dot{z}(t)$ term in the equation of motion, which can lead to similar non-linear effects as a $z^3(t)$ term [118]. This conjecture could allow to explain the emergence of the

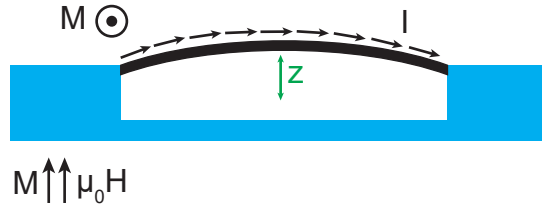


Figure 4.10: Sketch illustrating the interplay of the oscillating string in an external magnetic field when a current is passing through the string. The current as well as the magnetization gain dependences on the amplitude and frequency of the oscillating string.

non-linear behavior observed in Fig. 4.7 and its absence in Fig. 4.9. However, further experiments with non-magnetic materials are required to pinpoint the origin to the AMR. By repeating the measurements with a sample where the Co layer is switched for a non-magnetic metal e.g. Au, the effect should not appear if it indeed originates from the AMR.

4.5.2 Temperature shifts due to current

After discussing the mechanical response spectrum and its dependence on the external magnetic field as well as the direct effects of an additional current sent through the string, we now want to elaborate on a secondary effect. As all electric devices, the nano-string shown in the measurements in this section, has a resistance R . This resistance was shown to be around $R \approx 2000 \Omega$ in Fig. 4.7. This resistance will lead to power dissipation if a current flows through the string, and this power dissipation will lead to an increase in the string's temperature. From a theoretical standpoint this was discussed in 4.2.2, now we will take a look into the experimental consequences. This is showcased in Fig. 4.11. For this consideration, no magnetic field was used. Here we show a piezo drive voltage sweep for different conditions. Panel a) shows a measurement without any added current through the string, and in the absence of an external magnetic field. Here we see the initially Lorentzian shaped mechanical response, which becomes Duffing like for larger excitation powers. In this panel we also define the *bare* mechanical frequency Ω_m^0 as the center frequency at the lowest excitation power. In panel b) we show the same measurement, but with an added DC current of $I_{DC} = 400 \text{ nA}$ sent across the string during the measurement. As we can see, the general mechanical response spectrum does not change. It is however shifted to a lower frequency by about 1 kHz, due to the change in the string's temperature. The fact that the Duffing spectrum for higher excitation powers looks unchanged, also is an indication for no change in temperature during this time. This suggests, that the current increases the temperature of the string, but reaches a new thermal equilibrium faster than the data acquisition can occur. This changes in panel c), here the additional current is applied in the form of a slow sinusoidal AC current with $I_{AC} = 400 \text{ nA}$ and a frequency of 23 Hz. In this case the change in the mechanical response spectrum is more distinct. For low piezo excitation powers, we see not only one undisturbed Lorentzian peak, but a double peak structure. The peak lower in frequency is close to the frequency value visible in panel b), whereas the higher frequency peak is

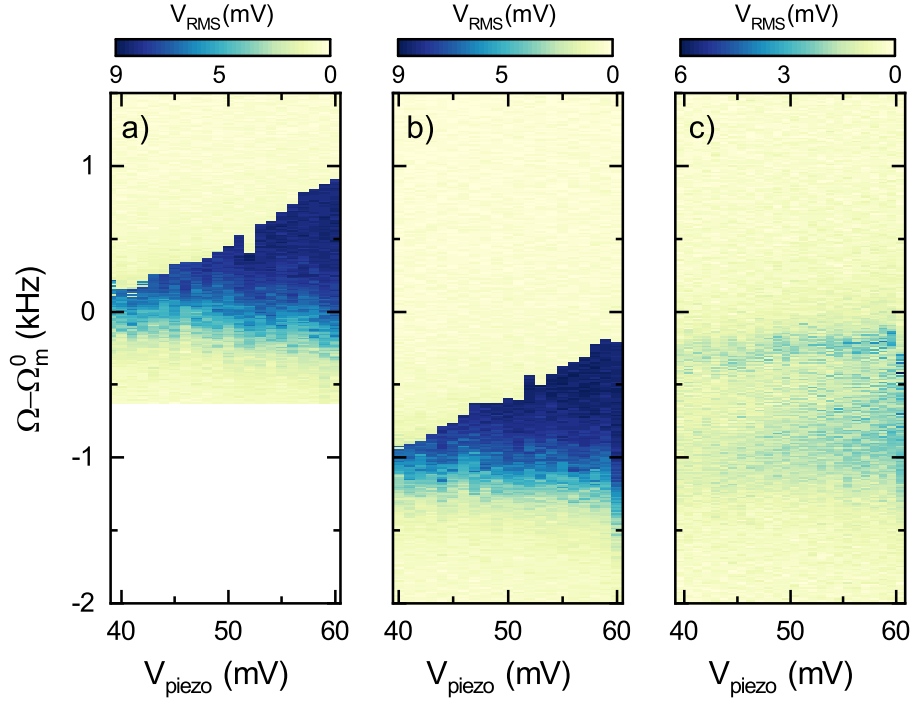


Figure 4.11: Mechanical response spectrum during a piezo drive-power sweep. For a) no AC or DC current was sent through the string, in b) a DC current of $I_{DC} = 400 \text{ nA}$ was applied and for c) an AC current with $I_{AC} = 400 \text{ nA}$ and a frequency $\nu = 23 \text{ Hz}$ was sent through the string. The static current results in a straight resonance frequency shift. For the alternating current, the resonance frequency has a static shift, but two frequencies are discernible for low drive powers, here the alternating current leads to an oscillation in the resonance frequency. By carefully setting the measurement parameters both are visible as a broadened double peak structure.

significantly higher in frequency, but not reaching the undisturbed frequency value shown in panel a). This suggests, that the oscillation of the current is slow enough for the string to thermalize partially within one current cycle and thus two distinct resonance frequencies can be measured. Also the oscillating current leads to a lower dissipated power over time compared to the direct current, which explains the difference in the reached minimum frequency. Towards higher piezo drive powers, the mechanical response spectrum broadens and no distinction between two separate peaks can be made anymore. The data indicates a broadening towards a Duffing-like peak shape for the lower frequency peak, but it allows no certain statement for the upper frequency peak before they merge. However, neither does reach the pure Duffing shape which can be seen in panel b), which is in agreement with the attribution of the effect to the AMR.

We now can compare the model for heating discussed in 4.2.2 with the actual resonance change between panels a) and b). Using the extracted resonance frequencies from the lowest piezo drive powers, and the thermal expansion coefficients of Co and Si_3N_4 [202], we can evaluate Eqs. (4.9) and (4.10), and get a temperature difference of $\Delta T_{\text{exp}} = 0.293 \text{ K}$.

If we now take the known values for the string from fabrication and measurement, we can also evaluate Eqs. (4.7) and (4.8). We thereby calculate a temperature difference of $\Delta T_{\text{calc}} = 0.184 \text{ K}$, using the known values for $I = 400 \text{ nA}$, $R = 1938 \Omega$ and the strings geometry. For the thermal conductivity, we assumed a weighted mean of the conductivities of Co and Si_3N_4 [202]. The difference between the value determined from the experimental values and the one calculated from the model shows, that the approximations taken in the model are not entirely justified, even if they are in the same order of magnitude. We attribute this to a different thermal conductivity of the string, most likely in the area of the clamping pads. This depends not only on material but also the specific geometry and may lower the overall thermal conductivity and can be imagined as a bottleneck. This assumption is also supported by the fact, that a thermal equilibrium seems to be achieved fast, if at a slightly higher temperature than expected, as can be seen in in Fig. 4.11. Apart from showing the influence of heating on the resonance frequency of a nano-string the comparison of panels a) and b) also indicates that the Duffing behavior does not seem to change depending on the string temperature alone. Furthermore the fast thermalization visible in panel c) gives insight in the thermal flow in a nano-string structure.

4.6 Discussion and Outlook

In this section, we discuss an alternative scheme for the readout of the motion of nano-string resonators covered with a ferromagnetic material. For this, we used a bi-layer nano-string where the bottom layer consists from Si_3N_4 whereas the top layer is made from Co. This cobalt layer is electrically connected via the clamping pads. We compare this magnetomotive readout method to a simultaneous readout using optical interferometry to compare them. In particular, we observe that the electrical connection of the string to an external circuit drastically alters its mechanical response spectrum. To be specific, we find a drastic increase in the effective Duffing parameter. Moreover, applied electrical currents also affect the temperature of the string via Joule heating. Again, this impacts the resonance frequency of the metalized string. The full impact of electric currents onto the mechanical and magnetic properties of nano-string resonators still holds several questions, in particular if the observed non-linear behavior is restricted to magnetic materials and specifically if this effect originates from the AMR. They go however, beyond the scope of this thesis.

PART 5

SUPERCONDUCTING NANO-MECHANICAL CIRCUIT DEVICES

5.1 Introduction

In this part of the thesis we will move beyond classical physics and discuss quantum phenomena. The quantum nature of light [220,221] coupled with the quantized level structure of atoms, result in the field of quantum electrodynamics (QED) [222,223]. A powerful platform for QED in the microwave regime are integrated superconducting circuits [224,225]. In circuit QED (cQED), superconducting qubits [226] act as artificial atoms. High quality coplanar waveguide resonators [227], or three-dimensional cavities [228] are used to contain the quantized light field and allow experimental access. In this field of QED and cQED, the Jaynes-Cummings model [229] is a powerful tool to understand the interaction between quantum states and physical matter. Further, superconducting circuits show a high engineering flexibility. This can be seen in the fact that they allow for strong [102,224,230], ultrastrong [231–233] and even controllable coupling [234–238]. Recently, the research in this field culminated in the demonstration of quantum supremacy by Arute et al. [239]. We want to discuss a different approach to use circuit QED. By coupling circuit QED devices with mechanical elements, we enter the field of electromechanics, the microwave pendant to the more known optomechanics [240]. This can be done by e.g. integrating a nano-string resonator into a coplanar waveguide microwave resonator [90,91]. It was demonstrated, that strong coupling is reachable in a cavity electromechanical system [102]. The same system was further used to cool the mechanical resonator to its quantum ground state by sideband cooling [96]. More recently coherent state transfer between an itinerant microwave field and a mechanical resonator was shown [104]. Further, the readout of a superconducting qubit by using a nano-electromechanical system was proved feasible [41] and the integration of a mechanical element in a circuit qubit was shown [106]. All of this shows not only the feasibility to combine mechanical elements with cQED devices, but also, that the combination of nano-electromechanics with cQED is a powerful approach

to delve into the quantum nature of mechanical motion. It also gives an insight on how these hybrid systems can be used to enable ultra sensitive force sensors [94, 241, 242], new quantum information processing technologies [105, 243–245] as well as access to observing quantum behavior in large scale structures [246, 247].

Here, we will discuss a hybrid system, situated in the field of superconducting nano-electromechanics and circuit QED. We will discuss the integration of a mechanical resonator in the form of a nano-string into a superconducting circuit qubit, specifically a transmon qubit. This approach was proposed by Abdi et al. in 2015 [248], to open several interesting ranges rich in physics. Starting from three-partite entanglement, sideband driven cooling, enabled by enhanced phonon-photon coupling strengths, to the generation of mechanical Fock- or number states. Furthermore, also the possibility to use a mechanical resonator, with its high quality factor, as an intermediate storage in a qubit environment can be seen as a prospect. To set the context of the work done towards this goal within this thesis, we will first outline the prior state of the art at the WMI, concerning this specific topic. We will then consider second generation samples. We will compare finite element simulation predictions with actual measurement results. At the end we discuss the merits of using a different transmon layout, specifically the X-mon layout as a possible new platform for integrating a nano-string into a qubit.

5.2 Embedding nano-electromechanics in superconducting quantum circuits

In this section, we present an overview to the efforts invested into a project aiming to technically realize quantum hybrid structures based on mechanical elements in a superconducting circuit QED environment. Naturally, the mechanical element for this project is made from aluminum, because this material choice enables larger electromechanical couplings compared to insulating Si_3N_4 strings [91, 92, 102, 125, 126, 211, 249]. The first step within this project is to combine circuit QED device layouts [224, 250–252] with nanomechanical string resonators [91, 125, 211]. The critical aspect from the fabrication perspective, is the release of the nano-string. This requires using etching techniques to be applied to the sample chip hosting a superconducting qubit with two delicate Josephson junctions. In particular, for the first generation of devices we decided to locally separate the elements qubit and nano-string on the chip as far as possible. The layout for this sample is shown in Fig. 5.1. Here panel a) shows the full layout as a sketch. The $6 \times 10 \text{ mm}^2$ silicone substrate hosts a microwave resonator in coplanar waveguide (CPW) design. The $\lambda/2$ resonator has a center frequency of $\omega_c/2\pi = 5.875 \text{ GHz}$. The two elements are placed next to the two voltage anti-nodes, which are spatially located close to the coupling capacitances. These positions are indicated in Fig. 5.1 a). The red box indicates the position of the transmon qubit¹ which is shown in detail in panel b). The green box indicates the position of the nano-string. A more detailed picture of the nano-string also showing the release from the substrate is shown in panel c). For the detailed fabrication process we refer to Ref. [253]. In the fabrication, the release process was of particular concern as the acceleration voltage and plasma used for the RIE process was identified to potentially damage the Josephson junctions. Nevertheless, conservative settings and protection of the transmon qubit

¹The name transmon is an acronym for a transmission line shunted plasma oscillation qubit [250].

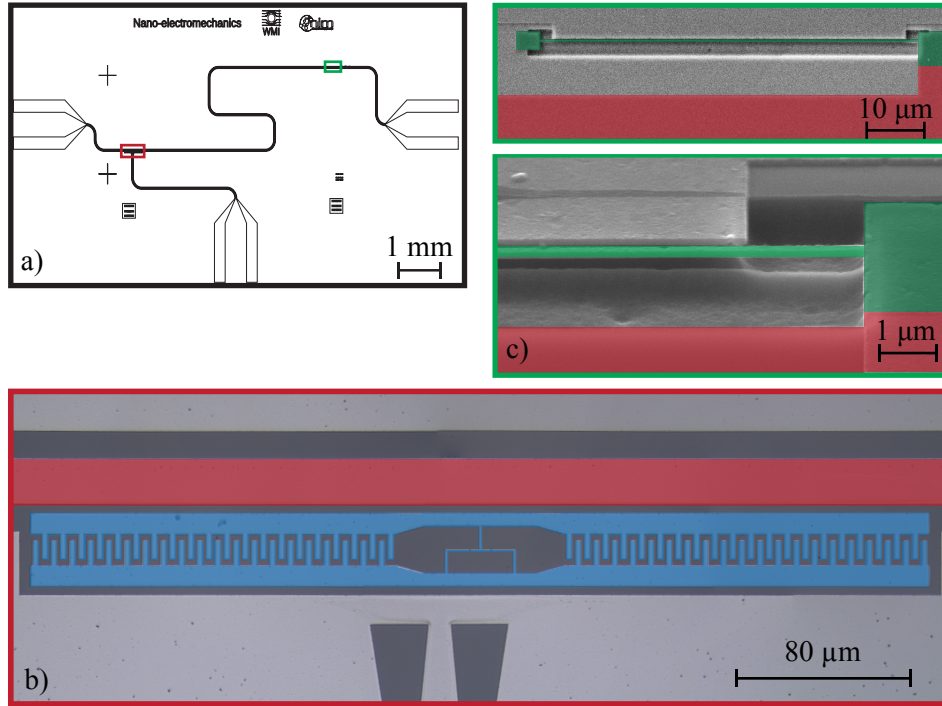


Figure 5.1: Picture of the sample layout, containing a spatially separated circuit qubit and nano-string resonator. Panel a) depicts the whole sample chip with a transmon qubit and a mechanical string coupled to the same $\lambda/2$ microwave resonator. Panel b) shows a micro-graph of the qubit area. The qubit is colored in blue, whereas the cpw resonator is red. In panel c) two SEM pictures of the string are visible, the upper panel shows the whole string (green) connected to the microwave resonator (red). The lower panel shows a close-up of the clamping area, showcasing the release from the substrate. Also the gap between the string and the adjoining groundplane can be seen.

by using a carefully chosen sample layout enabled to realize a working device which was later used to quantitatively compare effects of circuit QED with signatures of the optomechanical Hamiltonian. In particular, as published in Ref. [249], we demonstrated, that the capability to measure photon numbers using the ac-Stark effect of the transmon and the electromechanically induced transparency [?, 103, 252, 254–256] yield quantitatively corroborative results. In detail, the device parameters for this sample are the resonator frequency of $\omega_c/2\pi = 5.875$ GHz, with a linewidth of $\kappa_c/2\pi = 1.468$ MHz. The transmon plasma frequency was determined as $\omega_q/2\pi = 7.916$ GHz with a linewidth of $\kappa_q/2\pi = 6$ MHz. The mechanical resonator has a resonance frequency of $\Omega_m/2\pi = 3.150$ MHz with a linewidth of $\Gamma_m/2\pi = 12.4$ Hz, which results in a Q-factor of ≈ 250.000 corresponding to a thermal coherence time of $38 \mu\text{s}$ at $T \approx 50$ mK. The coupling between the qubit and the resonator was extracted as 134 MHz and the coupling strength between the microwave resonator and the nano-string was determined to be $g_0/2\pi = 0.31$ Hz. Building on top of the insights gained in [249, 253], we performed simulations and prototyping on a second generation device. This work was done together with Lisa Rosenzweig, as part of her Master's thesis. The goal of this project, was to increase the coupling strength between a nano-string resonator

and a CPW microwave resonator, as a study to further the understanding of engineering of the coupling mechanics. An additional requirement is, that the same microwave resonator is coupled to a qubit, and that a fast readout of this qubit is possible. For this reason, two separate microwave resonators were used. One resonator is coupled to both the qubit and the resonator, and is optimized for a high coupling strength between nano-string and microwave resonator. This was mainly done by engineering the impedance of this resonator. The second resonator is only coupled to the qubit and is optimized for qubit control and readout. This was done to go a step further from the first sample presented in [253] towards the one proposed by Abdi et al. [248]. We will discuss the design of the transmon qubit used in this device here. The results on the design and prototyping considering the high impedance microwave resonators and the efforts of coupling them with a nano-string as well as the measurements on those samples, will not be discussed in detail and can be found in Lisas masters thesis [257]. By focusing on the simulations and engineering of the qubit layout, we will gain insight into the necessity of changes to the qubit layout when considering integrating a nano-string within the qubit. This research and development of the qubit design, integrating a nano-string will be shown in the following. The work was carried out together with Nathalie Segercrantz during her time as a postdoc researcher at the WMI. This second project was carried complementary and subsequent to the design and fabrication work done during the Master thesis of Lisa Rosenzweig.

5.3 Modeling and simulations

Based on the knowledge and confidence gained with the design discussed in Sec. 5.2 we next discuss the alterations required to realize the proposal by Abdi et al. [248]. Key aspects encompass the integration of the nano-string into a transmon type qubit and the realization of a significantly larger coupling strength. For this we briefly review some key formulas describing the qubit and its interaction with a nano-string as well as a microwave resonator. We will not derive those formulas in detail, nor will we discuss the rich physics connected to superconducting circuit qubits. We point towards [250, 251, 253, 257, 258] for further information on transmon qubits. One of the main requirements, assumed by Abdi et al. [248], is that the coupling strength between the nano-string and the qubit is significantly large². To reach this, is the goal of the study shown here. However, during the engineering of this coupling parameter we find that great care needs to be taken to ensure several key parameters of the whole system stay within their specific limits. We will discuss those parameters and their respective limits in the following.

5.3.1 The transmon layout

A microwave resonator can be described as an harmonic $L_C C_C$ oscillator, with an effective inductance L_C and capacitance C_C . However, the level spacing of an harmonic oscillator is equidistant and hence does not allow to address selective transitions. In contrast an ideal qubit is a two-level system. The transmon qubit mimics this two-level behavior even though it is an LC oscillator. In particular, the anharmonicity introduced by the Josephson junctions is chosen to be at a level, where it is significantly distorted to allow addressing selective transitions. In detail, this level of anharmonicity depends in the relative value

²In the order of ten to several tens of Hz.

of the inductance L_J of the Josephson junctions and the qubit's capacitance C_Σ . For a qubit to be considered in the transmon regime, the ratio between the Josephson energy E_J and the charge energy E_C needs to be sufficiently large: $\xi = E_J/E_C > 50$ [250, 251]. The Josephson energy is simply given by the energy of the two contributing junctions, whereas the charge energy is defined by the qubit's overall capacitance:

$$\begin{aligned} E_C &= \frac{e^2}{2C_\Sigma} \\ E_J &= 2E_J^0 |\cos(\pi\Phi/\Phi_0)|. \end{aligned} \quad (5.1)$$

Here, the sum capacitance of the qubit C_Σ is given by the capacitance of the junctions C_J , the coupling capacitance to readout resonators etc. C_g and the intrinsic capacitance of the qubit. An equivalent circuit diagram of the qubit can be seen in Fig. 5.2. The maximum

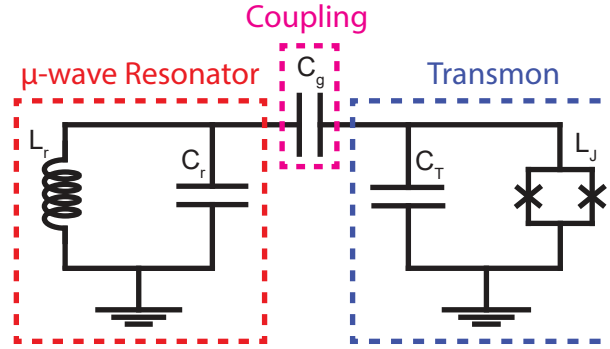


Figure 5.2: Equivalent circuit diagram showing a transmon qubit coupled to a readout resonator via C_g , the capacitance of the qubit is mainly located in a shunting capacitance C_T .

frequency of the qubit is then given by [250]:

$$\omega_q = \frac{1}{\hbar} \sqrt{8E_C E_J}. \quad (5.2)$$

Its anharmonicity, the change in transition frequency between qubit levels, is given by [250]:

$$\omega_{n,n+1} = (E_{n+1} - E_n)/\hbar = \omega_q - E_C/\hbar(n+1). \quad (5.3)$$

Here n is the level index and the energy of one specific level is given by [250]:

$$E_n = \hbar\omega_q \left(n + \frac{1}{2}\right) - \frac{E_C}{12} (6n^2 + 6n + 3). \quad (5.4)$$

Next, we discuss the coupling strengths in the qubit resonator system. The coupling between the qubit and a microwave resonator, mediated by a coupling capacitance C_g is given by [248]:

$$\chi = 4E_C n_{ac} \left(\frac{\xi}{2}\right)^{1/4} = \frac{eC_g}{C_\Sigma} \sqrt{\frac{\hbar\omega_c}{2C_c}} \left(\frac{E_J}{e^2} C_\Sigma\right)^{1/4} \quad (5.5)$$

with the root mean square number of resonator induced cooper-pairs in the qubit n_{ac} . If we now want to integrate a nano-string in a capacitively coupled manner into these qubits, it needs to be a mechanically compliant part of the qubit capacitance $C'_T \rightarrow C_{T,0} + C_T(x)$. It will therefore work as a capacitor between the qubit and the groundplane, as can be

seen in Fig. 5.1 c). This causes a displacement dependent charging energy $E_C(x)$ and the qubit frequency changes accordingly to

$$\omega_q(x) = \frac{1}{\hbar} \sqrt{8E_C(x)E_J}.$$

Here Abdi et al. [248] define the bare coupling strength between the qubit and the mechanical resonator as g_0 via

$$E_C(x) \approx E_C + g_0 n_{\text{phonon}},$$

with n_{phonon} the number of excitations in the nano-string. Consequently g_0 becomes

$$g_0 = \frac{E_C C_T}{d_0 C_\Sigma} x_{\text{zpm}} = \frac{e^2 C_T}{2C_\Sigma^2 d_0} \sqrt{\frac{\hbar}{2\rho_{\text{Al}} w t \pi \sqrt{\frac{\sigma_{\text{Al}}}{\rho_{\text{Al}}}}}}. \quad (5.6)$$

Here $x_{\text{zpm}} = \sqrt{\hbar/2m_{\text{eff}}\Omega_m}$ is the square amplitude of the mechanical zero point motion. This depends on the string's effective mass m_{eff} and resonance frequency Ω_m as defined in Sec. 1.2. The equilibrium distance between the string and the ground plane is defined as d_0 . The effective coupling between the transmon and the nano-string is then given by [248]:

$$g_t = g_0 \sqrt{2\xi} = \frac{C_T}{d_0 C_\Sigma} x_{\text{zpm}} \sqrt{E_C E_J}, \quad (5.7)$$

as the coupling is enhanced by the E_J/E_C ratio ξ , which can be tuned in situ for our sample layout. Abdi et al. also derive a value for the three-body electromechanical mode interaction between the microwave resonator, qubit and mechanical string resonator [248]:

$$g_{\text{tc}} = \frac{E_C C_T}{d_0 C_\Sigma} x_{\text{zpm}} \frac{C_g}{2e} \sqrt{\frac{\hbar\omega_c}{2C_c}} \left(\frac{\xi}{2}\right)^{1/4}. \quad (5.8)$$

Notably, both electromechanical coupling strengths can be enhanced by increasing the E_J/E_C ratio. The engineering challenge is to increase g_0 from the first sample shown in [249, 253] where the coupling was $g_0/2\pi = 0.31$ Hz. For a large coupling strength g_0 , the ratio of mechanically compliant capacitance $C_T(x)$ to non-compliant capacitance C_Σ needs to be as large as possible. The mechanically compliant capacitance $C_T(x)$ is limited by the geometry of the nano-string, therefore we will consider decreasing the non mechanically compliant capacitance here. However, great care needs to be taken, such that all the other parameters, like the qubit frequency, anharmonicity and coupling to the microwave resonator do not suffer from this. Namely the resonance frequency should stay within the experimentally feasible levels, and the coupling strength between qubit and microwave resonator should be large enough to remain in the strong coupling limit $\chi \gg \Gamma_c, \Gamma_t$.³ Also, apart from the electrical cross-dependences of the system capacitances via C_Σ , physical dependences may occur due to the used sample layout. The initial transmon design shown in Fig. 5.1 has the issue, that the coupling capacitance to the microwave resonator is at the same time also part of the internal capacitance, such that changing C_g does not only affects C_Σ but also C_T . This is a hindrance when trying to optimize the whole design. In Fig. 5.3 a layout used for coupling a transmon qubit to two microwave resonators is shown, here, the coupling to the storage resonator (SR) was designed to be much smaller compared to the coupling to the readout resonator (RR). This was done by

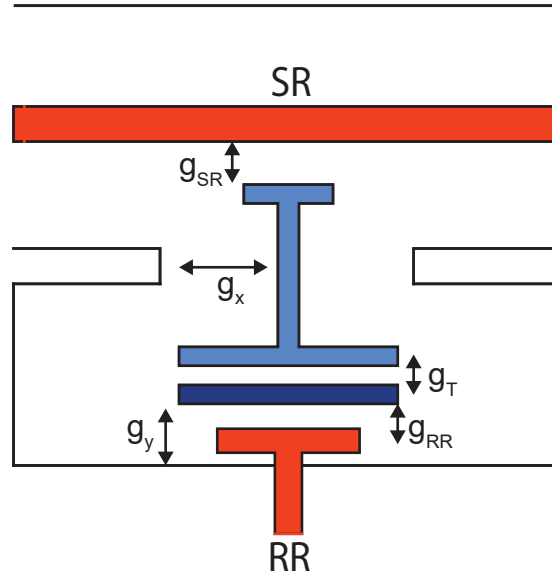


Figure 5.3: Design layout of a transmon structure coupled to two microwave resonators. The capacitance g_{SR} between qubit and storage resonator (SR) is chosen smaller compared to the capacitance g_{RR} between qubit and readout resonator (RR), this results in a smaller/larger coupling strength to those respective resonators. Also the capacitance g_T of the qubit structure itself as well as the coupling capacitances g_x and g_y to the environment are included .

separating the two capacitances $C_{g,SR}$ and C_T . The specifications necessary for a device given in [248] are summarized in Tab. 5.1 for two possible device setups. To design a qubit-resonator-string hybrid device, we use two processes. First, we take the relations shown in ((5.1) to (5.8)) to find an operating point in the parameter regime which fulfills the specifications in Tab. 5.1. Then we design a layout and use finite element simulations to extract the relevant parameters. By using the results of the simulations, we then refine the layout step by step. The explicit simulations involved in designing this layout can be found in Ref. [257]. In short, we used finite element simulations⁴ to simulate the different capacitances of the layout. We use the extracted values to calculate the rest of the parameters. This technique also allows to predict the possible crosstalk between the microwave resonators. As is shown in Fig. 5.3 this resulted in an asymmetry in the qubit structure. The coupling capacitance between the qubit structure and storage resonator is relatively small, lowering the coupling strength between the two. On the other side a strong coupling between the qubit structure and the readout resonator is of benefit, thus the respective coupling capacitance is chosen larger. This results in a physically larger capacitor. The capacitance of the qubit structure itself is mainly comprised by the large central capacitor. Please note, that also the capacitances coupling the qubit structure to the surrounding environment $g_{x,y}$ need to be taken into account, as they influence the

³Here Γ_c is the linewidth (full width half maximum) of the microwave resonator and Γ_q is the qubit linewidth.

⁴CST@Microwave Studio suite

Quantity	set#1	set#2
ξ	150(50) ^a	142(60) ^a
m	1 pg	3 pg
g_0	18.2 kHz	20.6 kHz
$g_t(\xi_c)$	315 kHz	350 kHz
$\chi(\xi_c)$	31.4 MHz	510 MHz
$\Omega_m/2\pi$	10 MHz	1 MHz
$\kappa_c/2\pi$	10 kHz	50 kHz
$\gamma_t/2\pi$	3 kHz	5 kHz
$8E_C n_{ac}/\hbar\omega_c^b$	2.0×10^{-4}	3.4×10^{-3}

Table 5.1: Table from [248] ^a resonance value e.g. $\omega_{tr}(\xi) = \omega_c$ ^b prefactor of the qubit-resonator coupling rate whose fundamental upper bound is ~ 0.1

overall capacitance of the qubit structure. Starting from these results, we designed a transmon with an included nano-string. The conceptual layout for this transmon qubit can be seen in Fig. 5.4 a). In this design, the coupling capacitor towards the microwave resonator was enlarged to engineer the coupling strength. The actual qubit structure is spatially distanced from the resonator, to suppress parasitic coupling capacitances. The main capacitance of the structure, which is comprised by the two capacitor plates, shunted by the loop containing the Josephson junctions was also optimized. Here, the goal was to increase the impact of the capacitance comprised by the nano-string onto the overall qubit capacitance. This can be done by reducing the capacitance provided by the large plates. At the same time, the overall capacitance cannot be too small, since the E_J/E_C ratio of the qubit needs to be within its limits. From a layout perspective, the shunting loop and the nano-string were positioned in such a way, that an external flux line to tune the Josephson junctions can be added. Here, care was taken to suppress crosstalk from this antenna structure to the microwave resonator, as this was an issue we experienced in previous experiments (cf. [257]). Since the complex and involved experimental setups and data acquisition schemes do not contribute to the understanding of the discussion here, we will only compare the simulated and design values to the experimentally extracted values. For information on experimental techniques, we refer to [251, 253, 257]. The design parameters chosen for implementation are summarized in Tab. 5.2. This assumes a string with $l = 20 \mu\text{m}$ length, $w = 120 \text{ nm}$ width and $t = 120 \text{ nm}$ thickness, corresponding to a total mass of the string of $m = 39 \text{ pg}$. Due to the double clamped design, this leads to an effective mass of $m_{\text{eff}} = m/2 = 19.5 \text{ pg}$. The equilibrium distance of the string was set as $d_0 = 150 \text{ nm}$. Further, for the calculations, the Josephson energy was assumed to be similar to previously measured junctions of the same dimensions and design $E_{J,0} \approx 2.5 \times 10^{-21} \text{ J}$ [259]. We will now compare some of the experimentally extracted device parameters to the values gained from finite element simulations of the design layout. By doing so, we gain insight into where there are challenges. These may reside either in transferring the design layout to the actual physical device, or in how well the finite element simulation describes the actual situation. The coplanar microwave resonator, has a designed frequency value of $\omega_c/2\pi(\text{simu}) = 5.4 \text{ GHz}$, compared to this, the experimentally extracted resonance frequency is determined as $\omega_c/2\pi = 5.84 \text{ GHz}$. This shows good agreement between simulation and experiment. However, the quality

Quantity	Value
ξ	153
$\omega_c/2\pi$	5.4 GHz
$\omega_{tr}/2\pi$	18 GHz
$\Omega_m/2\pi$	10 MHz
$g_0/2\pi$	110 Hz
$\chi/2\pi$	92 MHz
$g_t/2\pi$	1.8 kHz
$g_{tc}/2\pi$	18 Hz

Table 5.2: Simulated values for a sample with a layout similar to the one shown in Fig. 5.4a)

factor $Q = \omega_c \kappa_c \approx 1000$ is relatively low compared to previously fabricated resonators with $Q \approx 6600$ [253]. Here, the assumption is, that the challenge lies in the fabrication, not the design. The coupling strength between qubit and resonator is experimentally determined as $\chi/2\pi \approx 10$ MHz. This value shows a significant deviation from the intended value of $\chi/2\pi \approx 92$ MHz. Due this low coupling value it is also impossible to gain further insight into other qubit parameters e.g. qubit linewidth. The reason for the large deviation is not strictly known. However, we can speculate towards several possible reasons. Most stem from the fabrication process. Differently then for previous samples, here the Josephson junctions and the nano-string were in close proximity. As a test, the whole sample was etched without special protection. Thus, also the Josephson junctions are under etched and freely suspended as can be seen in Fig. 5.4 c). The fabrication of the nano-string and the rest of the qubit structure was separated. This was done to allow annealing of the nano-string. We do not know the quality of the interface between qubit and nano-string. I.e. if there are additional junction like structures in this area due to oxidation during the annealing process. In particular since no special effort was made to clean those interface areas before the growing process. A further consideration is, that the qubit structure is partially evaporated over the existing nano-string here the substrate for the qubit structure is uneven. Even though no issues are discernible in the SEM pictures (cf. Fig. 5.4) there may be structural weaknesses in these areas.

5.3.2 The X-mon layout

As an alternative strategy, we study the option to realize the same physics in a X-mon type qubit [258]. This device design has potential improvements compared to the implementation with the *classical* transmon type qubit. The X-mon layout is schematically shown in Fig. 5.5. The capacitance of the structure is not locally constrained, as in the previously shown transmon layout, but rather given by the distributed capacitance of the cross shape, to which it owes its name, to the surrounding ground plane. This allows for a more distributed device geometry. One consequence of this, is that it is possible to use all of the arms of the cross to couple the qubit to other circuit devices, while keeping those

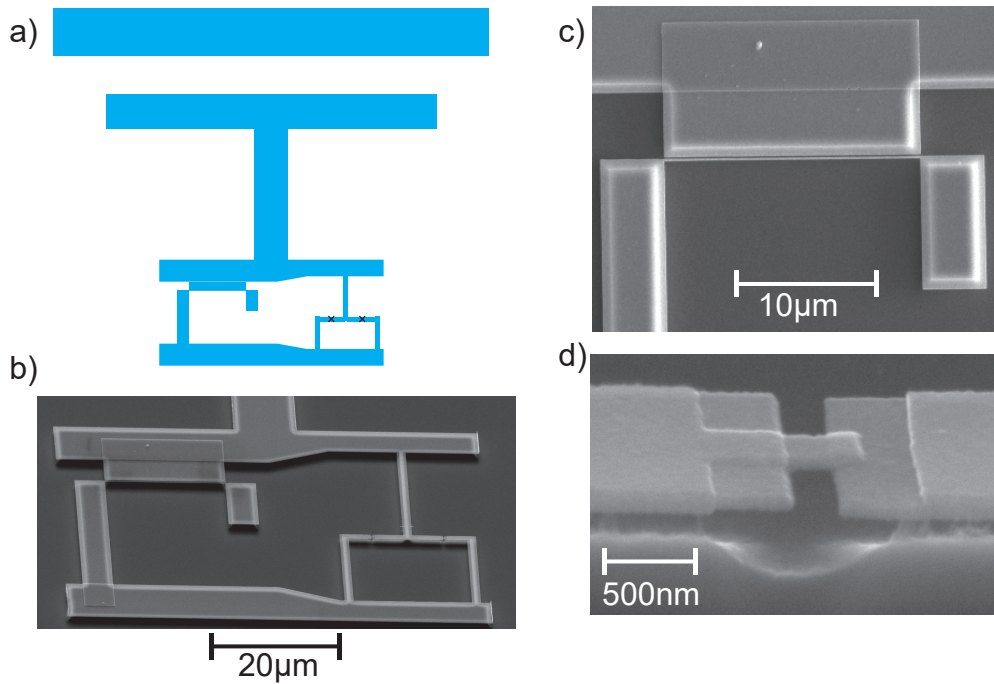


Figure 5.4: a) Schematic of the resonator-transmon-nano-string sample. The transmon is capacitively coupled to a microwave resonator. The bulk capacitor plates are shunted by a SQUID loop on the right hand side, on the other side a nano-string is inserted. Panel b) shows a tilted SEM picture of the transmons capacitor area. In c) the nano-string area is shown in closer detail. The 20 μm string has a designed equilibrium distance of $d_0 = 150$ nm to its ground plane. Panel d) shows one of the Josephson junctions in the SQUID loop, due to the underetching process used, part of the junction is free standing.

from interacting with each other through spatial separation. We thus want to discuss the merits of using a X-mon type qubit for our project.

From an equivalent circuit point of view the two designs differ little (cf. Fig. 5.6), since both qubit designs are based on non-linear oscillators. However, from a geometric design description the situation is more involved. In the case of a transmon qubit, as shown in Fig. 5.3, bulky capacitor plates make up most of the device capacitance. The capacitance of these plates is indicated as C_S in Fig. 5.6. The same capacitor plates are also part of the coupling capacitance C_g which couples the qubit structure to the resonator. This means, that by changing anything about the internal capacitance C_S , also the coupling capacitance C_g will change, as they are based on partially shared device parts. This effect does not only happen for this pair of capacitances. All connecting capacitances to the qubit, e.g. from antennas or resonators have, apart from the physical coupling as part of the overall capacitance C_Σ , also a geometric influence. This is the reason why the mapping of the parameter space is more involved for a transmon qubit, as many of the capacitors share device parts. In the case of the X-mon layout the geometry is more relaxed. As can be seen in Fig. 5.5, the coupling capacitance between the qubit and the readout resonator only attributes to the self capacitance of the X-mon (C_Σ) in a small area of one of the arms. The same is obviously true for all antennas or resonators connected to the different arms.

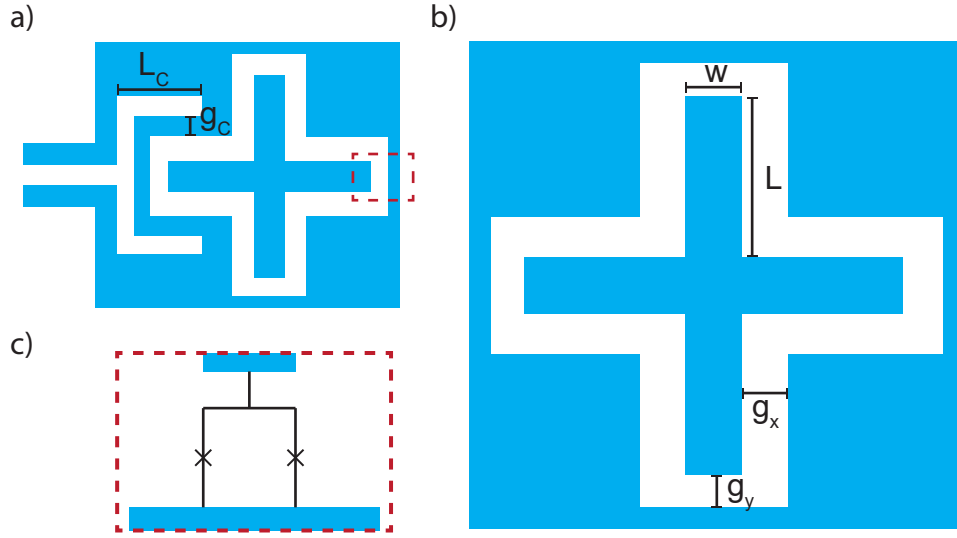


Figure 5.5: a) Schema showing the X-mon layout used, coupled to a readout resonator. Panel b) denominates the parameters used for the simulations. These are the width w and length L of the X-mon arms are changed. The self capacitance C_s depends mainly on the gaps to the ground plane g_x and g_y . Panel c) shows a zoom in into one of the arms, where a SQUID-loop shunts the capacitance to the groundplane.

This does not inherently change the physics connecting the single parameters, however it allows to decouple them geometrically. Thus, for the rest of the qubit, the capacitance can be changed rather freely without influencing C_g . This can be done by geometrical means, as the capacitance C_Σ is largely modulated by the gaps to the groundplane g_x and g_y (cf. Fig. 5.5). Note, that this requires all connected microwave resonators or antennas to have a voltage anti-node at the coupling capacitances they share with the X-mon at its arms. A further advantage of the X-mon is, that due to its shape, it is possible to spatially separate circuit parts coupled to the qubit. This way the SQUID-loop and a possible control line for the flux can be separated from the readout resonator. Also the rather sensitive Josephson junctions can be spatially separated from the fabrication intensive nano-string. Altogether, we can identify the following potential advantages for the implementation of a nano-string into a X-mon type qubit: i) Engineering the coupling and internal capacitances in the qubit and microwave resonator system can be done more easily. This is a consequence of the geometric layout of the X-mon, as the geometric dependences between the single capacitors is less distinctive. ii) The possibility to use different arms of the X-mon to couple to different resonators, antennas etc. suppresses the crosstalk among those circuit devices. Further, the number of arms can be scaled up for future endeavors, if more connections to other circuits are necessary. iii) By spatially separating the areas where Josephson junctions are present in the qubit layout from the areas where one or more nano-strings are located, it is easier to protect the junctions during the fabrication processes concerning the nano-strings. This presents the X-mon layout as advantageous for the implementation of one or several nano-strings as mechanically

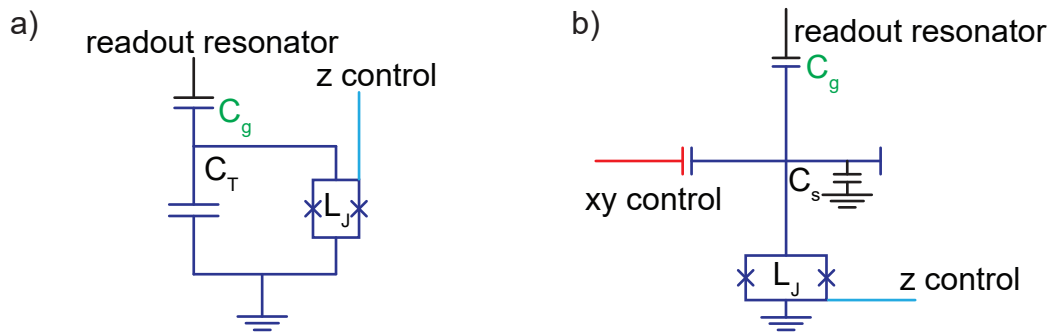


Figure 5.6: Comparison of the equivalent circuit diagrams for a transmon qubit a) and the X-mon geometry b). From an electrical circuit point of view the two designs are equivalent to each other, however the cross-correlations between single elements are different for the actual layouts. For more information please see the text.

compliant parts of a transmon qubit's capacitance, compared to the standard transmon layout [250].

5.4 Discussion and Outlook

In this part, we considered the engineering necessary to implement an Al nano-string resonator as a mechanically compliant element of a transmon qubit. We see this as a powerful platform to enable a three system hybrid device, for which rich physics were proposed by Abdi et al. in Ref. [248]. This hybrid device is comprised of a mechanical nano-string resonator, a transmon qubit and at least one coplanar waveguide resonator. We considered different second generation design approaches. One in which two different microwave resonators were used to address the still separated devices (qubit and nano-string). In the second approach, we considered the integration of a nano-string into a transmon qubit and engineering the layout of this intermediate device. To this end we also compared simulated values from a pre-study with actually measured values of the fabricated devices. From this we learned the limitations of using a traditional transmon layout for this purpose. We then discussed the possibility of using a X-mon type qubit layout for the purpose of integrating a nano-string as a mechanically compliant element. We come to the result, that the advantages of using such a layout are significant. Using a X-mon design should facilitate the device engineering. It allows for easier connections to other circuit devices and inherently simplifies the protection of Josephson junctions during subsequent fabrication processes. We therefore recommend looking into this system of a nano-string integrated in a X-mon qubit in greater detail.

DISCUSSION AND OUTLOOK

In this thesis, we investigated the coupling mechanisms of nanomechanical resonators to various experimental degrees of freedom. By using different coupling schemes, we formed hybrid systems. These hybrid systems were established by coupling nanomechanical string resonators to mechanical, magnetic and electric degrees of freedom. First, we introduced the workhorse of the thesis, a doubly clamped, tensile stressed nanomechanical string. We theoretically explored the models used to describe this system. We began with a homogeneous string in the linear regime and extended the model to multilayer strings and non-linear effects including an in-situ tuning mechanism for the mechanical resonance frequency. Then, we focused onto the hybrid systems originating from the different coupling mechanisms. In part 2, we discussed and investigated a nano-string network comprised of three nano-mechanical string resonators with independently tunable resonance frequencies, and comparable strong inter-resonator coupling. We explored the emergence of a mechanical dark state in the system, when all resonator frequencies are degenerate, corroborating this dark state using numerical calculations as this goes beyond analytic description. We investigated the dynamical evolution of the nano-string network by studying the excitation transfer inspired by Landau-Zener physics. We did this in the range still describable by analytic solutions as well as beyond them. This demonstrates control over the transfer dynamics in a nano-string resonator network, thus enabling controlled information exchange between the single resonators in the network. This shows, that nanomechanical string networks are an exquisite platform for realizing mechanical sensing applications and that they can be used for analog simulation purposes. Part 3, introduces a hybrid system consisting of a nanomechanical string resonator coupled to a magnetic degree of freedom. The coupling is facilitated by the magnetostriction of a CoFe alloy thin film on top of a nanomechanical string. We investigated the magnetostrictive constants of two low magnetic damping Co-Fe alloys grown within a specific layer stack [108]. The CoFe material system recently gained interest in the field of spintronics and was identified as a metallic magnetic system with ultra-low magnetic damping properties. One of the main questions is, whether the magnetoelastic properties are connected to the magnetization damping properties of the material, as for the case of the well known material system Permalloy (NiFe). Here, we were able to make progress on two paths. On one side, the fact, that the exceptional magnetic damping properties of CoFe only emerge in thin films and within

specific layer stacks, makes it a formidable challenge to extract the magnetoelastic properties for conventional sensing methods. We were able to overcome this challenge by using nanomechanical resonators and extract the magnetostrictive constant for the Co-Fe alloys. Our method allows the investigation of the magnetostrictive and elastic properties of thin film magnetic layers, even with small sample volumes and high aspect ratios. Both are requisites for future technical applications of spintronic devices including, in particular, magnetic sensing applications. On the other side, we found sizable magnetostriction in the Co-Fe alloys which excludes the absence of magnetostriction mediated magnon phonon coupling as origin of the low-damping properties. This is also a point where CoFe differs from the Permalloy material system, where the emergence of low magnetic damping was connected to the near-zero magnetostriction. We then gain further insight into the magnetomotive and magnetostrictive behavior of nanomechanical strings by focusing on the effects of electrical currents passing through a string in part 4. Here, we discussed the impacts of an electrical circuit in a metalized nano-string. By comparing a magnetomotive readout with non-invasive optical interferometry, we examine the effects of external as well as internal electrical currents on the nano-string's behavior. We do this both in the presence of an external magnetic field and the absence thereof. We find, that an additional external current can significantly influence both the frequency as well as the lineshape of the metalized string through heating and more involved electromagnetic interactions. We were able to quantitatively describe the change in lineshape and frequency due to electrical circuits. Apart from this, such a system might be used for future sensing applications, e.g. for high speed on-chip temperature measurements. In the last part 5, we considered a system, where a nanomechanical string resonator is coupled to a superconducting circuit qubit. This could result in a powerful platform to enable a three system hybrid device. The hybrid device is comprised of a mechanical nano-string resonator, a transmon qubit and at least one coplanar waveguide resonator at microwave frequencies. We discussed the system parameters for realizing ground state cooling and three partite entanglement and how they can be reached in experiment for real world device layouts. Using finite element simulations we simulated the device and compared the results to earlier experiments.

Within this thesis, we showed how nanomechanical strings can be used to extract the magnetostrictive properties of a material where the special magnetic properties are only apparent in thin films and within specific layer stacks, and which is therefore challenging for conventional measurement methods. With this we validated the use of nanomechanical string resonators for sensing applications using multilayer material systems. We investigated the impact of electrical currents onto the system of a nanomechanical string resonator and qualitatively described the effects of electrical currents on the frequency and lineshape of a nano-string. This can be seen as a suspended conductor, which is of interest for spintronic applications. We presented a network of mechanical strings and investigated the dynamical excitation transfer within it. Further, we generated a mechanical dark state in one of the modes of the network, which could be used for storage applications. We also discussed the integration of a nanomechanical string into a circuit qubit, considering the field of circuit quantum dynamics as a foundation for nanomechanical sensing and storage applications. We thus showed the large potential of nanomechanical string resonators in sensing applications by forming hybrid devices and the impact of environmental parameters onto nanomechanical string resonators uncovering novel aspects of their mechanical properties.

APPENDIX A

NANOMECHANICAL STRING RESONATORS

A.1 In situ frequency tuning mechanism - technical considerations

The frequency tuning technique presented in Sec. 1.3.3 can be seen complementary to the more commonly used tuning methods using electric fields [70, 73, 149, 209, 210] or a magnetomotive approach [260]. The discussed method completely eliminates the need for electric fields and thereby also the necessary corresponding local control gates, simplifying the system. However, the purely mechanical tuning mechanism also presents future challenges. Due to all frequencies being applied to the same global piezo-actuator, frequency crowding becomes an issue for networks with large resonator numbers. Furthermore the necessary high drive tone powers lead to heating in the actuator and thereby also the sample. This changes the sample temperature over the course of a measurement, which has influence on the material parameters. These challenges can be overcome, e.g. changing the nano-strings crosssections to shapes different from simple prismatic shape, will allow them to support more modes at different frequencies compensating the frequency crowding by spreading the control frequencies. By engineering the sample and sample holder (including the piezo-actuator) towards better heat management, the impact of the piezo heating can be reduced and maybe even suppressed.

APPENDIX B

NANOMECHANICAL RESONATOR NETWORKS

B.1 Optical interferometer

Figure B.1 shows a schematic of the optical interferometer used for measurements in Part 2. The red laser light 633nm from a DL Pro 633 made by Toptica is used. The beam first passes an optical bi-prism to roughly shape the beam profile, it is then coupled into a single mode optical fiber using a commercial microscope objective. After passing the fiber the beam is collimated and now has a circular spot and contains only one mode. A Glan-Thomson polarizer, in conjunction with a $\lambda/2$ -wave plate is used to smoothly set the laser power. A polarizing beam splitter separates the beam now in two arms, the sample arm and the reference arm. A $\lambda/2$ -wave plate in front of the beam splitter is used to set the splitting ratio. The beam passes two more beam splitters and changed to a circular polarization by a $\lambda/4$ -wave plate. It is then focussed onto the sample by a commercial microscope objective. The reflected beam passes back through the objective and $\lambda/4$ -wave plate and is then deflected by a polarizing beam splitter into another polarizing beam splitter where it is reunited with the reference arm. The reference arm starts at the same polarizing beam splitter. It then passes a second polarizing beam splitter and a $\lambda/4$ -wave plate, after which it is reflected by a piezo-controlled mirror. The reflected beam again passes the $\lambda/4$ -wave plate and is then deflected by the polarizing beam splitter onto another polarizing beam splitter where it is reunited with the sample arm. The laser beams from the sample and reference arms then pass a last $\lambda/2$ -wave plate and a polarizing beam splitter and the two resulting beams are focussed into the input ports of a split photo-detector. For a full description of the interferometer and it's working mechanisms please see [119]. An amplifier chain is used to amplify the voltage signal from the photo diode before analyzing it. Typically, the strings oop motion is small for thermal measurements and therefore a higher amplification of the signal is necessary. To reduce the added noise of the amplifiers and to cut of the amplification of higher harmonics in the voltage signal, lowpass filters were used in between amplification steps. Please note, that the frequency of the nano-strings needs to be taken into account when selecting the filter cut-off frequencies.

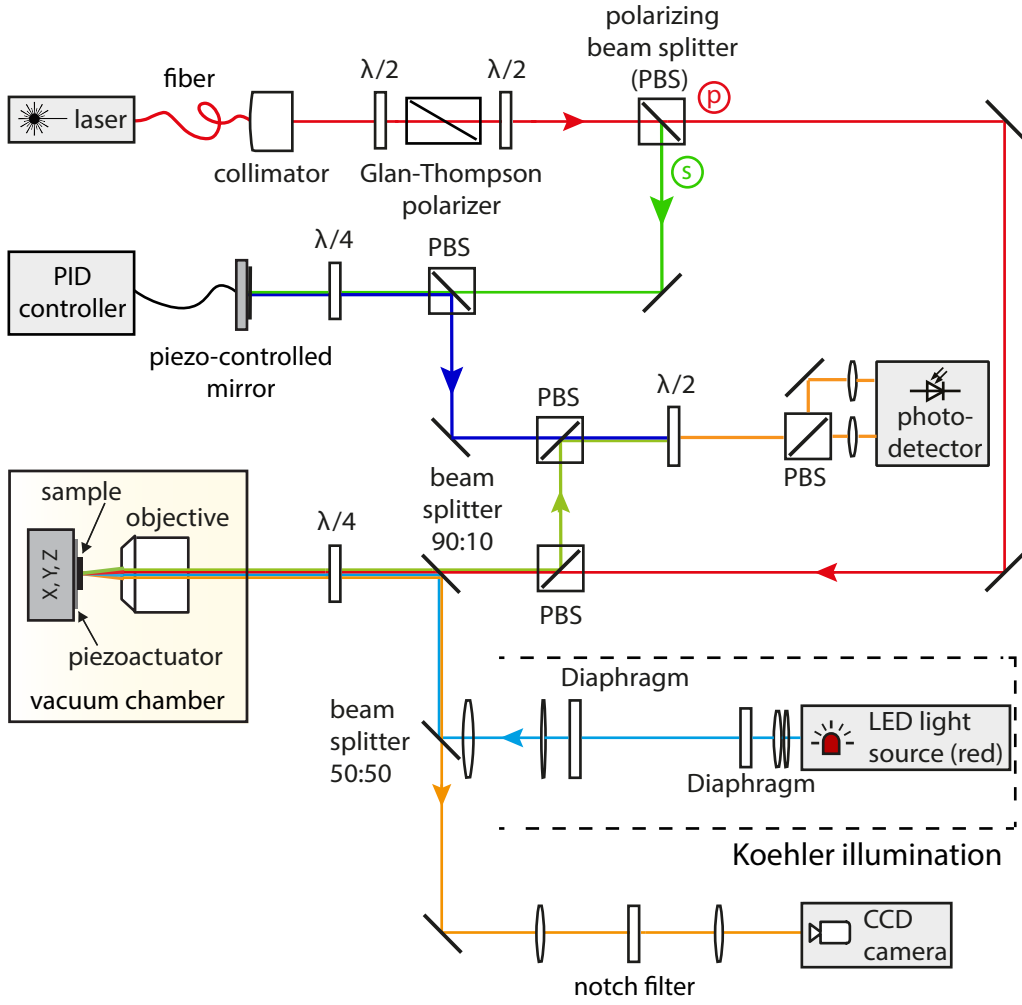


Figure B.1: Schematic of the optical interferometer used to measure the oscillatory motion of nano-strings in Part 2.

B.2 In line network dynamics

Additional parameters and measurement data for the population transition dynamics in the in-line network configuration.

	D	E	F
$\Omega^0/2\pi$	9.237 MHz	9.241 MHz	9.2385 MHz
$\Gamma/2\pi$	80(10) Hz	80(10) Hz	80(10) Hz

Table B.1: Eigenfrequencies of the undisturbed modes of the string resonators (D/E/F) in the and their linewidth (FWHM), for the *in-line* sample layout.

	$\delta\epsilon$	$\epsilon\varphi$	$\delta\varphi$
$g_{ij}/2\pi$	130 Hz	103.5 Hz	—

Table B.2: Inter mode coupling strengths for the in-line three resonator network, extracted from individual avoided crossing measurements

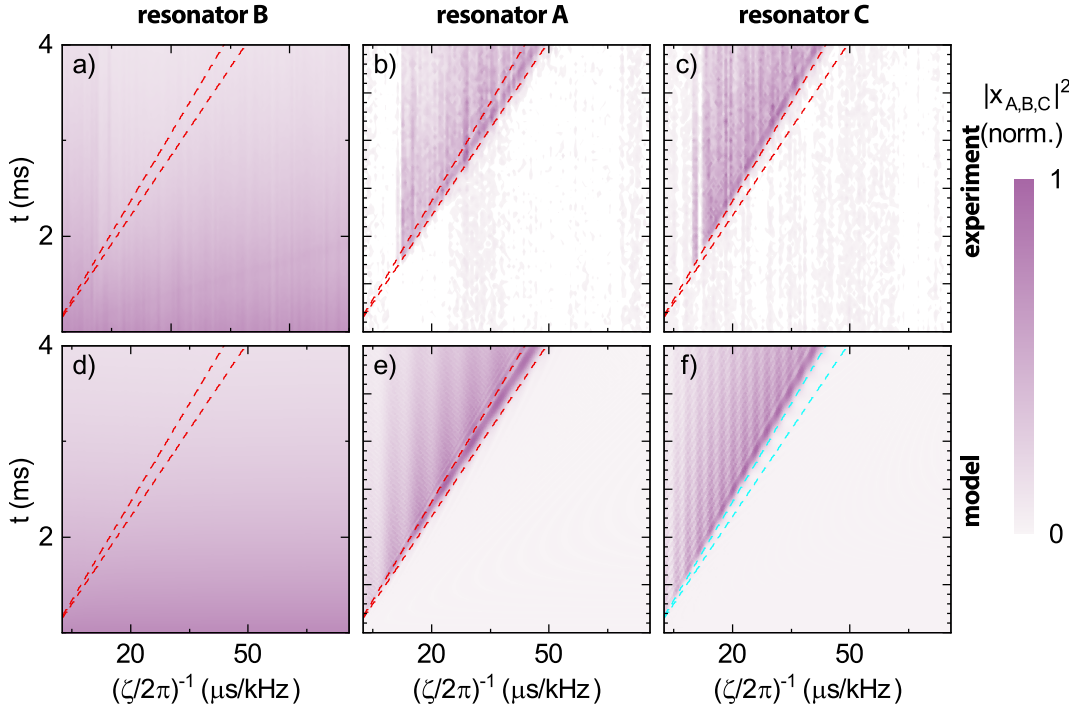


Figure B.2: Excitation of the single strings over the time of a Landau-Zener experiment for the in-line layout. The string network is set up to compare to the on-resonance configuration of the star-shaped layout. Panels (a-c) show the measurement data. And corresponding numerical simulation results are shown in panels (d-f). In both cases an initial pulse is used to excite mode δ . The resonance frequency of δ is then tuned, upwards through the resonance frequencies of the other modes (φ and ϵ) with varying tuning speeds (fast to slow). The dashed red lines are a guide to the eye to mark the times at which the mode frequency of δ matches the mode frequencies of φ (lower) and ϵ (upper) respectively. The measurement and model are shown for all read-out resonators (D,E,F) respectively. A high mechanical response of the measured string is depicted by dark color. Each row of the graph is normalized to the initial excitation pulse.

APPENDIX C

MAGNETOMECHANICAL AND MAGNETOMOTIVE HYBRID SYSTEMS

C.1 nano-stringfrequency buckling considerations using FEM simulations

We used a finite element simulation (COMSOL®) to simulate the eigenfrequency and mode-shape of a $L = 25 \mu\text{m}$ nano-string. For this simulation we used the geometry and material parameters of a nano-string with the same layout as shown in Fig. 3.4. We also assumed an average pre-stress of the string of 458 MPa, as obtained by our measurements 3.5. From this we find the first eigenfrequency to be $\Omega_{\text{simu}}/2\pi = 7.373 \text{ MHz}$ which is in good agreement with the measured value of 7.316 MHz shown in Fig. 3.7. The simulation also shows that this eigenfrequency has the mode-shape of a undisturbed out-of-plane oscillation. This mode-shape also persist for a large range of compressive stresses in the metal film, assuming a tensile pre-stress in the Si_3N_4 . Simulations show, that the mode shape only changes, once the compressive stress in the metal significantly exceeds the tensile pre-stress in the SiN. For a typical pre-stress of $\sigma_0 \approx 750 \text{ MPa}$ this happens if the compressive stress in the thin metal film reaches $\approx 3400 \text{ MPa}$. Which is not reachable in any way using the discussed material system and fabrication techniques.

C.2 Magnetization damping of CoFe stacks on SiN substrates measured using broadband magnetic resonance

To investigate the magnetization damping properties of the $\text{Co}_{25}\text{Fe}_{75}$ and $\text{Co}_{10}\text{Fe}_{90}$ alloys investigated in 3.5, we perform broadband ferromagnetic resonance measurements (bbFMR) on extended CoFe thin films on reference SiN substrates¹ at room temperature [261]. The

¹These measurements were carried out using extended thin films, as the filling factor for structured nano-string samples is to low to technically resolve with the used measurement technique

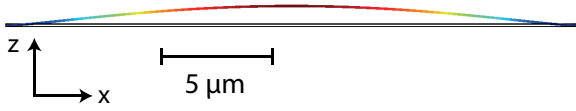


Figure C.1: Result of a numeric finite element simulation of the eigenfrequency and mode shape of a $L = 25 \mu\text{m}$ nano-string, alike to what is shown in Fig. 3.4. Using the same material and geometry parameters as in the experiment, as well as the experimentally obtained pre-stress ($\sigma_0 = 458 \text{ MPa}$), the resonance frequency and mode shape were simulated. Giving a resonance frequency of $\Omega_{simu} = 7.373 \text{ MHz}$ and the mode-shape of an undisturbed oop oscillation.

continuous CoFe films were grown on Si_3N_4 (SiN) in the same process as the string samples investigated in 3.5 by the group of Justin Shaw. The bbFMR measurements were performed as described in Ref. [261,262]. The measurements and following analysis of the data were carried out by Lukas Liensberger. For the bbFMR, the CoFe layer faced the center conductor of the coplanar waveguide (center conductor width $\approx 250 \mu\text{m}$), which was located between the pole pieces of an electromagnet. A static magnetic field of $|\mu_0 H_0| \leq 3 \text{ T}$ was applied parallel (ip) and perpendicular (oop) to the sample surface depending on the investigated effect. FMR spectra were acquired for various microwave frequencies $f \leq 43.5 \text{ GHz}$ using a microwave diode detection scheme including a lock-in amplifier and microwave frequency modulation (c.f. Fig. C.2a)). In a first step, we fit the FMR data (an example is shown in Fig. C.2b)) to a Lorentzian lineshape to extract the resonance magnetic field H_{res} and linewidth ΔH for each frequency f . Fitting the resonance magnetic field H_{res} vs. frequency f (see Fig. C.2 c)/e) to [261]

$$f(H_{\text{res}}^{\text{ip}}) = \frac{|\gamma|}{2\pi} \mu_0 \sqrt{(H_{\text{res}} + H_{\text{aniso}})(H_{\text{res}} + H_{\text{aniso}} + M_{\text{eff}})}, \quad (\text{C.1})$$

and

$$f(H_{\text{res}}^{\text{oop}}) = \frac{|\gamma|}{2\pi} \mu_0 \cdot (H_{\text{res}} - M_{\text{eff}}), \quad (\text{C.2})$$

for ip and oop data, respectively, yields the effective magnetization M_{eff} , the in-plane anisotropy H_{aniso} and the gyromagnetic ratio $\gamma = g\mu_B/\hbar$. The Gilbert damping was extracted from the linewidth over frequency data (c.f. Fig. C.2 d)/f) using [261]

$$\mu_0 \Delta H = \mu_0 \Delta H_0 + \frac{4\pi\alpha f}{|\gamma|}. \quad (\text{C.3})$$

The extracted fit values are listed in Tab. C.1. All values are in good agreement with the values measured by Schoen et al. [108]. From this we conclude that using SiN as a substrate does not change the low damping behavior of the CoFe stack. Note that the extracted α values for the oop field geometry are expected to be better than for the ip geometry, as the oop configuration suppresses the two-magnon scattering process.

C.3 Optical and electrical measurement setups

In this section, we give a more detailed description of the measurement setups used in parts 3 and 4. Expanding on the measurement setup descriptions in 3.4.1 and 4.4.1.

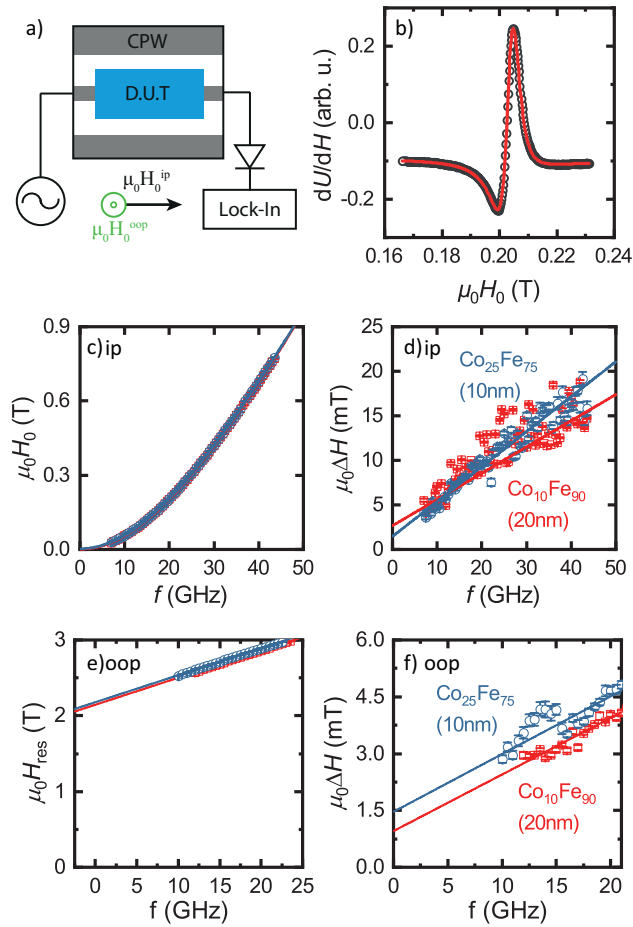


Figure C.2: a) Sketch of the FMR measurement setup: The sample is positioned on the center conductor of a coplanar waveguide (CPW) with the CoFe facing the CPW. The CPW is connected to a microwave source on one side and to a microwave diode and a lock-in amplifier at the other. An external magnetic field is applied c),d) in-plane or e),f) out-of-plane. b) Exemplary field-swept FMR measurement at $f = 20$ GHz for $\text{Co}_{10}\text{Fe}_{90}$ with the external field applied in-plane. Frequency dependence of the ip (oop) resonance field H_{res} c)(e) and full width at half maximum ΔH d)(f) of the FMR spectra obtained from 20 nm $\text{Co}_{10}\text{Fe}_{90}$ (red) and 10 nm $\text{Co}_{25}\text{Fe}_{75}$ (blue) grown on top of a Si_3N_4 substrate. The solid lines are fits to the data.

Optical interferometer for magnetomechanic measurements

The optical interferometer used for magnetomechanical as well as magnetomotive experiments can be separated into three parts. The first part is the laser source (a diode laser with a wavelength of 633 nm), with optical filters and a lens array used to couple to a single mode fibre. The fibre then connects this to the actual interferometer. This way the laser source can be exchanged flexible and the actual interferometer gains portability. The main part of the interferometer consists of two parts, one housing the majority of the optical setup and one housing the sample stage. The sample container is fashioned in a brass tube, which can be inserted between the pole-shoes of several electromagnets at the WMI, and can be evacuated to suppress air damping of the nano-strings. For this

Table C.1: List of the fit values extracted from broadband magnetic resonance measurements shown in Fig. C.2.

	$\mu_0 M_{\text{eff}}$ (T)	g	$\mu_0 \Delta H$ (mT)	α (10^{-3})
Co ₁₀ Fe ₉₀ (ip)	2.12 ± 0.01	2.08 ± 0.01	2.6 ± 0.3	4.2 ± 0.2
Co ₂₅ Fe ₇₅ (ip)	2.16 ± 0.01	2.06 ± 0.01	1.4 ± 0.2	5.6 ± 0.2
Co ₁₀ Fe ₉₀ (oop)	2.14 ± 0.01	2.00 ± 0.01	0.95 ± 0.2	2.0 ± 0.1
Co ₂₅ Fe ₇₅ (oop)	2.17 ± 0.01	2.00 ± 0.01	1.4 ± 0.2	2.1 ± 0.1
	$\mu_0 H_{\text{aniso}}$ (mT)			
Co ₁₀ Fe ₉₀ (ip)	-0.8 ± 0.1			
Co ₂₅ Fe ₇₅ (ip)	-3 ± 0.1			

very reason, large efforts were made when constructing and upgrading this part, that no magnetic materials were used. This was done to suppress any motion or deflection of the interferometer parts due to magnetic interactions, which could lead to misalignments of the optical path. The main interferometer is designed in four optical stages. In the uppermost stage, the laser is coupled from the fibre into a free space setup, also the light of a red (635 nm) LED is coupled into the optical path. The laser then passes through the second and third stage, into the fourth stage where it is guided into and through the vacuum tube onto the sample stage, where it is focussed with a special microscope objective housed in a German silver casing. The reflected laserbeam, which interfered with the sample the same way as already described in 2.4.1, carries information on the center of mass motion of the observed string. The reflected beam passes back through the fourth stage, while passing the third stage a small percentage of 2% is guided into a camera, giving optical access to the sample and laser-spot. The main part of the reflected beam is then guided through stage two onto a photo-diode, where the intensity of the reflected light is converted into a voltage. A picture as well as the schematic of the whole setup can be seen in Fig. C.3

Optical measurement

We detect the frequency dependent displacement response of a nano-string to a stimulus using a vector network analyzer (VNA). For this, we use the VNA to send an excitation signal to the piezo-actuator at the sample. To remain in the linear response regime of the nano-string, we choose an appropriately small excitation amplitude (cf. 1.3.2). We then analyze the reflected laser light by comparing the voltage signal of the photo-diode to the excitation signal using the VNA. For the optical interferometric measurements, the voltage signal from the photo-detector is amplified before analyzing it. To this end, an amplifier chain is used. Two low-noise-high-gain amplifiers with a total amplification of 20 – 60 dB are used. In front of both amplifiers, low-pass filters, suited for the mechanical frequencies of interest, are added to suppress high frequency noise of the amplifiers.

Electrical measurements

To investigate the impact of an electrical current onto the system of a (magnetic) metallized nano-string we use the measurement setup described in 4.4.1. For this, electrical connections onto the optically investigated strings were made via Al wire bonding. The

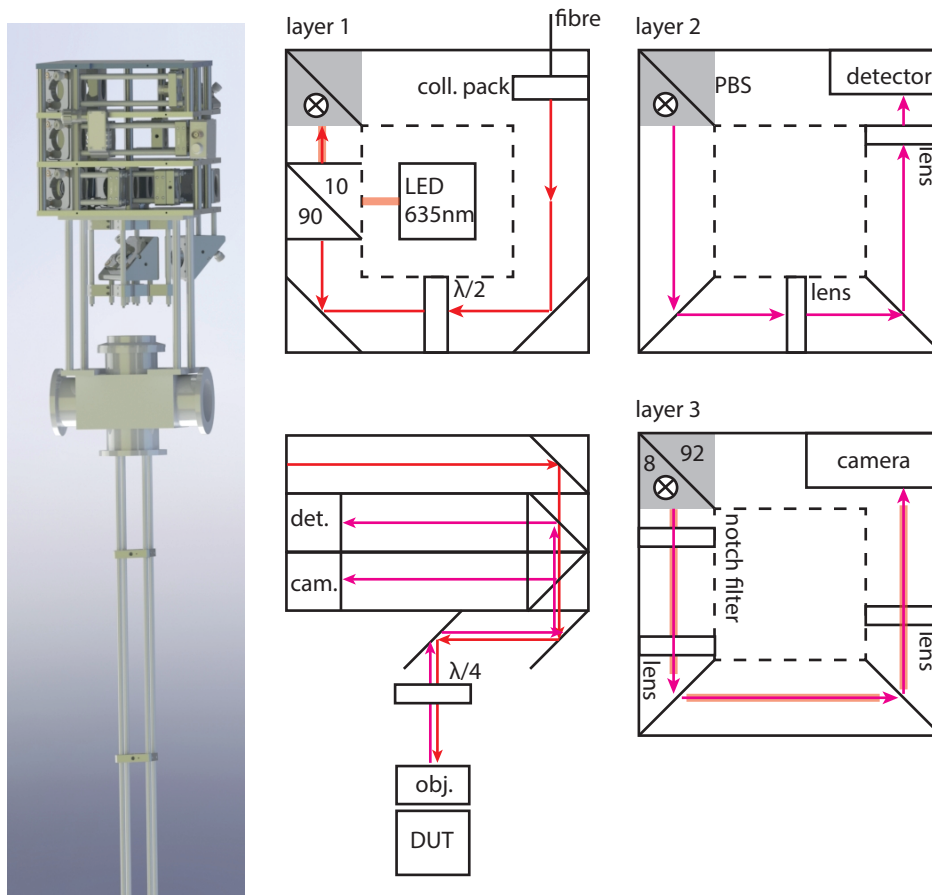


Figure C.3: Rendered graphic of the overall interferometer and detailed schematic of the interferometer head. The off-site laser source is connected to the interferometer via a single mode fibre. In the top layer (1) the laser beam is coupled into the interferometer, and the light from a red LED source is added to the optical path. The light then passes through the next two layers (2 and 3) via a polarizing beam splitter and a 92/8 beam splitter. It is then guided through the vacuum chamber onto a microscope objective and focussed onto the string. The reflected light is guided to a camera for optical access on one side (8%) and to a photo-diode on the other (92%).

wire bonds connect the clamping pads of the single strings with electrodes on the sample carrier. From there on, wires connect the sample stage through the vacuum chamber of the optical interferometer to a break-out box outside the vacuum enclosure. By connecting the lock-in amplifier to the single channels of the break-out box, we can perform 4-wire resistance measurements of the single strings as well as send external electrical currents through the string. For this specific purpose, a 1 M Ω resistor is used between the output port of the lock-in and the break-out box. As the metallized nano-strings resemble safety fuses, great care needs to be taken to limit the voltage/currents across the strings to prevent destroying them. To gain insight into the temperature at the sample stage, a pt100 temperature sensor is soldered onto the sample carrier PCB, further also a 10 Ω resistor is present, to allow heating the whole sample carrier. This combination of temperature

sensor and heater was used to stabilize the sample environment temperature. This is especially necessary when changing the external magnetic field, as the electromagnet changes temperature by several degrees depending on the applied magnetic field.

BIBLIOGRAPHY

- [1] M. Denny, *European Journal of Physics* **23**, 449 (2002).
- [2] H. Feldmann, *Laryngo-Rhino-Otologie* **76**, 116 (1997).
- [3] S. M. Curry, *American Journal of Physics* **44**, 924 (1976).
- [4] M. Lepidi, V. Gattulli, and D. Foti, *Engineering Structures* **31**, 1486 (2009).
- [5] G. Arioli and F. Gazzola, *Communications in Nonlinear Science and Numerical Simulation* **42**, 342 (2017).
- [6] A. C. Davies, *Annals of Science* **35**, 509 (1978).
- [7] R. Doll and M. NÃ¶bauer, *Physical Review Letters* **7**, 51 (1961).
- [8] A. Einstein, *Die Naturwissenschaften* **3**, 237 (1915).
- [9] A. Einstein and W. De Haas, *Proc. KNAW*, vol. 181, 696 (1915).
- [10] J. W. Judy, *Smart Materials and Structures* **10**, 1115 (2001).
- [11] M. Gad-el Hak, *The MEMS handbook* (CRC Press, Boca Raton, FL, 2002).
- [12] P. Rai-Choudhury, *Handbook of Microlithography, Micromachining, and Microfabrication. Volume 1: Microlithography* (SPIE PRESS, 1997).
- [13] N. P. Mahalik, *Micromanufacturing and Nanotechnology* (Springer-Verlag GmbH, 2005).
- [14] G. Wiederrecht, editor, *Handbook of Nanofabrication* (ACADEMIC PR INC, 2009).
- [15] Y. Qin, *Micro-manufacturing engineering and technology* (Elsevier, Amsterdam Boston, 2010).
- [16] C.-M. Ho and Y.-C. Tai, *Annual Review of Fluid Mechanics* **30**, 579 (1998).
- [17] G. Rebeiz and J. Muldavin, *IEEE Microwave Magazine* **2**, 59 (2001).
- [18] D. Eddy and D. Sparks, *Proceedings of the IEEE* **86**, 1747 (1998).

- [19] R. Verma, B. P. Gogoi, and D. Mladenovic, SAE transactions 181–188 (2003).
- [20] C. Acar, A. R. Schofield, A. A. Trusov, L. E. Costlow, and A. M. Shkel, IEEE Sensors Journal **9**, 1895 (2009).
- [21] M. Kraft, *MEMS for automotive and aerospace applications* (Woodhead Pub, Oxford Philadelphia, 2013).
- [22] S. Finkbeiner, *2013 Proceedings of the ESSCIRC (ESSCIRC)*, 9–14 (IEEE, 2013).
- [23] S. Bhattacharya, A. K. Agarwal, O. Prakash, and S. Singh, editors, *Sensors for Automotive and Aerospace Applications* (Springer-Verlag GmbH, 2018).
- [24] J. C. Eloy and E. Mounier, *MEMS/MOEMS Components and Their Applications II*, edited by A. K. Henning (SPIE, 2005).
- [25] S. Nihtianov, *Smart sensors and MEMS : intelligent devices and microsystems for industrial applications* (Woodhead Publishing, Duxford, 2018).
- [26] F. Khoshnoud and C. W. de Silva, IEEE Instrumentation & Measurement Magazine **15**, 14 (2012).
- [27] G. Lammel, *2015 28th IEEE International Conference on Micro Electro Mechanical Systems (MEMS)* (IEEE, 2015).
- [28] P. Muhammad and S. A. Devi, Procedia Computer Science **93**, 940 (2016).
- [29] J. P. Sanjurjo, E. Prefasi, C. Buffa, and R. Gaggl, Sensors **17**, 1312 (2017).
- [30] G. Binnig and H. Rohrer, Scientific American **253**, 50 (1985).
- [31] G. Binnig, C. F. Quate, and C. Gerber, Physical Review Letters **56**, 930 (1986).
- [32] C. Gerber, G. Binnig, H. Fechs, O. Marti, and H. Rohrer, *Scanning Tunneling Microscopy*, 79–82 (Springer Netherlands, 1986).
- [33] Y. Martin, D. W. Abraham, and H. K. Wickramasinghe, Applied Physics Letters **52**, 1103 (1988).
- [34] C. L. Degen, M. Poggio, H. J. Mamin, C. T. Rettner, and D. Rugar, Proceedings of the National Academy of Sciences **106**, 1313 (2009).
- [35] A. Boisen, S. Dohn, S. S. Keller, S. Schmid, and M. Tenje, Reports on Progress in Physics **74**, 036101 (2011).
- [36] A. C. Bleszynski-Jayich, W. E. Shanks, B. Peaudecerf, E. Ginossar, F. von Oppen, L. Glazman, and J. G. E. Harris, Science **326**, 272 (2009).
- [37] U. Mohideen and A. Roy, Physical Review Letters **81**, 4549 (1998).
- [38] H. B. Chan, Science **291**, 1941 (2001).
- [39] D. Rugar, R. Budakian, H. J. Mamin, and B. W. Chui, Nature **430**, 329 (2004).

- [40] S. Kolkowitz, A. C. B. Jayich, Q. P. Unterreithmeier, S. D. Bennett, P. Rabl, J. G. E. Harris, and M. D. Lukin, *Science* **335**, 1603 (2012).
- [41] M. D. LaHaye, J. Suh, P. M. Echternach, K. C. Schwab, and M. L. Roukes, *Nature* **459**, 960 (2009).
- [42] H. G. Craighead, *Science* **290**, 1532 (2000).
- [43] M. Roukes, *Physics World* **14**, 25 (2001).
- [44] K. Ekinici, *Small* **1**, 786 (2005).
- [45] M. Li, H. X. Tang, and M. L. Roukes, *Nature Nanotechnology* **2**, 114 (2007).
- [46] T. D. Stowe, K. Yasumura, T. W. Kenny, D. Botkin, K. Wago, and D. Rugar, *Applied Physics Letters* **71**, 288 (1997).
- [47] E. Gavartin, P. Verlot, and T. J. Kippenberg, *Nature Nanotechnology* **7**, 509 (2012).
- [48] H. J. Mamin and D. Rugar, *Applied Physics Letters* **79**, 3358 (2001).
- [49] J. Moser, J. Güttinger, A. Eichler, M. J. Esplandiu, D. E. Liu, M. I. Dykman, and A. Bachtold, *Nature Nanotechnology* **8**, 493 (2013).
- [50] S. Stapfner, L. Ost, D. Hunger, J. Reichel, I. Favero, and E. M. Weig, *Applied Physics Letters* **102**, 151910 (2013).
- [51] J. Chaste, A. Eichler, J. Moser, G. Ceballos, R. Rurali, and A. Bachtold, *Nature nanotechnology* **7**, 301 (2012).
- [52] R. Budakian, H. J. Mamin, and D. Rugar, *Applied Physics Letters* **89**, 113113 (2006).
- [53] R. Mukhopadhyay, M. Lorentzen, J. Kjems, and F. Besenbacher, *Langmuir* **21**, 8400 (2005).
- [54] J. Arlett, E. Myers, and M. Roukes, *Nature Nanotechnology* **6**, 203 (2011).
- [55] K. Eom, H. S. Park, D. S. Yoon, and T. Kwon, *Physics Reports* **503**, 115 (2011).
- [56] M. R. Paul, M. T. Clark, and M. C. Cross, *Nanotechnology* **17**, 4502 (2006).
- [57] T. Y. Kwon, K. Eom, J. H. Park, D. S. Yoon, T. S. Kim, and H. L. Lee, *Applied Physics Letters* **90**, 223903 (2007).
- [58] P. W. Snyder, G. Lee, P. E. Marszalek, R. L. Clark, and E. J. Toone, *Proceedings of the National Academy of Sciences* **104**, 2579 (2007).
- [59] J. Tamayo, M. Calleja, D. Ramos, and J. Mertens, *Physical Review B* **76** (2007).
- [60] E. M. Puchner and H. E. Gaub, *Current Opinion in Structural Biology* **19**, 605 (2009).
- [61] B. Ilic, Y. Yang, K. Aubin, R. Reichenbach, S. Krylov, and H. G. Craighead, *Nano Letters* **5**, 925 (2005).

- [62] M. Spletzer, A. Raman, A. Q. Wu, X. Xu, and R. Reifenberger, *Applied Physics Letters* **88**, 254102 (2006).
- [63] K. Jensen, K. Kim, and A. Zettl, *Nature Nanotechnology* **3**, 533 (2008).
- [64] P. A. Greaney and J. C. Grossman, *Nano Letters* **8**, 2648 (2008).
- [65] A. K. Naik, M. S. Hanay, W. K. Hiebert, X. L. Feng, and M. L. Roukes, *Nature Nanotechnology* **4**, 445 (2009).
- [66] J. F. Davis, M. Bronikowski, D. Choi, L. Epp, M. Hoenk, D. Hoppe, B. Kowalczyk, F. Noca, E. Wong, B. Hunt, B. Chang, M. Jouzi, M. Tzolov, A. Yin, J. Xu, J. D. Adam, R. M. Young, J. Adams, and B. Rogers, *2003 Third IEEE Conference on Nanotechnology, 2003. IEEE-NANO 2003.*, vol. 2, 635–638 vol. 2.
- [67] M. Sato, B. E. Hubbard, A. J. Sievers, B. Ilic, D. A. Czaplewski, and H. G. Craighead, *Physical Review Letters* **90**, 044102 (2003).
- [68] S.-B. Shim, M. Imboden, and P. Mohanty, *Science* **316**, 95 (2007).
- [69] T. S. Biswas, J. Xu, X. Rojas, C. Doolin, A. Suhel, K. S. D. Beach, and J. P. Davis, *Nano Lett.* **14**, 2541 (2014).
- [70] K. Gajo, S. Schüz, and E. M. Weig, *Appl. Phys. Lett.* **111**, 133109 (2017).
- [71] M. Pernpeintner, P. Schmidt, D. Schwienbacher, R. Gross, and H. Huebl, *Physical Review Applied* **10**, 034007 (2018).
- [72] J. Doster, S. Hoenl, H. Lorenz, P. Paulitschke, and E. M. Weig, *Nature Communications* **10**, 5246 (2019).
- [73] T. Faust, J. Rieger, M. J. Seitner, J. P. Kotthaus, and E. M. Weig, *Nature Physics* **9**, 485 (2013).
- [74] M. J. Seitner, H. Ribeiro, J. Kölbl, T. Faust, J. P. Kotthaus, and E. M. Weig, *Physical Review B* **94**, 245406 (2016).
- [75] O. M. Aldossary and V. E. Lembessis, *J. Phys. B: At. Mol. Opt. Phys.* **45**, 115502 (2012).
- [76] S. C. Masmanidis, H. X. Tang, E. B. Myers, M. Li, K. D. Greve, G. Vermeulen, W. V. Roy, and M. L. Roukes, *Physical Review Letters* **95**, 187206 (2005).
- [77] N. A. Spaldin and M. Fiebig, *Science* **309**, 391 (2005).
- [78] R. B. Karabalin, L. G. Villanueva, M. H. Matheny, J. E. Sader, and M. L. Roukes, *Physical Review Letters* **108**, 236101 (2012).
- [79] M. Pernpeintner, R. B. Holländer, M. J. Seitner, E. M. Weig, R. Gross, S. T. B. Goennenwein, and H. Huebl, *Journal of Applied Physics* **119**, 093901 (2016).
- [80] D. Schwienbacher, M. Pernpeintner, L. Liensberger, E. R. J. Edwards, H. T. Nembach, J. M. Shaw, M. Weiler, R. Gross, and H. Huebl, *Journal of Applied Physics* **126**, 103902 (2019).

- [81] D. S. Greywall, B. Yurke, P. A. Busch, A. N. Pargellis, and R. L. Willett, *Physical Review Letters* **72**, 2992 (1994).
- [82] D. S. Greywall, B. Yurke, P. A. Busch, and S. C. Arney, *Europhysics Letters (EPL)* **34**, 37 (1996).
- [83] A. N. Cleland and M. L. Roukes, *Appl. Phys. Lett.* **69**, 2653 (1996).
- [84] A. N. Cleland and M. L. Roukes, *Nature* **392**, 160 (1998).
- [85] K. L. Ekinci, Y. T. Yang, X. M. H. Huang, and M. L. Roukes, *Applied Physics Letters* **81**, 2253 (2002).
- [86] X. M. H. Huang, C. A. Zorman, M. Mehregany, and M. L. Roukes, *Nature* **421**, 496 (2003).
- [87] X. M. H. Huang, M. Manolidis, S. C. Jun, and J. Hone, *Applied Physics Letters* **86**, 143104 (2005).
- [88] W. J. Venstra and H. S. J. van der Zant, *Applied Physics Letters* **93**, 234106 (2008).
- [89] W. J. Venstra, H. J. R. Westra, K. B. Gavan, and H. S. J. van der Zant, *Applied Physics Letters* **95**, 263103 (2009).
- [90] K. C. Schwab and M. L. Roukes, *Physics Today* **58**, 36 (2005).
- [91] C. A. Regal, J. D. Teufel, and K. W. Lehnert, *Nature Physics* **4**, 555 (2008).
- [92] J. D. Teufel, J. W. Harlow, C. A. Regal, and K. W. Lehnert, *Physical Review Letters* **101**, 197203 (2008).
- [93] M. D. LaHaye, *Science* **304**, 74 (2004).
- [94] A. D. O'Connell, M. Hofheinz, M. Ansmann, R. C. Bialczak, M. Lenander, E. Lucero, M. Neeley, D. Sank, H. Wang, M. Weides, J. Wenner, J. M. Martinis, and A. N. Cleland, *Nature* **464**, 697 (2010).
- [95] T. Rocheleau, T. Ndukum, C. Macklin, J. B. Hertzberg, A. A. Clerk, and K. C. Schwab, *Nature* **463**, 72 (2009).
- [96] J. D. Teufel, T. Donner, D. Li, J. W. Harlow, M. S. Allman, K. Cicak, A. J. Sirois, J. D. Whittaker, K. W. Lehnert, and R. W. Simmonds, *Nature* **475**, 359 (2011).
- [97] E. E. Wollman, C. U. Lei, A. J. Weinstein, J. Suh, A. Kronwald, F. Marquardt, A. A. Clerk, and K. C. Schwab, *Science* **349**, 952 (2015).
- [98] M. Poot, S. Etaki, I. Mahboob, K. Onomitsu, H. Yamaguchi, Y. M. Blanter, and H. S. J. van der Zant, *Physical Review Letters* **105** (2010).
- [99] O. Shevchuk, G. A. Steele, and Y. M. Blanter, *Physical Review B* **96** (2017).
- [100] I. C. Rodrigues, D. Bothner, and G. A. Steele, *Nature Communications* **10** (2019).
- [101] P. Schmidt, M. T. Amawi, S. Pogorzalek, F. Deppe, A. Marx, R. Gross, and H. Huebl, *Communications Physics* **3** (2020).

- [102] J. D. Teufel, D. Li, M. S. Allman, K. Cicak, A. J. Sirois, J. D. Whittaker, and R. W. Simmonds, *Nature* **471**, 204 (2011).
- [103] V. Singh, S. J. Bosman, B. H. Schneider, Y. M. Blanter, A. Castellanos-Gomez, and G. A. Steele, *Nature Nanotechnology* **9**, 820 (2014).
- [104] T. A. Palomaki, J. W. Harlow, J. D. Teufel, R. W. Simmonds, and K. W. Lehnert, *Nature* **495**, 210 (2013).
- [105] A. P. Reed, K. H. Mayer, J. D. Teufel, L. D. Burkhardt, W. Pfaff, M. Reagor, L. Sletten, X. Ma, R. J. Schoelkopf, E. Knill, and K. W. Lehnert, *Nature Physics* **13**, 1163 (2017).
- [106] J.-M. Pirkkalainen, S. U. Cho, J. Li, G. S. Paraoanu, P. J. Hakonen, and M. A. Sillanpää, *Nature* **494**, 211 (2013).
- [107] M. Kounalakis, Y. M. Blanter, and G. A. Steele, *Physical Review Research* **2**, 023335 (2020).
- [108] M. A. W. Schoen, D. Thonig, M. L. Schneider, T. J. Silva, H. T. Nembach, O. Eriksson, O. Karis, and J. M. Shaw, *Nat Phys* **12**, 839 (2016).
- [109] A. N. Cleland, *Foundations of nanomechanics: from solid-state theory to device applications* (Springer Berlin Heidelberg, 2003).
- [110] S. Schmid, L. G. Villanueva, and M. L. Roukes, *Fundamentals of Nanomechanical Resonators* (Springer International Publishing, 2016).
- [111] S. Timoshenko, W. Weaver, and D. Young, *Vibration Problems in Engineering* (John Wiley and Sons: New York, 1990 5th ed.).
- [112] J. Gere, *Mechanics of materials* (Chapman and Hall, City, 1991).
- [113] R. Gross and A. Marx, *Festkörperphysik* (De Gruyter Oldenbourg, 2012).
- [114] W. Demtröder, *Experimentalphysik 1 : Mechanik und Wärme* (Springer Berlin Heidelberg, Berlin, Heidelberg, 2018).
- [115] S. S. Verbridge, J. M. Parpia, R. B. Reichenbach, L. M. Bellan, and H. G. Craighead, *Journal of Applied Physics* **99**, 124304 (2006).
- [116] Q. P. Unterreithmeier, *Gradient field transduction of nanomechanical resonators*, Ph.D. thesis, Ludwig-Maximilians-Universität München (2010).
- [117] L. Boltzmann, *Wiener Berichte* (1871).
- [118] A. Nayfeh, *Nonlinear oscillations* (Wiley, New York, 1979).
- [119] A. Faltermeier, *Umbau eines Freistrahlint interferometers zur Charakterisierung nanomechanischer Saiten*, Bachelor's thesis, Technical University of Munich (2017).
- [120] Y. T. Yang, C. Callegari, X. L. Feng, K. L. Ekinici, and M. L. Roukes, *Nano Letters* **6**, 583 (2006).

- [121] B. Lassagne, D. Garcia-Sanchez, A. Aguasca, and A. Bachtold, *Nano Letters* **8**, 3735 (2008).
- [122] Y. Tsaturyan, A. Barg, E. S. Polzik, and A. Schliesser, *Nature Nanotechnology* **12**, 776 (2017).
- [123] A. H. Ghadimi, S. A. Fedorov, N. J. Engelsen, M. J. Beryehi, R. Schilling, D. J. Wilson, and T. J. Kippenberg, *Science* **360**, 764 (2018).
- [124] J. Davis, D. Vick, D. Fortin, J. Burgess, W. Hiebert, and M. Freeman, *Applied Physics Letters* **96**, 072513 (2010).
- [125] F. Hocke, X. Zhou, A. Schliesser, T. J. Kippenberg, H. Huebl, and R. Gross, *New Journal of Physics* **14**, 123037 (2012).
- [126] X. Zhou, F. Hocke, A. Schliesser, A. Marx, H. Huebl, R. Gross, and T. J. Kippenberg, *Nature Physics* **9**, 179 (2013).
- [127] H. Okamoto, A. Gourgout, C.-Y. Chang, K. Onomitsu, I. Mahboob, E. Y. Chang, and H. Yamaguchi, *Nature Physics* **9**, 480 (2013).
- [128] L. Novotny, *American Journal of Physics* **78**, 1199 (2010).
- [129] D. Dragoman, *Quantum-Classical Analogies* (Springer Berlin Heidelberg, Berlin, Heidelberg, 2004).
- [130] S. Rips and M. J. Hartmann, *Physical Review Letters* **110**, 120503 (2013).
- [131] D. Hatanaka, I. Mahboob, K. Onomitsu, and H. Yamaguchi, *Applied Physics Letters* **102**, 213102 (2013).
- [132] I. Mahboob, M. Mounaix, K. Nishiguchi, A. Fujiwara, and H. Yamaguchi, *Scientific Reports* **4**, 4448 (2014).
- [133] M. Pechal, P. Arrangoiz-Arriola, and A. H. Safavi-Naeini, *Quantum Science and Technology* **4**, 015006 (2018).
- [134] T. Faust, J. Rieger, M. J. Seitner, P. Krenn, J. P. Kotthaus, and E. M. Weig, *Physical Review Letters* **109**, 037205 (2012).
- [135] T. Luschmann, *Coupling Strings, String Networks and Magnon-Phonon Interaction*, Master's thesis, Technical University of Munich (2018).
- [136] D. Schwienbacher, T. Luschmann, R. Gross, and H. Huebl, arXiv:2011.08080 [cond-mat.mes-hall] .
- [137] L. D. Landau, *Z. Sowjetunion* **2**, 46 (1932).
- [138] C. Zener, *Proceedings of the Royal Society of London. Series A, Containing Papers of a Mathematical and Physical Character* **137**, 696 (1932).
- [139] C. E. Carroll and F. T. Hioe, *Journal of Physics A: Mathematical and General* **19**, 1151 (1986).

- [140] S. Brundobler and V. Elser, *Journal of Physics A: Mathematical and General* **26**, 1211 (1993).
- [141] B. Militello, *Phys Rev A* **99**, 033415 (2019).
- [142] J. Marion, *Classical dynamics of particles and systems* (Academic Press, New York, 1965).
- [143] G. Strang, *Introduction to Linear Algebra* (Cambridge University Pr., 2016).
- [144] M. Pernpeintner, *Nanomechanical Hybrid Systems*, Ph.D. thesis, Technical University of Munich (2016).
- [145] N. O. Azak, M. Y. Shagam, D. M. Karabacak, K. L. Ekinici, D. H. Kim, and D. Y. Jang, *Applied Physics Letters* **91**, 093112 (2007).
- [146] L. Tian, *Physical Review Letters* **108**, 153604 (2012).
- [147] Y.-D. Wang and A. A. Clerk, *New Journal of Physics* **14**, 105010 (2012).
- [148] C. Dong, V. Fiore, M. C. Kuzyk, and H. Wang, *Science* **338**, 1609 (2012).
- [149] H. Okamoto, R. Schilling, H. Schütz, V. Sudhir, D. J. Wilson, H. Yamaguchi, and T. J. Kippenberg, *Appl. Phys. Lett.* **108**, 153105 (2016).
- [150] H. Fu, Z. cheng Gong, T. hua Mao, C. pu Sun, S. Yi, Y. Li, and G. yu Cao, *Physical Review A* **94**, 043855 (2016).
- [151] M. Fleischhauer and M. D. Lukin, *Physical Review A* **65**, 022314 (2002).
- [152] M. Johnsson and K. Mølmer, *Physical Review A* **70**, 032320 (2004).
- [153] A. Joshi and M. Xiao, *Physical Review A* **71**, 041801(R) (2005).
- [154] T. Gao, E. Estrecho, K. Bliokh, T. Liew, M. Fraser, S. Brodbeck, M. Kamp, C. Schneider, S. Höfling, Y. Yamamoto *et al.*, *Nature* **526**, 554 (2015).
- [155] H. Xu, D. Mason, L. Jiang, and J. Harris, arXiv preprint arXiv:1703.07374 (2017).
- [156] E. I. Rosenthal, N. K. Ehrlich, M. S. Rudner, A. P. Higginbotham, and K. W. Lehnert, *Physical Review B* **97**, 220301 (2018).
- [157] Rebeiz, *RF MEMS* (John Wiley and Sons, 2003).
- [158] A. Grayson, R. Shawgo, A. Johnson, N. Flynn, Y. Li, M. Cima, and R. Langer, *Proceedings of the IEEE* **92**, 6 (2004).
- [159] P. Vettiger, J. Brugger, M. Despont, U. Drechsler, U. Dürig, W. Häberle, M. Lutwyche, H. Rothuizen, R. Stutz, R. Widmer, and G. Binnig, *Microelectronic Engineering* **46**, 11 (1999).
- [160] A. Requicha, *Proceedings of the IEEE* **9**, 1922 (2003).
- [161] N. Kacem, S. Hentz, D. Pinto, B. Reig, and V. Nguyen, *Nanotechnology* **20**, 275501 (2009).

- [162] C. Chen, M. Ma, J. Z. Liu, Q. Zheng, and Z. Xu, *Journal of Applied Physics* **110**, 034320 (2011).
- [163] H. M. Youssef and K. A. Elsibai, *Nanoscale and Microscale Thermophysical Engineering* **15**, 48 (2011).
- [164] A. H. Ghadimi, D. J. Wilson, and T. J. Kippenberg, *Nano Letters* **17**, 3501 (2017).
- [165] S. Mangin, D. Ravelosona, J. A. Katine, M. J. Carey, B. D. Terris, and E. E. Fullerton, *Nature Materials* **5**, 210 (2006).
- [166] S. Krause, L. Berbil-Bautista, G. Herzog, M. Bode, and R. Wiesendanger, *Science* **317**, 1537 (2007).
- [167] T. Yang, T. Kimura, and Y. Otani, *Nature Physics* **4**, 851 (2008).
- [168] I. M. Miron, K. Garello, G. Gaudin, P.-J. Zermatten, M. V. Costache, S. Auffret, S. Bandiera, B. Rodmacq, A. Schuhl, and P. Gambardella, *Nature* **476**, 189 (2011).
- [169] L. Liu, O. J. Lee, T. J. Gudmundsen, D. C. Ralph, and R. A. Buhrman, *Phys. Rev. Lett.* **109**, 096602 (2012).
- [170] M. Weiler, A. Brandlmaier, S. Geprägs, M. Althammer, M. Opel, C. Bihler, H. Huebl, M. Brandt, R. Gross, and S. Goennenwein, *New Journal of Physics* **11**, 013021 (2009).
- [171] A. Brandlmaier, S. Geprägs, G. Woltersdorf, R. Gross, and S. Goennenwein, *Journal of Applied Physics* **110**, 043913 (2011).
- [172] L. Martin and R. Ramesh, *Acta Materialia* **60**, 2449 (2012).
- [173] L. Dreher, M. Weiler, M. Pernpeintner, H. Huebl, R. Gross, M. S. Brandt, and S. T. B. Goennenwein, *Phys. Rev. B* **86**, 134415 (2012).
- [174] M. Weiler, L. Dreher, C. Heeg, H. Huebl, R. Gross, M. S. Brandt, and S. T. Goennenwein, *Physical review letters* **106**, 117601 (2011).
- [175] P. G. Gowtham, T. Moriyama, D. C. Ralph, and R. A. Buhrman, *Journal of Applied Physics* **118**, 233910 (2015).
- [176] C. Chang, R. Tamming, T. Broomhall, J. Janusonis, P. Fry, R. Tobey, and T. Hayward, *Physical Review Applied* **10**, 034068 (2018).
- [177] C. A. Grimes, S. C. Roy, S. Rani, and Q. Cai, *Sensors* **11**, 2809 (2011).
- [178] R. C. Hall, *Journal of Applied Physics* **30**, 816 (1959).
- [179] D. Hunter, W. Osborn, K. Wang, N. Kazantseva, J. Hattrick-Simpers, R. Suchoski, R. Takahashi, M. L. Young, A. Mehta, L. A. Bendersky, S. E. Lofland, M. Wuttig, and I. Takeuchi, *Nature Communications* **2**, 518 (2011).
- [180] E. Quandt and A. Ludwig, *Journal of applied physics* **85**, 6232 (1999).
- [181] E. Quandt and A. Ludwig, *Sensors and Actuators A: Physical* **81**, 275 (2000).

- [182] E. Quandt, A. Ludwig, D. Lord, and C. Faunce, *Journal of applied physics* **83**, 7267 (1998).
- [183] A. Ludwig, M. Tewes, S. Glasmachers, M. Löhndorf, and E. Quandt, *Journal of magnetism and magnetic materials* **242**, 1126 (2002).
- [184] H. D. Chopra, M. R. Sullivan, A. Ludwig, and E. Quandt, *Physical Review B* **72**, 054415 (2005).
- [185] F. Johnson, H. Garmestani, S. Chu, M. McHenry, and D. Laughlin, *IEEE transactions on magnetics* **40**, 2697 (2004).
- [186] M. Cooke, M. Gibbs, and R. Pettifer, *Journal of magnetism and magnetic materials* **237**, 175 (2001).
- [187] M. Cooke, L. Wang, R. Watts, R. Zuberek, G. Heydon, W. Rainforth, and G. Gehring, *Journal of Physics D: Applied Physics* **33**, 1450 (2000).
- [188] R. Żuberek, A. Wawro, H. Szymczak, A. Wisniewski, W. Paszkowicz, and M. Gibbs, *Journal of Magnetism and Magnetic Materials* **214**, 155 (2000).
- [189] C.-Y. Hung, M. Mao, S. Funada, T. Schneider, L. Miloslavsky, M. Miller, C. Qian, and H. Tong, *Journal of Applied Physics* **87**, 6618 (2000).
- [190] Y. Cheng, A. J. Lee, J. T. Brangham, S. P. White, W. T. Ruane, P. C. Hammel, and F. Yang, *Applied Physics Letters* **113**, 262403 (2018).
- [191] M. A. W. Schoen, J. Lucassen, H. T. Nembach, T. J. Silva, B. Koopmans, C. H. Back, and J. M. Shaw, *Phys. Rev. B* **95**, 134410 (2017).
- [192] L. Flacke, L. Liensberger, M. Althammer, H. Huebl, S. Geprägs, K. Schultheiss, A. Buzdakov, T. Hula, H. Schultheiss, E. R. J. Edwards, H. T. Nembach, J. M. Shaw, R. Gross, and M. Weiler, *Applied Physics Letters* **115**, 122402 (2019).
- [193] M. Collet, O. Gladii, M. Evelt, V. Bessonov, L. Soumah, P. Bortolotti, S. Demokritov, Y. Henry, V. Cros, M. Bailleul *et al.*, *Applied Physics Letters* **110**, 092408 (2017).
- [194] Y. K. Kim and T. J. Silva **68**, 2885 (1996).
- [195] J. Joule, *Ann. Electr. Magn. Chem* **8**, 219 (1842).
- [196] J. Joule, *Philos. Mag. Ser* **3**, 30 (1847).
- [197] S. Chikazumi, *Physics of Ferromagnetism (International Series of Monographs on Physics)* (Clarendon Press, 1997).
- [198] M. J. Seitner, K. Gajo, and E. M. Weig, *Applied Physics Letters* **105**, 213101 (2014).
- [199] F. Hocke, *Microwave circuit-electromechanics in a nanomechanical hybrid system*, Ph.D. thesis, Technical University of Munich (2013).

- [200] P. Jörg, *Aufbau eines Freistrahl-Interferometers zur Untersuchung nanomechanischer Resonatoren im Magnetfeld*, Bachelor's thesis, Technical University of Munich (2015).
- [201] F. Hoehne, Y. A. Pashkin, O. Astafiev, L. Faoro, L. Ioffe, Y. Nakamura, and J. Tsai, *Physical Review B* **81**, 184112 (2010).
- [202] F. Cardarelli, *Materials Handbook: A Concise Desktop Reference*, 101–248 (Springer International Publishing, 2018).
- [203] D. W. Hoffman and J. A. Thornton, *Thin Solid Films* **45**, 387 (1977).
- [204] C. T. Wu, *Thin Solid Films* **64**, 103 (1979).
- [205] H. Windischmann, *Journal of Vacuum Science & Technology A* **9**, 2431 (1991).
- [206] E. R. Edwards, H. T. Nembach, and J. M. Shaw, *Physical Review Applied* **11**, 054036 (2019).
- [207] W. Gil, D. Görlitz, M. Horisberger, and J. Kötzler, *Physical Review B* **72**, 134401 (2005).
- [208] P. Sadeghi, M. Tanzer, S. L. Christensen, and S. Schmid, *Journal of Applied Physics* **126**, 165108 (2019).
- [209] Q. P. Unterreithmeier, E. M. Weig, and J. P. Kotthaus, *Nature* **458**, 1001 (2009).
- [210] P. N. Kambali, G. Swain, A. K. Pandey, E. Buks, and O. Gottlieb, *Applied Physics Letters* **107**, 063104 (2015).
- [211] M. Pernpeintner, T. Faust, F. Hocke, J. P. Kotthaus, E. M. Weig, H. Huebl, and R. Gross, *Applied Physics Letters* **105**, 123106 (2014).
- [212] W. Thomson, *Proceedings of the Royal Society of London* **8**, 546 (1857).
- [213] I. A. Campbell, A. Fert, and O. Jaoul, *Journal of Physics C: Solid State Physics* **3**, S95 (1970).
- [214] H. Ebert, A. Vernes, and J. Banhart, *Physical Review B* **54**, 8479 (1996).
- [215] J. B. Wachtman and D. G. LAM, *Journal of the American Ceramic Society* **42**, 254 (1959).
- [216] J. B. Wachtman, W. E. Tefft, D. G. Lam, and C. S. Apstein, *Physical Review* **122**, 1754 (1961).
- [217] M. Shimada, K. Matsushita, S. Kuratani, T. Okamoto, M. Koizumi, K. Tsukuma, and T. Tsukidate, *Journal of the American Ceramic Society* **67**, C (1984).
- [218] M. Harmouche and A. Wolfenden, *Materials Science and Engineering* **84**, 35 (1986).
- [219] R. Bruls, H. Hintzen, G. de With, and R. Metselaar, *Journal of the European Ceramic Society* **21**, 263 (2001).

- [220] C. Gerry and P. Knight, *Introductory Quantum Optics* (Cambridge University Press, 2004).
- [221] D. F. Walls and G. J. Milburn, *Quantum Optics* (Springer-Verlag GmbH, 2007).
- [222] H. Mabuchi, *Science* **298**, 1372 (2002).
- [223] *Nature Photonics* **3**, 669 (2009).
- [224] A. Wallraff, D. I. Schuster, A. Blais, L. Frunzio, R.-S. Huang, J. Majer, S. Kumar, S. M. Girvin, and R. J. Schoelkopf, *Nature* **431**, 162 (2004).
- [225] A. Blais, R.-S. Huang, A. Wallraff, S. M. Girvin, and R. J. Schoelkopf, *Physical Review A* **69**, 062320 (2004).
- [226] J. Clarke and F. K. Wilhelm, *Nature* **453**, 1031 (2008).
- [227] A. Megrant, C. Neill, R. Barends, B. Chiaro, Y. Chen, L. Feigl, J. Kelly, E. Lucero, M. Mariantoni, P. J. J. O'Malley, D. Sank, A. Vainsencher, J. Wenner, T. C. White, Y. Yin, J. Zhao, C. J. Palmstrøm, J. M. Martinis, and A. N. Cleland, *Applied Physics Letters* **100**, 113510 (2012).
- [228] H. Paik, D. I. Schuster, L. S. Bishop, G. Kirchmair, G. Catelani, A. P. Sears, B. R. Johnson, M. J. Reagor, L. Frunzio, L. I. Glazman, S. M. Girvin, M. H. Devoret, and R. J. Schoelkopf, *Physical Review Letters* **107**, 240501 (2011).
- [229] E. Jaynes and F. Cummings, *Proceedings of the IEEE* **51**, 89 (1963).
- [230] D. I. Schuster, A. Wallraff, A. Blais, L. Frunzio, R.-S. Huang, J. Majer, S. M. Girvin, and R. J. Schoelkopf, *Physical Review Letters* **94**, 123602 (2005).
- [231] T. Niemczyk, F. Deppe, H. Huebl, E. P. Menzel, F. Hocke, M. J. Schwarz, J. J. García-Ripoll, D. Zueco, T. Hümmer, E. Solano, A. Marx, and R. Gross, *Nature Physics* **6**, 772 (2010).
- [232] P. Forn-Díaz, J. Lisenfeld, D. Marcos, J. J. García-Ripoll, E. Solano, C. J. P. M. Harmans, and J. E. Mooij, *Physical Review Letters* **105**, 237001 (2010).
- [233] A. Baust, E. Hoffmann, M. Haeberlein, M. J. Schwarz, P. Eder, J. Goetz, F. Wulschner, E. Xie, L. Zhong, F. Quijandría, D. Zueco, J.-J. G. Ripoll, L. García-Álvarez, G. Romero, E. Solano, K. G. Fedorov, E. P. Menzel, F. Deppe, A. Marx, and R. Gross, *Physical Review B* **93** (2016).
- [234] J. Majer, J. M. Chow, J. M. Gambetta, J. Koch, B. R. Johnson, J. A. Schreier, L. Frunzio, D. I. Schuster, A. A. Houck, A. Wallraff, A. Blais, M. H. Devoret, S. M. Girvin, and R. J. Schoelkopf, *Nature* **449**, 443 (2007).
- [235] S. H. W. van der Ploeg, A. Izmalkov, A. M. van den Brink, U. Hahn, M. Grajcar, E. Il'ichev, H.-G. Meyer, and A. M. Zagoskin, *Physical Review Letters* **98**, 057004 (2007).
- [236] A. Hoffmann and S. D. Bader, *Phys. Rev. Applied* **4**, 047001 (2015).

- [237] A. Baust, E. Hoffmann, M. Haerberlein, M. J. Schwarz, P. Eder, J. Goetz, F. Wulschner, E. Xie, L. Zhong, F. Quijandría, B. Peropadre, D. Zueco, J.-J. G. Ripoll, E. Solano, K. Fedorov, E. P. Menzel, F. Deppe, A. Marx, and R. Gross, *Physical Review B* **91** (2015).
- [238] F. Wulschner, J. Goetz, F. R. Koessel, E. Hoffmann, A. Baust, P. Eder, M. Fischer, M. Haerberlein, M. J. Schwarz, M. Pernpeintner, E. Xie, L. Zhong, C. W. Zollitsch, B. Peropadre, J.-J. G. Ripoll, E. Solano, K. G. Fedorov, E. P. Menzel, F. Deppe, A. Marx, and R. Gross, *EPJ Quantum Technology* **3**, 10 (2016).
- [239] F. Arute, K. Arya, R. Babbush, D. Bacon, J. C. Bardin, R. Barends, R. Biswas, S. Boixo, F. G. S. L. Brandao, D. A. Buell, B. Burkett, Y. Chen, Z. Chen, B. Chiaro, R. Collins, W. Courtney, A. Dunsworth, E. Farhi, B. Foxen, A. Fowler, C. Gidney, M. Giustina, R. Graff, K. Guerin, S. Habegger, M. P. Harrigan, M. J. Hartmann, A. Ho, M. Hoffmann, T. Huang, T. S. Humble, S. V. Isakov, E. Jeffrey, Z. Jiang, D. Kafri, K. Kechedzhi, J. Kelly, P. V. Klimov, S. Knysh, A. Korotkov, F. Kostritsa, D. Landhuis, M. Lindmark, E. Lucero, D. Lyakh, S. Mandrà, J. R. McClean, M. McEwen, A. Megrant, X. Mi, K. Michielsen, M. Mohseni, J. Mutus, O. Naaman, M. Neeley, C. Neill, M. Y. Niu, E. Ostby, A. Petukhov, J. C. Platt, C. Quintana, E. G. Rieffel, P. Roushan, N. C. Rubin, D. Sank, K. J. Satzinger, V. Smelyanskiy, K. J. Sung, M. D. Trevithick, A. Vainsencher, B. Villalonga, T. White, Z. J. Yao, P. Yeh, A. Zalcman, H. Neven, and J. M. Martinis, *Nature* **574**, 505 (2019).
- [240] F. Marquardt and S. Girvin, *Physics* **2** (2009).
- [241] F. Lecocq, J. D. Teufel, J. Aumentado, and R. W. Simmonds, *Nature Physics* **11**, 635 (2015).
- [242] Y. Chu, P. Kharel, W. H. Renninger, L. D. Burkhardt, L. Frunzio, P. T. Rakich, and R. J. Schoelkopf, *Science* **358**, 199 (2017).
- [243] Y. Lee, Y. Park, F. Niu, B. Bachman, K. C. Gupta, and D. Filipovic **14**, 302 (2004).
- [244] F. C. Hoppensteadt and E. M. Izhikevich **48**, 133 (2001).
- [245] S. J. M. Habraken, K. Stannigel, M. D. Lukin, P. Zoller, and P. Rabl **14**, 115004 (2012).
- [246] S. Bose, K. Jacobs, and P. L. Knight, *Physical Review A* **59**, 3204 (1999).
- [247] W. Marshall, C. Simon, R. Penrose, and D. Bouwmeester, *Physical Review Letters* **91**, 130401 (2003).
- [248] M. Abdi, M. Pernpeintner, R. Gross, H. Huebl, and M. J. Hartmann, *Physical Review Letters* **114**, 173602 (2015).
- [249] P. Schmidt, D. Schwienbacher, M. Pernpeintner, F. Wulschner, F. Deppe, A. Marx, R. Gross, and H. Huebl, *Applied Physics Letters* **113**, 152601 (2018).
- [250] J. Koch, T. M. Yu, J. Gambetta, A. A. Houck, D. I. Schuster, J. Majer, A. Blais, M. H. Devoret, S. M. Girvin, and R. J. Schoelkopf, *Physical Review A* **76**, 042319 (2007).

- [251] K. F. Wulschner, *Interactions of harmonic and anharmonic macroscopic quantum oscillators in superconducting circuits*, Ph.D. thesis, Technical University of Munich (2016).
- [252] J. Goetz, F. Deppe, P. Eder, M. Fischer, M. Müting, J. P. Martínez, S. Pogorzalek, F. Wulschner, E. Xie, K. G. Fedorov, A. Marx, and R. Gross, *Quantum Science and Technology* **2**, 025002 (2017).
- [253] D. Schwienbacher, *Circuit nano-electromechanic stransmon qubits, nano-strings and resonators*, Master's thesis, Technical University of Munich (2016).
- [254] M. Boissonneault, J. M. Gambetta, and A. Blais, *Physical Review A* **79**, 013819 (2009).
- [255] S. Weis, R. Rivière, S. Deléglise, E. Gavartin, O. Arcizet, A. Schliesser, and T. J. Kippenberg, *Science* **330**, 1520 (2010).
- [256] J. Goetz, S. Pogorzalek, F. Deppe, K. Fedorov, P. Eder, M. Fischer, F. Wulschner, E. Xie, A. Marx, and R. Gross, *Physical Review Letters* **118**, 103602 (2017).
- [257] L. Rosenzweig, *Design and Realisation of Superconducting Quantum Circuits for Nano-Electromechanical Experiments*, Master's thesis, Technical University of Munich (2018).
- [258] R. Barends, J. Kelly, A. Megrant, D. Sank, E. Jeffrey, Y. Chen, Y. Yin, B. Chiaro, J. Mutus, C. Neill, P. O'Malley, P. Roushan, J. Wenner, T. C. White, A. N. Cleland, and J. M. Martinis, *Physical Review Letters* **111**, 080502 (2013).
- [259] P. E. Schmidt, *Nanomechanical Quantum Systems*, Ph.D. thesis, Technical University of Munich (2019).
- [260] M. Bicer, M. N. Esfahani, A. D. Yalcinkaya, and B. E. Alaca, *Journal of Micromechanics and Microengineering* **28**, 105003 (2018).
- [261] S. S. Kalarickal, P. Krivosik, M. Wu, C. E. Patton, M. L. Schneider, P. Kabos, T. J. Silva, and J. P. Nibarger, *Journal of Applied Physics* **99**, 093909 (2006).
- [262] R. Ohshima, S. Klingler, S. Dushenko, Y. Ando, M. Weiler, H. Huebl, T. Shinjo, S. T. Goennenwein, and M. Shiraishi, *Applied Physics Letters* **110**, 182402 (2017).

LIST OF PUBLICATIONS

- M. Pernpeintner, P. Schmidt, D. Schwienbacher, R. Gross and H. Huebl. Frequency Control and Coherent Excitation Transfer in a Nanosting-resonator Network. *Physical Review Applied* **10**, 034007 (2018); doi: [10.1103/PhysRevApplied.10.034007](https://doi.org/10.1103/PhysRevApplied.10.034007)
- P. Schmidt, D. Schwienbacher, M. Pernpeintner, F. Wulschner, F. Deppe, A. Marx, R. Gross and H. Huebl. Ultrawide-range photon number calibration using a hybrid system combining nano-electromechanics and superconducting circuit quantum electrodynamics. *Applied Physics Letters* **113**, 152601 (2018); doi: [10.1063/1.5052414](https://doi.org/10.1063/1.5052414)
- D. Schwienbacher, M. Pernpeintner, L. Liensberger, E.R.J. Edwards, H.T. Nembach, J.M. Shaw, M. Weiler, R. Gross and H. Huebl. Magnetoelasticity of Co₂₅Fe₇₅ thin films *Journal of Applied Physics* **126**, 103902 (2019); doi: [10.1063/1.5116314](https://doi.org/10.1063/1.5116314)
- D. Schwienbacher, T. Luschmann and H. Huebl. Dia- and adiabatic dynamics in a phononic network *arXiv* 2011.08080 (2020); arXiv: [2011.08080](https://arxiv.org/abs/2011.08080)

ACKNOWLEDGMENTS

There are many people without whom this thesis would not have been possible. In particular, I would like to thank:

Dr. Hans Hübl, my supervisor. He introduced me to the field of nanomechanics, and was in no small part responsible for the fact that I remained in it for such a long time. Thank you for invaluable support regarding my whole thesis. For your help during sample fabrication, experiments and data evaluation, and for carefully proofreading this thesis. I am also grateful for your encouragement and personal support in many situations.

Prof. Dr. Rudolf Gross, for giving me the opportunity to write my PhD thesis at the Walther-Meißner-Institut. Thank you for various fruitful discussions, for valuable support in every situation and for your constructive feedback that made me think about many things again and again.

Dr. Matthias Pernpeintner, for introducing me to the field of optomechanics and circuit electromechanics. Thank you for sharing your expertise in fabrication, measurement techniques and data analysis. Both during my Master's thesis and the first months of my PhD. Your supervision during this time inspired me and I aspired to mentor my students in the way you did for me.

Dr. Nathalie Segercrantz, for the interesting discussions concerning quantum nanomechanics and for reminding me of some of the basics I'd already buried. Thank you for your insight into quantum nanomechanics, physics and many other topics.

Dr. Philip Schmidt, for being a part of my scientific life at WMI from the beginning of my Masters Thesis to quite some time into my PhD. Thank you for the many interesting discussions on nanomechanics, your help in the lab and outside of it. And for keeping me entertained with anecdotes from your life.

Dr. Stefan Weichselbaumer, for the tremendous help with measurement software and the operation of the Abaqus fridge. Thank you for your insight during many technical discussions and your help ending them.

My master students, Lisa Rosenzweig and Thomas Luschmann, for joining me in the quest for nanomechanics. Thank you for the countless hours and effort you spent for sample fabrication, measurements and simulations. Thank you for the indispensable results that contributed to this thesis.

My bachelor students, Andreas Faltermeier and Korbinian Rubenbauer, for their efforts in

improving the optical setups and characterizing sources of mechanical noise in the Abaqus fridge.

The coffee group: Michael Fischer, Katrin Ganzhorn, Stefan Weichselbaumer and Nathalie Segercrantz, for many discussions concerning physics and the rest of the world during the consumption of hot caffeinated beverages.

My office colleagues Stefan Klinger, Alma Dorantes, Tobias Wimmer, Luis Flacke and Qi-Ming Chen, for many discussions about politics, biology, music and physics as well as the occasional laugh during and after working hours.

Lukas Liensberger and Thomas Luschmann, for helping me staying sane during the Corona-home-office-time.

The WMI magnetism group, for all the time spent in seminars and meetings, giving me many good ideas and constructive comments as well as giving me access to your experimental equipment.

The WMI qubit group, for many constructive discussions during our meetings and for not only sharing your experimental equipment but also your experimental insight.

Thomas Brenninger, Sebastian Kammerer and Astrid Habel. For their help and assistance with all thin film and nano-fabrication facilities at WMI, and for their support when I was in need of chemicals and other consumables.

The IT team, Matthias Opel, Dieter Guratzsch and Michael Renger. For the time we spent together solving the different IT issues at WMI.

The WMI workshop, Helmut Thies, Alexander Rößl, Georg Nitschke and Christian Reichlmeier, for fabricating components for the optical interferometers, cryostats and for support regarding all technical problems.

The "Helium Halle", Peter Binkert, Jan Naundorf and Harald Schwaiger, for providing liquid helium for my low temperature experiments.

The administrative staff, Emel Dönertas, Andrea Person, Carola Siegmayer, Martina Meven and Ludwig Ossiander. For taking over most of the administrative work so that I could focus on physics.

Everyone else at the WMI, all the other Postdocs, PhD-, Master, and Bachelor students, for the great times I shared at the institute with you, and C.W., for lending me 10 ct. for a drink on a hot day ;)

And last, but not least: Meiner Familie. Vielen Dank für all eure Unterstützung während meiner Doktorarbeit, ohne euch wäre das alles nicht möglich gewesen.